

FÁBIO MACHADO CAVALCANTI

Evaluation of catalysts supported on carbon nanotubes and kinetic modeling of the process for the Water-Gas Shift (WGS) reaction: macro and microkinetic approaches and use of machine learning techniques for catalyst selection

São Paulo
2024

FÁBIO MACHADO CAVALCANTI

Evaluation of catalysts supported on carbon nanotubes and kinetic modeling of the process for the Water-Gas Shift (WGS) reaction: macro and microkinetic approaches, and use of machine learning techniques for catalyst selection

Corrected Version

Ph.D. Thesis presented to the Graduate Program in Chemical Engineering at Escola Politécnica, Universidade de São Paulo, Brazil to obtain the degree of Doctor of Science.

Concentration area: Chemical Engineering

Advisors:

Prof. Reinaldo Giudici

Prof^a. Rita Maria de Brito Alves

Prof. Martin Schmal

Prof. Joris W. Thybaut (Ghent University)

São Paulo

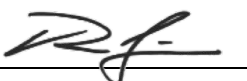
2024

Autorizo a reprodução e divulgação total ou parcial deste trabalho, por qualquer meio convencional ou eletrônico, para fins de estudo e pesquisa, desde que citada a fonte.

Este exemplar foi revisado e corrigido em relação à versão original, sob responsabilidade única do autor e com a anuência de seu orientador.

São Paulo, 16 de fevereiro de 2024

Assinatura do autor: Fábio Machado Cavalcanti

Assinatura do orientador: 

Catálogo-na-publicação

CAVALCANTI, FÁBIO

Evaluation of catalysts supported on carbon nanotubes and kinetic modeling of the process for the Water-Gas Shift (WGS) reaction: macro and microkinetic approaches, and use of machine learning techniques for catalyst selection / F. CAVALCANTI – versão corr. -- São Paulo, 2024.

170 p.

Tese (Doutorado) - Escola Politécnica da Universidade de São Paulo.
Departamento de Engenharia Química.

1.HIDROGÊNIO 2.CATÁLISE 3.NANOTUBOS DE CARBONO 4.REDES NEURAIS 5.CINÉTICA QUÍMICA I.Universidade de São Paulo. Escola Politécnica. Departamento de Engenharia Química II.t.

Cavalcanti, FM. Evaluation of catalysts supported on carbon nanotubes and kinetic modeling of the process for the Water-Gas Shift (WGS) reaction: macro and microkinetic approaches and use of machine learning techniques for catalyst selection. Corrected Version. 2024. Thesis (Doctorate in Chemical Engineering) – Escola Politécnica, Universidade de São Paulo, São Paulo, 2024.

Approved on: December 20th, 2023

Examining Committee

Prof^a. Dr^a. Rita Maria de Brito Alves (President)

Institution: Universidade de Sao Paulo

Judgment: Approved

Prof. Dr. Fábio Souza Toniolo

Institution: Universidade Federal do Rio de Janeiro

Judgment: Approved

Prof. Dr. Joris W. Thybaut

Institution: Ghent University (Belgium)

Judgment: Approved

Prof. Dr. José Carlos Costa da Silva Pinto

Institution: Universidade Federal do Rio de Janeiro

Judgment: Approved

Dr. Robson Pablo Sobradie Peguin

Institution: BRASKEM

Judgment: Approved

To my wife and daughter: loves of my life.

To my parents, grandmothers and brothers: my strength.

Thank you for believing together with me.

ACKNOWLEDGMENTS

To **God** for giving me the strength to overcome the challenges that life has given me so far.

To my girlfriend, fiancée and now wife, **Nathalia de Miranda Ladewig Cavalcanti**, for all these more than 16 years of much companionship, care, and affection. You were my greatest pillar throughout this journey, being the biggest supporter of my move to São Paulo. Thank you for never letting me get discouraged by the difficulties faced during the lab experiments that did not work out or by the programming codes that did not run properly, even without understand anything I was saying. Thank you for always being by my side, giving me that strength to make everything work out. It is very rewarding to be able to fulfill our life dreams together. *Merci pour tout, mon amour!* I love you so much!

To my daughter, **Olívia Ladewig Cavalcanti**, who came into the world to make everything more colorful! With you, I could feel the greatest love that exists in the world, which strengthens me every day. You are the fortitude where your mom and I safeguard ourselves and gain energy to move forward. As the lyrics of a song say, “*you will be in my heart, always!*”!

To my parents, **Fábia Machado Cavalcanti** and **José Roberto Cavalcanti**, for encouraging me to move to study in São Paulo, seeing in this scenario the construction of a promising and auspicious future for me. Thank you also for always pushing me and helping me complete my doctorate, as life was demanding more than I could bear. I love you so much, painho and mainha!

To grandma (voinha), **Jandira Dantas**, for going to great lengths to help me become a competent and qualified professional. Your 91-year history is a source of inspiration for me to continue always seeking to improve myself. Her love and enthusiasm for Nanotechnology is contagious to everyone and makes me always want to push the frontiers of knowledge. Her legacy will remain with me forever!

To my two brothers, **Eduardo** and **Leonardo Cavalcanti** (and also his wife **Zaira Porto**), for their help and companionship along the way. Also, for encouraging me to study Python and R, giving valuable programming tips that helped me develop the codes for this thesis. I trust everything in you!

To my in-laws, **Sandra Fausta** and **Gerwal Ladewig**, for always being present in our lives, wishing us success, and being that shelter in difficult times. Also, to **Victor** and **Anninha Ladewig** for the family you all are to us. We love you so much!

To my advisors, **Prof. Reinaldo Giudici**, **Prof. Rita Maria de Brito Alves**, and **Prof. Martin Schmal** for all the learning, encouragement, and guidance in this work. You are a dream team that any graduate student in Brazil aspires to be able to work with. Each of you played an important role in my formation and development of this experimental and computational thesis. Participating in the construction group of LaPCat (Catalytic Process Research and Innovation Laboratory) was an experience that will help me in the future challenges of my research career. Working with great experts in the different fields of Chemical Engineering made the journey richer and provided more learning for life! You will be my forever references!

To **Prof. Roberto Guardani**, in whose name I thank the entire PEQ faculty for the excellent classes taught and harmonious coexistence in the department's corridors.

To my foreign advisor, **Prof. Joris W. Thybaut**, for being so receptive to my proposal to undertake an internship in Belgium at LCT (Laboratory for Chemical Technology) at Ghent University. This opportunity of working with global references in chemical kinetics modeling and simulation was a turning point in my career. Among these researchers, I would like to thank **Dr. Jeroen Poissonnier** immensely for closely following the evolution of my research. You have no idea how much I learned from our weekly meetings, always having good discussions. I am so grateful to have worked with you both!

To my lab mentor, **Dr^a. Camila Emilia Kozonoe**, for all the teachings about experimental work in the laboratory, from a complicated catalyst synthesis method to the safe opening of a gas cylinder. Furthermore, for the great friendship created: *"you can count on me 'cause I can count on you!"* I also take this opportunity to extend my thanks for the companionship and assistance in experiments of **Maria Giuliana Fontanelli Torraga**, **Kelvin Pacheco**, **Thiago Hewer**, **Thiago Abreu**, **Tamara Mignoli**, and **Higor Azevedo (PEQ-USP)**, **Célio Souza**, **Rodrigo Bonfim** and **Thiago Miceli (NUCAT-COPPE-UFRJ)**, and **Tom Vandevyvere (LCT-UGent)**.

To grants n. 2017/11940-5 and n. 2019/09766-2, **São Paulo Research Foundation (FAPESP)**. This study was also financed in part by the **Coordenação de Aperfeiçoamento de Pessoal de Nível Superior – Brasil (CAPES)** – Finance Code 001.

*“Je trace des chemins qui n'attendent que toi
À toi, l'enfant qui vient, je précède tes pas
Je murmure ton nom dans le souffle de ma voix
Je t'offrirai le monde, toi que je n'connais pas
Je t'ouvre grand mon cœur comme on ouvre ses mains
Je t'espère des bonheurs aussi grand que les miens
Demain, c'est toi”*

Zaz

RESUMO

Cavalcanti, F. M. **Avaliação de catalisadores suportados em nanotubos de carbono e modelagem cinética do processo para a reação Water-Gas Shift (WGS):** abordagens macro e microcinéticas e uso de técnicas de *machine learning* para seleção de catalisadores. Versão Corrigida. 2024. Tese (Doutorado em Engenharia Química). Escola Politécnica, Universidade de São Paulo, São Paulo, 2024.

A reação Water-Gas Shift (WGS) é uma das rotas mais importantes para a produção de hidrogênio. Ela tem recebido grande importância devido ao uso do H₂ nas principais indústrias químicas e como principal fonte de energia limpa no futuro. Embora já existam catalisadores industriais bem estabelecidos para a reação WGS, vários novos foram desenvolvidos para melhorar o desempenho e a estabilidade do processo com metais nobres em nanoescala suportados em óxidos. Para auxiliar com esses numerosos catalisadores, Redes Neurais Artificiais (RNAs) foram utilizadas para construir um modelo baseado em dados catalíticos da literatura. Neste contexto, foi desenvolvido um novo catalisador: nanopartículas de Co/CeO₂-Sr suportadas em Nanotubos de Carbono de Paredes Múltiplas. O uso do Co resultou em alta atividade e tolerância ao enxofre, enquanto CeO₂ possui alta capacidade de armazenamento de oxigênio devido à sua redutibilidade, e o Sr atua como promotor. O uso de nanotubos de carbono como suporte tem se mostrado vantajoso devido à sua elevada área superficial, propriedades condutoras e baixa disponibilidade de alguns óxidos. A atividade catalítica foi avaliada em uma faixa de temperatura industrialmente relevante sob pressão atmosférica, apresentando melhores desempenhos em temperaturas mais altas (300-450°C), e alcançando conversões de CO próximas do equilíbrio. Além disso, dados cinéticos foram coletados variando-se as concentrações das espécies. Modelos de lei de potência, de etapa determinante de reação, e os microcinéticos foram ajustados a eles, para discriminar a melhor formulação para compreender completamente a reação em estudo. O mecanismo redox foi identificado como o mais adequado e permitiu explicar o papel do catalisador durante a reação WGS, proporcionando ciclos de oxidação e redução a partir da disponibilidade e mobilidade de espécies O* em sua superfície. Todo este trabalho é um material de consultoria robusto para auxiliar nos planejamentos futuros de catalisadores e otimização para projetos de reatores industriais.

Palavras-chave: Produção de hidrogênio. Reação Water-Gas Shift. Nanotubos de carbono com paredes múltiplas. Redes Neurais. Estudo cinético. Modelagem microcinética.

ABSTRACT

Cavalcanti, F. M. **Evaluation of catalysts supported on carbon nanotubes and kinetic modeling of the process for the Water-Gas Shift (WGS) reaction:** macro and microkinetic approaches and use of machine learning techniques for catalyst selection. Corrected Version. 2024. Thesis (Doctorate in Chemical Engineering). Escola Politécnica, Universidade de São Paulo, São Paulo, 2024.

The Water-Gas Shift (WGS) reaction is one of the most important routes for hydrogen production. It has received great importance due to the use of H₂ in the main chemical industries and main clean energy source in the future. Although there are already well-established industrial catalysts for the WGS reaction, several new ones have been developed for improving process performance and stability with noble metals at nanoscale supported on oxides. To assist with these numerous catalysts, Artificial Neural Networks (ANNs) were used to build a model based on catalytic data from the literature. In this context, a novel catalyst, Co/CeO₂-Sr nanoparticles supported on Multi-Walled Carbon Nanotubes (MWCNTs), was developed. The use of Co resulted in a high activity and sulfur-tolerance, while CeO₂ has a high oxygen storage capacity as a result of its reducibility, and Sr acts as a promoter. The use of carbon nanotubes as catalyst support has shown to be advantageous due to their high surface area, conductive properties, and the low availability of some oxides. The catalytic activity was evaluated in an industrially relevant temperature range under atmospheric pressure, presenting better performances at higher temperatures (300-450°C), and achieving near-equilibrium CO conversion. Furthermore, kinetic data was collected by varying the species concentrations. Conventional power-law, mechanistic rate-determining step, and microkinetic models were adjusted to them, for discriminating the best formulation to fully understand the chemical reaction. The redox mechanism was identified as most suitable and allows explaining the catalyst role during the WGS reaction, providing oxidation and reduction cycles from the availability and mobility of O* species on its surface. All this work is a robust consultancy material to assist in future catalyst design and optimization for industrial reactor projects.

Keywords: Hydrogen production. Water-Gas Shift reaction. Multi-walled carbon nanotubes. Artificial Neural Networks. Kinetic study. Microkinetic modeling.

LIST OF FIGURES

Figure 1.1 – Simplified process flow diagram for H ₂ production through steam reforming of natural gas.....	28
Figure 3.1 – Distribution of the outcome variables reported in the articles cited in the reference review paper (LEVALLEY; RICHARD; FAN, 2014). The sum of the percentages is greater than 100%, since more than one variable can be reported in one article.....	39
Figure 3.2 – Three-Layer Feedforward Neural Network employed in this work.....	40
Figure 3.3 – Scheme of a neuron of layer <i>j</i>	41
Figure 3.4 – Mean squared error <i>versus</i> number of neurons in the hidden layer (a) for the testing set and (b) for the training set.	45
Figure 3.5 (a) Comparison between prediction and observed CO conversion values for the training set (b) Histogram of residues for the training set.	46
Figure 3.6 (a) Comparison between prediction and observed CO conversion values for the testing set (b) Histogram of residues for the testing set.	46
Figure 3.7 (a) Comparison between prediction and observed CO conversion values for all dataset (b) Histogram of residues for all dataset.	47
Figure 3.8 – ANN structure with 3 layers – 1 input, 1 hidden and 1 output layer – and the estimated weights computed during the training step (NH = 12, error = 0.04368, steps = 5304).	48
Figure 3.9 – CO conversion <i>versus</i> Cu composition (NH = 12, Cu/CeO ₂ , T = 300°C, P = 1 bar, m _{cat} = 0.1 g, GHSV = 1000 h ⁻¹ , surface area = 100 m ² /g, T _{calc} = 300°C, t _{calc} = 4 h, feed composition: 2% CO, 10% H ₂ O, 88% N ₂).....	49
Figure 3.10 – CO conversion <i>versus</i> temperature for different active phases (NH = 12, Metal/CeO ₂ , Metal = 2 wt%, P = 1 bar, m _{cat} = 0.1 g, GHSV = 1000 h ⁻¹ , surface area = 100 m ² /g, T _{calc} = 300°C, t _{calc} = 4 h, feed composition: 2% CO, 10% H ₂ O, 88% N ₂). ...	50
Figure 3.11 – CO conversion <i>versus</i> Cu composition and temperature (NH = 12, Cu/CeO ₂ , P = 1 bar, m _{cat} = 0.1 g, GHSV = 1000 h ⁻¹ , surface area = 100 m ² /g, T _{calc} = 300°C, t _{calc} = 4 h, feed composition: 2% CO, 10% H ₂ O, 88% N ₂).....	51
Figure 3.12 – CO conversion <i>versus</i> GHSV (NH = 12, Cu/CeO ₂ , Cu = 2wt%, T = 300°C, P = 1 bar, m _{cat} = 0.1 g, surface area = 100 m ² /g, T _{calc} = 300°C, t _{calc} = 4 h, feed composition: 2% CO, 10% H ₂ O, 88% N ₂).....	53

Figure 3.13 – CO conversion <i>versus</i> GHSV and temperature (NH = 12, Cu/CeO ₂ , Cu = 2 wt%, P = 1 bar, m _{cat} = 0.1 g, surface area = 100 m ² /g, T _{calc} = 300°C, t _{calc} = 4 h, feed composition: 2% CO, 10% H ₂ O, 88% N ₂).	54
Figure 3.14 – CO conversion <i>versus</i> temperature for different feed compositions (NH = 12, Cu/CeO ₂ , Cu = 2 wt%, T = 300°C, P = 1 bar, m _{cat} = 0.1 g, GHSV = 1000 h ⁻¹ , surface area = 100 m ² /g, T _{calc} = 300°C, t _{calc} = 4 h, feed composition: 2% CO, 10% H ₂ O, 88% N ₂ – steam/CO = 5 (reference); 2% CO, 40% H ₂ O, 58% N ₂ – steam/CO = 20; 10.7% CO, 28.6% H ₂ O, 5% CO ₂ , 39.3% H ₂ , 16.4% N ₂ – reformat).	55
Figure 3.15 – CO conversion <i>versus</i> calcination temperature (NH = 12, Cu/CeO ₂ , Cu = 2 wt%, T = 300°C, P = 1 bar, m _{cat} = 0.1 g, GHSV = 1000 h ⁻¹ , surface area = 100 m ² /g, t _{calc} = 4 h, feed composition: 2% CO, 10% H ₂ O, 88% N ₂).	56
Figure 3.16 – CO conversion <i>versus</i> surface area (NH = 12, Cu/CeO ₂ , Cu = 2 wt%, T = 300°C, P = 1 bar, m _{cat} = 0.1 g, GHSV = 1000 h ⁻¹ , T _{calc} = 300°C, t _{calc} = 4 h, feed composition: 2% CO, 10% H ₂ O, 88% N ₂).	57
Figure 4.1 – Schematic representation of SWCNTs and MWCNTs.	66
Figure 4.2 – Scheme of the oxidative treatment of CNTs with HNO ₃	67
Figure 4.3 – Experimental apparatus for the functionalization of the MWCNTs.	70
Figure 4.4 - MWCNTs being impregnated with the Cu-precursor solution aqueous solution.	71
Figure 4.5 – Microactivity-EFFI coupled with GC.	75
Figure 4.6 – N ₂ physisorption isotherms at 77 K for the crude MWCNTs (black squares) and the synthesized catalyst of Co/Ce-Sr-MWCNT (blue circles).	79
Figure 4.7 – X-ray diffractogram of the Co/Ce-Sr-MWCNT catalyst. The numbers between brackets correspond to the hkl planes of the MWCNT.	81
Figure 4.8 – TEM images of the catalysts during different steps of the preparation method: (a)-(c) crude MWCNTs, (d) functionalized MWCNTs, (e)-(g) Ce and Sr nanoparticles impregnated on the MWCNTs, and (h)-(l) Co, Ce, and Sr nanoparticles deposited on the MWCNTs.	84
Figure 4.9 – EDX spectrum from Figure 3i of the Co/Ce-Sr-MWCNT catalyst.	85
Figure 4.10 – Raman spectra of the raw MWCNT and the synthesized catalyst of Co/Ce-Sr-MWCNT.	86
Figure 4.11 – TGA (black) and DTG (blue) curves of the catalyst of Co/Ce-Sr-MWCNT under N ₂ atmosphere.	87
Figure 4.12 – H ₂ -TPR profile for the Co/Ce-Sr-MWCNT catalyst.	89

Figure 4.13 – Signal produced by successive injections of equal volumes of CO onto the catalyst of Co/Ce-Sr-MWCNT.	90
Figure 4.14 – CO conversion as a function of temperature for the WGS reaction over the Co/Ce-Sr-MWCNT catalyst with space time ($W/F_{CO,inlet}$) of $62.5 \text{ kg s mol}^{-1}$ for 2 different pretreatment temperatures (empty points at 400°C and filled points at 300°C). The dashed line represents the equilibrium conversions for the feed composition of the experiment: 11% CO, 29% H_2O , and 60% N_2 under atmospheric pressure (calculated using the REquil pallet from ASPEN PLUS® 8.0). Lines connecting the experimental points were added to guide the eye.....	91
Figure 4.15 – H_2 yield as a function of temperature for the WGS reaction over the Co/Ce-Sr-MWCNT catalyst with space time ($W/F_{CO,inlet}$) of $62.5 \text{ kg s mol}^{-1}$ for 2 different pretreatment temperatures (empty points at 400°C and filled points at 300°C). The dashed line represents the equilibrium conversions for the feed composition of the experiment: 11% CO, 29% H_2O , and 60% N_2 under atmospheric pressure. (calculated using the REquil pallet from ASPEN PLUS® 8.0). Lines connecting the experimental points were added to guide the eye.....	92
Figure 4.16 – CO conversion as a function of space time ($W/F_{CO,inlet}$) for the WGS reaction over the Co/Ce-Sr-MWCNT catalyst at three different temperatures: 300° (■), 350° (●) and 400°C (▲). The reaction was conducted with a feed composition of 11% CO, 29% H_2O , and 60% N_2 , and under atmospheric pressure. Lines are added to guide the eye.	93
Figure 4.17 – 15-hour stability test for the WGS reaction over the Co/Ce-Sr-MWCNT catalyst at 350°C and a space time ($W/F_{CO,inlet}$) of $62.5 \text{ kg s mol}^{-1}$, a feed composition of 11% CO, 29% H_2O , and 60% N_2 , and under atmospheric pressure.....	94
Figure 5.1 – (a) Parity plot of molar flow rates of CO. Performance curves of CO conversion as a function (b) of temperature and (c) of space time, for the WGS reaction over the Co/Ce-Sr-MWCNT catalyst using model M1.	105
Figure 5.2 – (a) Parity plot of molar flow rates of CO. Performance curves of CO conversion as a function (b) of temperature and (c) of space time, for the WGS reaction over the Co/Ce-Sr-MWCNT catalyst using model M2.	106
Figure 5.3 – (a) Parity plot of molar flow rates of CO. Performance curves of CO conversion as a function (b) of temperature and (c) of space time, for the WGS reaction over the Co/Ce-Sr-MWCNT catalyst using model M3.	108

Figure 5.4 – (a) Parity plot of molar flow rates of CO. Performance curves of CO conversion as a function (b) of temperature and (c) of space time, for the WGS reaction over the Co/Ce-Sr-MWCNT catalyst using model M4.....	109
Figure 5.5 – (a) Parity plots of molar flow rates of CO. Performance curves of CO conversion as a function (b) of temperature and (c) of space time, for the WGS reaction over the Co/Ce-Sr-MWCNT catalyst using model M5.....	111
Figure 6.1 – Performance curves and parity plots. In the former, points are experimental data, and lines represent the model predictions. The CO conversion as a function of the temperature curve was carried out with space time of 88 kg s mol ⁻¹ . For the CO conversion as a function of space time graphs, the blue line represents the reaction performed at 300°C, the red at 350°C, and the green at 400°C.	123
Figure 6.2 – Energy diagram of the WGS reaction mechanism according to the values in Table 6.1.....	125

LISTA OF TABLES

Table 3.1 – Variables selected for the ANN and their ranges.....	38
Table 3.2 – Variables values for the sensitivity analysis.....	43
Table 3.3 - CO conversion sensitivities related to the considered input variables.	58
Table 4.1 – Textural properties of the crude MWCNT and the Co/Ce-Sr-MWCNT catalyst as obtained from N ₂ physisorption at 77 K	80
Table 4.2 – Crystallite size of the compounds of the Co/Ce-Sr-MWCNT catalyst (calculated using the Scherrer equation).....	82
Table 4.3 – Properties obtained from the CO pulsed chemisorption analysis.	90
Table 5.1 – Data acquired for the kinetic study of the WGS reaction over the Co/Ce-Sr-MWCNT under atmospheric pressure.	96
Table 5.2 – Data acquired in terms of molar flow rates for the kinetic study of the WGS reaction over the Co/Ce-Sr-MWCNT under atmospheric pressure.	98
Table 5.3 – Rival kinetic models considered for the WGS reaction rate conducted on the Co/Ce-Sr-MWCNT catalyst.	101
Table 5.4 – Metrics to evaluate the regression performance for each kinetic model.	104
Table 5.5 – Estimated kinetic parameters for the WGS reaction over the Co/Ce-Sr-MWCNT catalyst of the model represented by the simplified power law model (M1).	104
Table 5.6 – Estimated kinetic parameters for the WGS reaction over the Co/Ce-Sr-MWCNT catalyst of the model represented by power-law (M2).	106
Table 5.7 – Estimated kinetic parameters for the WGS reaction over the Co/Ce-Sr-MWCNT catalyst of the model represented by the LHHW mechanism (M3).	107
Table 5.8 – Estimated kinetic parameters for the WGS reaction over the Co/Ce-Sr-MWCNT catalyst of the model represented by the Eley-Rideal mechanism (M4). ...	109
Table 5.9 – Estimated kinetic parameters for the WGS reaction over the Co/Ce-Sr-MWCNT catalyst of the model represented by the redox mechanism (M5).	110
Table 5.10 – Statistical analysis of the model discrimination procedure.....	112
Table 6.1 – Reaction mechanism considered for the microkinetic model of the WGS over a Co catalyst supported on MWCNT with its parameter values (the estimated ones are shown in bold with the corresponding 95% confidence interval. The adsorption/desorption steps are shown in blue, while the surface reaction ones are	

shown in red. The fixed parameters were used from GOKHALE; DUMESIC;
MAVRIKAKIS (2008). 120

LIST OF ABBREVIATIONS AND ACRONYMS

AC	Activated carbon
AI	Artificial Intelligence
ANNs	Artificial Neural Networks
Ar	Argonium
BET	Brunauer, Emmet and Teller method
BJH	Barret, Jayner and Halenda method
Ce	Cerium
$\text{Ce}(\text{NO}_3)_3 \cdot 6\text{H}_2\text{O}$	Cerium III nitrate hexahydrate
CeO_2	Ceria
CeO_x	Cerium(2x) oxide
Ce_2O_3	Cerium(III) oxide
CME	Controlled Evaporator Mixer
CNT	Carbon Nanotubes
Co	Cobalt
CoO	Cobalt(II) oxide
Co_3O_4	Cobalt(II,III) oxide
CO	Carbon monoxide
CO_2	Carbon dioxide
Cr	Chromium
CVD	Chemical Vapor Deposition
Cu	Copper
DTG	Derivative Thermogravimetric
EDX	Energy Dispersive X-Ray Spectroscopy
Fe	Iron
GHSV	Gas hourly space velocity
H_2	Hydrogen
H_2 -TPR	Hydrogen Temperature Programmed Reduction
H_2O	Water
He	Helium
HFCs	Hydrogen fuel cells

HNO ₃	Nitric acid
HT	High temperature
LHHW	Langmuir-Hinshelwood-Hougen-Watson
LT	Low temperature
ML	Machine Learning
MSE	Mean Squared Error
MWCNTs	Multi-Walled Carbon Nanotubes
Mo	Molybdenum
Mn	Manganese
N ₂	Nitrogen
NH	Number of hidden neurons
Ni	Nickel
NP	Nanoparticles
OSC	Oxygen storage capacity
Pd	Palladium
PSO	Particle Swarm Optimization
Pt	Platinum
RDS	Rate-determining step
Rh	Rhodium
RMSD	Root-mean-square deviation
Ru	Ruthenium
RWGS	Reverse Water-Gas Shift
Sr	Strontium
Sr(NO ₃) ₂	Strontium nitrate
SSQ	Sum of squares
SWCNT	Single-Walled Carbon Nanotubes
TCD	Thermal conductivity detector
TEM	Transmission Electron Microscopy
TGA	Thermogravimetric Analysis
WGS	Water-Gas Shift
XRD	X-Ray Diffraction

CONTENTS

1	INTRODUCTION.....	28
2	OBJECTIVES	33
3	CHAPTER I – USE OF ARTIFICIAL NEURAL NETWORKS FOR CATALYST SELECTION.....	35
3.1	Introduction	35
3.2	Methodology.....	37
3.2.1	Data selection	37
3.2.2	Artificial Neural Networks.....	40
3.2.3	Sensitivity analysis.....	43
3.3	Results and discussion.....	44
3.3.1	ANN performance and regression.....	44
3.3.2	Sensitivity analysis findings	48
3.3.3	Discussion	58
3.4	Conclusions	60
4	CHAPTER II – SYNTHESIS, CHARACTERIZATION AND CATALYTIC TESTS	61
4.1	Introduction	61
4.2	Literature review	63
4.2.1	Catalyst for the WGS reaction.....	63
4.2.2	Use of carbon nanotubes in catalysis	65
4.2.3	Catalysts supported on CNTs for the WGS reaction.....	68
4.3	Methodology.....	70
4.3.1	Catalyst synthesis	70
4.3.2	Catalyst characterization.....	72
4.3.2.1	<i>Nitrogen physisorption Isotherms</i>	72
4.3.2.2	<i>X-Ray Diffraction (XRD)</i>	72

4.3.2.3	<i>Transmission Electron Microscopy (TEM) and Energy Dispersive X-Ray Spectroscopy (EDX)</i>	73
4.3.2.4	<i>Raman spectroscopy</i>	73
4.3.2.5	<i>Thermogravimetric Analysis (TGA)</i>	73
4.3.2.6	<i>Hydrogen Temperature Programmed Reduction (H₂-TPR)</i>	74
4.3.2.7	<i>Pulsed CO chemisorption analysis</i>	74
4.3.3	Catalyst activity tests	75
4.3.4	Intrinsic kinetic measurements	76
4.4	Results and discussion	78
4.4.1	Catalyst characterization	78
4.4.1.1	<i>Nitrogen physisorption isotherms</i>	78
4.4.1.2	<i>X-Ray Diffraction</i>	80
4.4.1.3	<i>Transmission Electron Microscopy (TEM)</i>	82
4.4.1.4	<i>Raman spectroscopy</i>	85
4.4.1.5	<i>Thermogravimetric Analysis (TGA)</i>	87
4.4.1.6	<i>Hydrogen Temperature Programmed Reduction (H₂-TPR)</i>	88
4.4.1.7	<i>Pulsed CO chemisorption analysis</i>	89
4.4.2	Catalytic tests	90
4.5	Conclusions	94
5	CHAPTER III: (MACRO)KINETIC STUDY	95
5.1	Introduction	95
5.2	Data for kinetic study	96
5.3	Kinetic modeling and parameter estimation	99
5.4	Model discrimination	103
5.5	Discussion	113
5.6	Conclusions	115
6	CHAPTER IV: MICROKINETIC STUDY	117
6.1	Introduction	117
6.2	Methodology	119

6.3	Results and discussion	122
6.4	Conclusions	125
7	CONCLUSIONS AND SUGGESTIONS FOR FUTURE WORKS	127
	REFERENCES	129
	APPENDIX A – DATABASE FOR ANN MODEL	143
	APPENDIX B – ANN WEIGHTS	145
	APPENDIX C – PYTHON CODE TO ESTIMATE KINETIC PARAMETERS	159

1 INTRODUCTION

The worldwide demand for hydrogen (H_2) production has increased over the last years based on the prognosis of becoming the major energy source in the future, by its use in fuel cells for vehicles – releasing water (H_2O) and few pollutants into the environment – and in the production of high-value synthetic liquid fuels through Fischer-Tropsch process from synthesis gas (a mixture of H_2 and carbon monoxide, CO), also known as syngas or water-gas (SAEIDI *et al.*, 2017). In Brazil, this demand has also increased due to the implementation of petroleum hydrorefining processes in order to comply with the new environmental legislation on fuels (BRASIL; ARAÚJO; SOUSA, 2011).

The most common route for H_2 generation in the Brazilian scenario is presented in Figure 1.1. It comprehends syngas production ($H_2 + CO$) from the steam reforming of natural gas – a fossil fuel resource, which has been studied in a sustainable way by the scientific community – followed by the water-gas shift (WGS) reaction for converting the remaining CO and the excess water into more H_2 , according to the following main chemical equations, respectively (LIMA *et al.*, 2012):

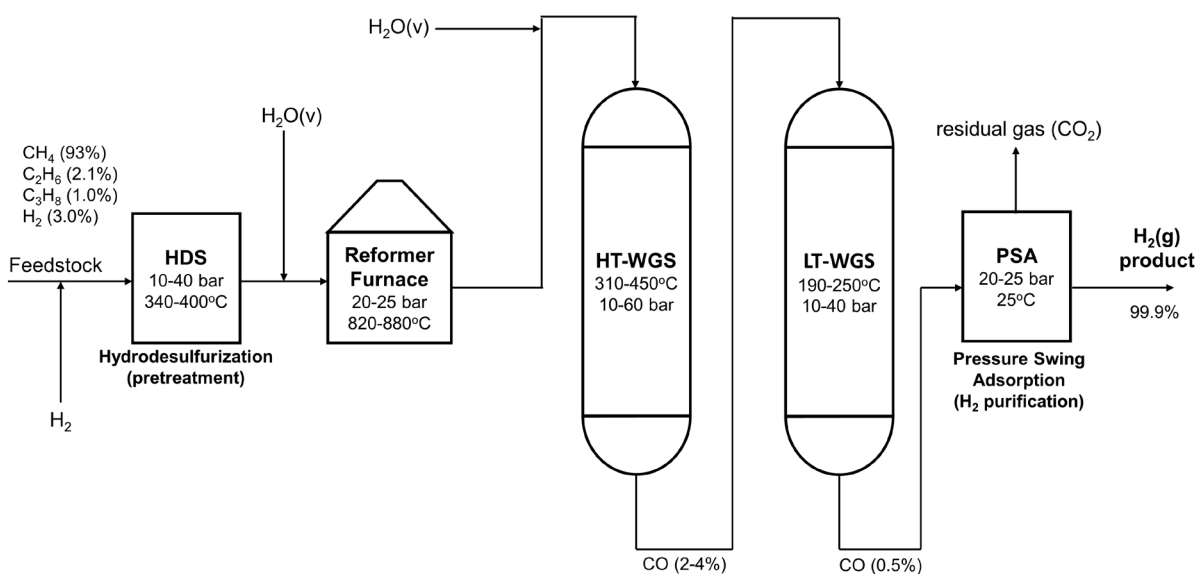
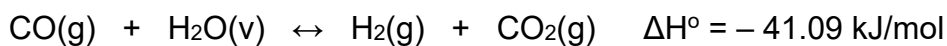
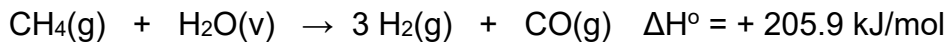


Figure 1.1 – Simplified process flow diagram for H_2 production through steam reforming of natural gas.

Source: Adapted from (BRASIL; ARAÚJO; SOUSA, 2011)

Therefore, the WGS reaction is a very relevant catalytic chemical process for increasing hydrogen production, besides controlling the H₂/CO ratio in reforming reactions, which is very important in the methanol synthesis and gas-to-liquids (GTL) processes, thus valorizing the energetic use of natural gas over oil in a global panorama (PAL *et al.*, 2018). Its importance dates back to 1913, when this reaction encountered its first prominent industrial application as part of the Haber-Bosch process of ammonia synthesis, preventing the iron catalyst deactivation by CO (MENDES *et al.*, 2010). Although the WGS reaction also produces carbon dioxide (CO₂), this greenhouse gas is at a single point and can then be separated from the outlet stream and sequestered (GRADISHER; DUTCHER; FAN, 2015).

As shown in Figure 1.1, the WGS reaction is typically performed in consecutive stages at high (HT, 310-450°C) and low (LT, 180-250°C) temperatures, in which well-established industrial catalysts of Fe₂O₃-Cr₂O₃ and Cu-ZnO-Al₂O₃ are generally employed, respectively (BRASIL; ARAÚJO; SOUSA, 2011). Due to the exothermic reaction reversibility, the former stage aims to promote a rapid CO consumption, being kinetically favorable with the final CO conversion limited by the equilibrium, achieving CO contents between 2-4 vol% in the effluent stream. On the other hand, the latter stage follows the opposite behavior, reaching CO concentrations below 0.5 vol% (LEE *et al.*, 2013).

This very low CO concentration is extremely essential for the platinum electrode used in hydrogen fuel cells (HFCs) since contents greater than 2 ppm can poison it (PAL *et al.*, 2018). The vehicles equipped with these fuel cells can be three times more efficient than gasoline engines (SAEIDI *et al.*, 2017). Hence, the development of new catalysts, more resistant and with suitable characteristics for this type of portable use (e.g. restrictions on volume and weight, tolerance to sulfur compounds, and absence of pyrophoricity), has received great attention in recent years (MENDES *et al.*, 2010).

In this context, the multi-walled carbon nanotubes – MWCNTs – have gained prominence in the catalysis field due to their high surface area and exceptional conductivity properties (SCHMAL, 2016). This allotropic form of carbon, composed of rolled graphene sheets, is generally functionalized with oxygenated organic groups, and it is used as support for catalysts with transition metal nanoparticles (NPs) deposited on its surface (MELCHIONNA *et al.*, 2015). Despite not being yet an economically viable option for large industrial catalytic processes due to the high cost

of their synthesis, the MWCNTs seem to be a more suitable alternative for use in microchannel reactors and portable applications, ensuring energy efficiency, safety and reliability.

In this work, the powerful features of functionalized MWCNTs were combined in a novel catalyst for the WGS reaction with cobalt (Co) nanoparticles as active phase, and promoted by ceria (CeO_2) and strontium (Sr). The choice for Co is due to its tolerance to sulfur – a common natural gas impurity – (MENDES *et al.*, 2010). CeO_2 is used due to its elevated oxygen storage capacity (OSC), which promotes the oxygen species mobility over the catalyst surface as a result of $\text{Ce}^{4+} \leftrightarrow \text{Ce}^{3+}$ redox process, and Sr is used by its virtue of altering the surface oxygen distribution and promoting better interactions between the metal and the support (FIGUEIRA *et al.*, 2018). These catalysts were synthesized and characterized by different techniques and their activities were evaluated at different temperatures under atmospheric pressure.

In addition, in order to describe the WGS reaction kinetics, Artificial Neural Networks (ANNs) were used to observe useful trends and to predict better catalysts and conditions for this process. The increasing use of Machine Learning (ML) techniques – a subarea of Artificial Intelligence (AI) – in Materials Science and Engineering aims to evaluate and improve the performance of materials in their applications, providing insights not easily perceived “by naked eyes” and reducing the number of expensive experiments in laboratory by means of a screening of potential and elucidative experimental conditions (BUTLER *et al.*, 2018). The insertion of properties such as active phase composition, support type, surface area, calcination temperature and time allowed predicting the reaction performance based on intrinsic catalyst variables not commonly used in phenomenological kinetic models.

By the way, a relevant aspect for determining the reaction rate is the formulation of phenomenological kinetic models for the WGS reaction, usually in terms of conventional power-law expressions, or, in the best scenario, of Langmuir-Hinshelwood mechanisms, estimating the kinetic parameters and the reaction orders from experimental data. This task is of utmost importance for reactor design; however, it provides limited information for catalyst design (DUMESIC *et al.*, 1993). These also denoted *macrokinetic* models are constructed starting from the collected data, usually obtained from a differential catalytic reactor – which works at small conversions (~ 5–10%) – by varying temperatures, partial pressures and space velocities (SCHMAL, 2016).

Although *macrokinetic* models have a lower computational cost to predict reaction rates, their applicability is limited to the catalyst and operating conditions employed for generating the data on which their construction was based. Such models do not take into account fundamental catalyst surface phenomena in terms of elementary steps (THYBAUT *et al.*, 2011). Therefore, the development of the so-called *microkinetic* models allowed the scientific community to understand more deeply the determination of the true kinetics of a catalytic reaction, which considers catalyst surface properties, active sites, and elementary steps of the reaction mechanism (SCHMAL, 2016). In this work, this kind of model will be built to describe the WGS reaction kinetics in its elementary steps, considering the catalytic cycles and catalyst surface aspects.

This brief exhibition clarifies the importance of this work for hydrogen production through the WGS reaction using a novel Co catalyst supported on carbon nanotubes and promoted by CeO₂ and Sr. The development of an ANN model to observe useful trends to find an optimum catalyst composition, and the development of kinetic models were evaluated to provide further insights regarding the impact of catalytic elementary surface reactions and intermediate transport limitations on the overall process performance.

This thesis consists of four chapters written in order of publication expectation. The first and last ones were already published, namely:

- CHAPTER I - USE OF ARTIFICIAL NEURAL NETWORKS FOR CATALYST SELECTION (CAVALCANTI *et al.*, 2019)
- CHAPTER II – SYNTHESIS, CHARACTERIZATION AND CATALYTIC TESTS
- CHAPTER III – (MACRO)KINETIC STUDY
- CHAPTER IV – MICROKINETIC STUDY (CAVALCANTI *et al.*, 2020)

2 OBJECTIVES

The main objective of this study is to evaluate new catalysts supported on carbon nanotubes and to develop a kinetic modeling for the WGS reaction to produce hydrogen. The specific objectives are:

- Develop an ANN model to describe the WGS reaction kinetics, besides predicting better catalysts and conditions for the process.
- Synthesize a novel stable catalyst composed of Co as active phase supported on functionalized MWCNTs, and promoted by CeO₂ and Sr.
- Evaluate its catalytic activity for a conventional industrial feed composition at different temperatures and atmospheric pressure.
- Discriminate (macro)kinetic models based on power-law expressions and Langmuir-Hinshelwood mechanisms for the catalyst under study.
- Develop a microkinetic model to determine a more accurate reaction rate for the WGS reaction, considering catalyst surface properties, density of active sites, reaction intermediates, and reaction mechanisms.

3 CHAPTER I – USE OF ARTIFICIAL NEURAL NETWORKS FOR CATALYST SELECTION

3.1 Introduction

The environmental catalysis field has been gaining prominence in the scientific community due to the attempt to reduce the greenhouse gases concentrations in the atmosphere. In this context, hydrogen (H₂) generation is an essential issue for the future since it is considered a non-polluting valuable energy source and the keystone of the new energy economy (SAEIDI *et al.*, 2017).

The Water-Gas Shift (WGS) Reaction ($\text{CO} + \text{H}_2\text{O} \leftrightarrow \text{H}_2 + \text{CO}_2$) is a well-known catalytic chemical process for hydrogen production and control of the H₂/CO ratio in methane reforming reactions. Although there are already well-established industrial catalysts for the WGS reaction, such as Fe₂O₃-Cr₂O₃ and Cu-ZnO-Al₂O₃, for high and low temperature stages, respectively (LIU; SONG; SUBRAMANI, 2009), several new ones have been developed for improving process performance and stability. They are usually composed of transition metal nanoparticles (active phase) – which interact with molecules during the reaction – supported on compounds that disperse the metals, such as inert oxides, alumina, silica, ceria, activated carbon, and carbon nanotubes (LEVALLEY; RICHARD; FAN, 2014).

For predicting better performance in the process, a catalyst selection method for the WGS reaction using Artificial Neural Networks (ANNs) is presented here. This tool is a branch of Artificial Intelligence (AI) based on the human brain behavior that learns tasks from experience (data) through interconnected neurons systems, being considered a Machine Learning (ML) method. ANNs applications in Chemical Engineering have grown over the years since they can replace phenomenological models – which are based on conservation principles and usually exhibit nonlinearity – due to their ability to learn from data without the knowledge of the physical-chemical laws that govern the system (ALVES; NASCIMENTO, 2004). For instance, an ANN model was developed to simulate a silica membrane reactor for methanol steam reforming, presenting good agreement with experimental results and without including fundamental transport equations (GHASEMZADEH; AGHAEINEJAD-MEYBODI; BASILE, 2018).

It is also worth noting that ANNs can approximate complex model equations to perform optimization problems with high-speed processing because of their few non-iterative algebraic calculations (NASCIMENTO; GIUDICI, 1998). This speed and high accuracy were verified in a work that compared the outcomes of a rigorous kinetic mathematical model with an ANN one for describing an industrial hydrogen plant (ZAMANIYAN *et al.*, 2013).

The article entitled “*Can artificial neural networks help the experimentation in catalysis?*” (SERRA *et al.*, 2003) was the milestone for the application of ANNs to kinetics and catalysis, successfully predicting the *n*-octane conversion and yields from partial reactant pressures, reactor temperature, and contact time, during its isomerization reaction catalyzed by Pt-chlorinated alumina. Moreover, the trained ANN was used in a different system with a similar reaction network, requiring a small number of samples to reach good-quality estimations. The ML increasing use in the Materials Science and Engineering fields leads to a reduction in the number of time-consuming and expensive small sets of experiments in the laboratory that attempt to answer scientific questions for improving the material performance (BUTLER *et al.*, 2018).

Specifically, in the field of heterogeneous catalysis, for designing a new catalyst, it is important to know the *past* of the catalysis (SCHMAL, 2016). Therefore, ANNs can be used to select better possible catalysts – cheaper, less toxic and composed of non-precious metals – for a given reaction, thus reducing the massive number of needed high-throughput (HT) experiments, peculiar conjuncture of combinatorial catalysis (BAUMES *et al.*, 2004). A growing number of papers have been published in the Big Data-Catalysis area, such as studies about composition of mixed metal oxides catalysts for the oxidative dehydrogenation of propane to propene through ANNs (HOLEŇA; BAERNS, 2003); the selection of additives for a Co/SrCO₃ catalyst by ANNs for the CO preferential oxidation (KOBAYASHI; OMATA; YAMADA, 2010); the catalyst composition investigation for the oxidative methane coupling with the application of analysis of variance (ANOVA), correlation techniques, and decision trees (ZAVYALOVA *et al.*, 2011); knowledge extraction using ANNs for CO oxidation over Cu (GÜNAY; YILDIRIM, 2011) and Au (GÜNAY; YILDIRIM, 2013) catalysts; the influence of catalyst preparation and operational variables on the CO conversion for the WGS reaction over Au and Pt catalysts (ODABAŞI; GÜNAY; YILDIRIM, 2014); the choice of better catalysts for producing hydrogen from biomass pyrolysis by the analysis of ANNs results (KARACI *et al.*, 2016); and the development of heuristic rules

through decision tree analysis for the steam reforming of methane (BAYSAL; GÜNAY; YILDIRIM, 2017).

This shows the great potential of using these methods to clarify issues not yet well understood by the simple analysis of experimental data or explained by phenomenological models. It is thus noteworthy that there is currently a tendency for review papers to become statistical review articles (ŞENER *et al.*, 2018), aiming not only at reporting what has already been studied about a certain subject in the literature, but also at extracting useful information from the built database. In this work, a databank collected from a review article for the WGS reaction (LEVALLEY; RICHARD; FAN, 2014) was used in a three-layer feedforward neural network to build a more complete model to predict optimal catalyst composition, including an important variable not reported in previous ANNs studies – the surface area. The progress of this work against similar statistical studies in the catalysis area was proposing better catalysts and operating conditions for H₂ production through the WGS reaction by means of the sensitivity analysis investigation of the ANN model developed.

3.2 Methodology

3.2.1 Data selection

The dataset was acquired from tables and/or figures presented in articles cited in a review paper for the WGS reaction (LEVALLEY; RICHARD; FAN, 2014), obtaining 283 experimental data points from bench-scale reactors. These data are available in APPENDIX A. Table 3.1 presents the selected variables for the ANN and their applicability ranges. Only articles that reported these most frequent variables were used to build the database, and a few others, which referred to other parameters, were removed. For the catalyst performance, as can be seen from Figure 3.1, the CO conversion was the most commonly recorded outcome variable (71%) in the review article against the CO consumption rate and others, which were little reported and whose articles were eliminated from the study.

Table 3.1 – Variables selected for the ANN and their ranges

Variable	Unit	Minimum value	Maximum value
Temperature	°C	200	450
Pressure	bar	0.8	27.6
Catalyst mass	g	0.02	2.86
Gas hourly space velocity (GHSV)	h ⁻¹	795	(1200000)**
CO feed composition	vol%	1.30	37.2
H ₂ O feed composition	vol%	1.50	69.2
CO ₂ feed composition	vol%	0	96.0
H ₂ feed composition	vol%	0	62.5
Inert feed composition (N ₂ or He)	vol%	0	96.50
CH ₄ feed composition	vol%	0	0.70
Active phase composition*	wt%	Co, Ni, Cu, Ru, Pd, Ag, Ir, Pt, Au, Cr, Zn	
Support type*	-	Fe ₂ O ₃ , AC, CNT, Mo ₂ C, CeO ₂ , La ₂ O ₃ , ZrO ₂ , MgO, Al ₂ O ₃ , TiO ₂	
Promotor/dopant concentration*	wt%	Na, K, Mg, Ba, B, Al, Si, Pb, S, Hg, Y, Ti, Zr, La, Ce, Fe	
Surface area	m ² /g	1.1	(1487)***
Calcination temperature	°C	25	800
Calcination time	h	0	10
CO conversion	dimensionless	0	1

*categorical or categorical-quantitative variables

**This maximum value reported for GHSV of 1.2×10^6 ml gas/ml catalyst/h (RHODES *et al.*, 2002) is very unusual in catalytic experiment ranges ($\approx 10^4$ h⁻¹), leading to a rather small residence time (0.003 s).

***This maximum value reported for the surface area of 1487 m²/g (BUIRAGO *et al.*, 2012) is well above the normally found catalyst surface area values (100–300 m²/g), since this catalyst support is a special industrial activated carbon prepared from olive stones by direct steam activation.

Source: (CAVALCANTI *et al.*, 2019)

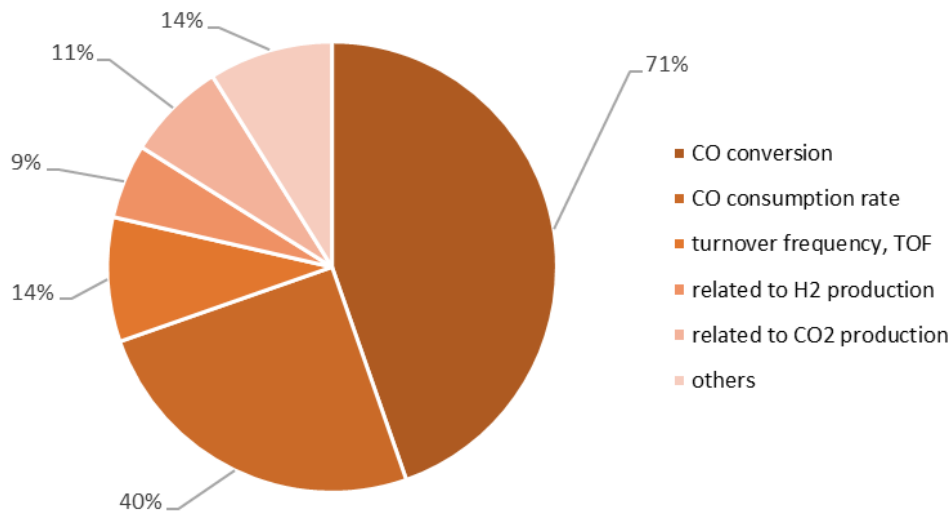


Figure 3.1 – Distribution of the outcome variables reported in the articles cited in the reference review paper (LEVALLEY; RICHARD; FAN, 2014). The sum of the percentages is greater than 100%, since more than one variable can be reported in one article.

Source: (CAVALCANTI *et al.*, 2019)

The input variables for the ANN can be divided into two groups: one related to operating conditions (temperature, pressure, catalyst mass, gas hourly space velocity – GHSV, and feed composition) and other to the catalyst design and textural characteristics (active phase and its composition, support type, promotor/dopant concentration, surface area, and calcination temperature and time). Therefore, the insertion of the latter properties into the model allows predicting the reaction performance based on intrinsic catalyst variables not commonly used in phenomenological kinetic reactor models (PANTOLEONTOS; KIKKINIDES; GEORGIADIS, 2012). In addition, as discussed before, the CO conversion was the only output variable considered.

All these variables are clearly important to describe the WGS reaction system. In particular, unlike other ANN similar works (ŞENER *et al.*, 2018), the choice of using the surface area as an ANN input variable is very pertinent, since this property can demonstrate the interplay extension between reactants molecules and the solid surface. The model proposed attempts to take into account the formation of active catalyst centers, thereby including some variables of the catalyst preparation method, such as calcination temperature and time, and catalyst chemical composition.

3.2.2 Artificial Neural Networks

We employed a three-layer feedforward neural network to model the process, that is, each layer connects to the next, but there is no way back from the “information”, causing all the connections to have the same direction, starting from the input layer towards the output layer. Figure 3.2 shows the ANN diagram with the variables considered. The only assumption of this proposed ANN model is that all the collected data represent the system under study.

The input variables in red are categorical or categorical-quantitative, being represented by one-dimensional zero-arrays with the composition value of the component other than zero (BROUWER, 2004). In other words, these variables were introduced into the ANN through 37 input neurons, in which each neuron corresponds to a chemical compound or a metal composition. As a result, in the totality, 52 neurons were inserted in the ANN scheme with 51 inputs and 1 output.

Although there are other related papers that used two hidden layers in the ANN architecture (GÜNAY; YILDIRIM, 2013), only one layer of this kind was adopted, since there are fewer calculation steps and it is more commonly used in Chemical Engineering applications, presenting good results (ALVES; NASCIMENTO, 2004).

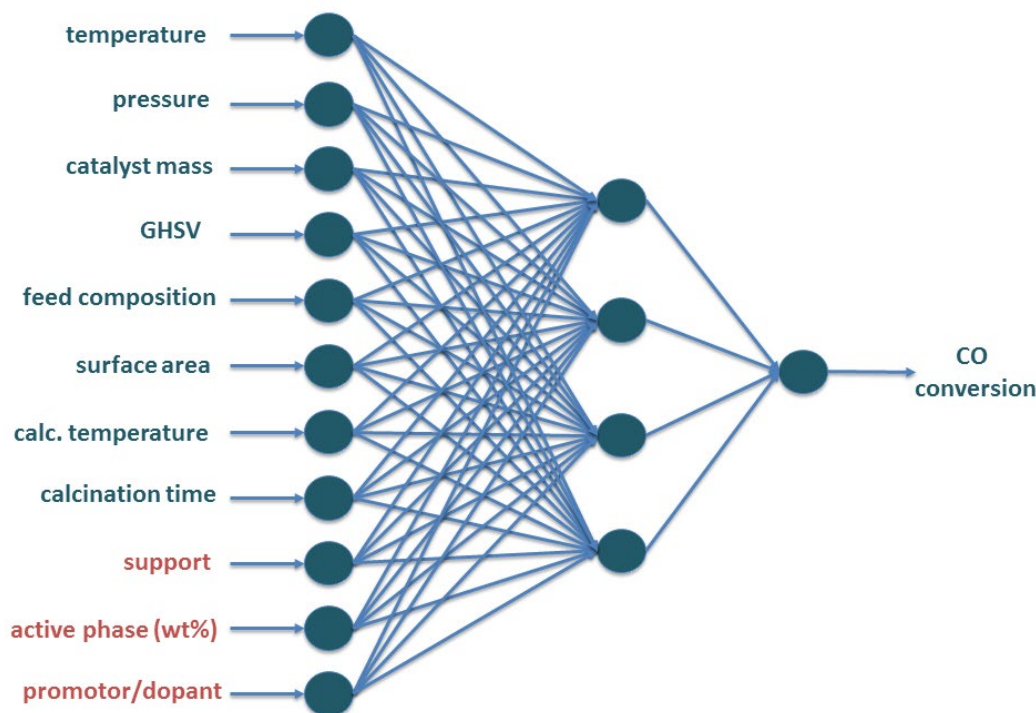


Figure 3.2 – Three-Layer Feedforward Neural Network employed in this work

Source: (CAVALCANTI *et al.*, 2019)

In this kind of ANN, the neurons of a layer are connected to all neurons of the next layer. In other words, each “information” x_i that leaves a neuron of a layer i is weighted by a weight w_{ij} and it is sent to all neurons of the next layer j . Figure 3.3 presents a neuron of a layer j of the ANN structure, and its output o_j is calculated by:

$$o_j(x_i) = f\left(w_{oj} + \sum_{i=1}^n w_{ij}x_i\right) \quad (1)$$

where w_{oj} denotes the intercept, n the number of neurons of the layer i , and f a sigmoid activation function.

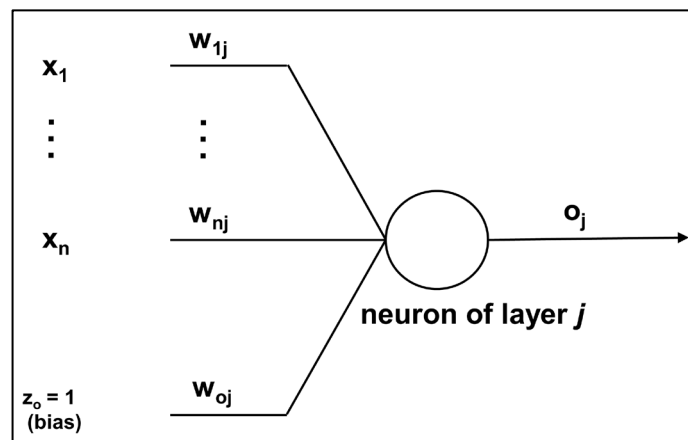


Figure 3.3 – Scheme of a neuron of layer j

Source: (CAVALCANTI *et al.*, 2019)

For the catalytic data adjustment, the **neuralnet** package – version 1.33 – was used (GÜNTHER; FRITSCH, 2010), available in the R software environment. Training an ANN is to estimate the weights w corresponding to the connections between two neurons of consecutive layers, which analogically refers to a synapse – a phenomenon in which information passes from one neuron to another. For this, a large enough dataset is compared to the ANN prediction. This training procedure is interrupted when all the partial derivatives of the error function with respect to weights ($\partial E/\partial w$) are smaller than a given tolerance, for instance, 0.01. The expression for the error function employed was the sum of the quadratic errors between the values observed o_h and those predicted by the ANN y_h , according to Eq. (2).

$$\min(E) = \min \left[\frac{1}{2} \sum_{l=1}^L \sum_{h=1}^H (y_h^{(l)} - o_h^{(l)})^2 \right] \quad (2)$$

in which E indicates the error function, y the observed outputs, o the predicted outputs, L the number of observations and H the output nodes.

The data were pre-processed through the min-max normalization, which ranged their values between 0 and 1, in order to avoid the influence of a variable on the model prediction due to its order of magnitude. Moreover, they were randomly partitioned into two-subsets:

- 80% for the training set, which was used to estimate the ANN weights; and
- 20% for the test set, which was used only to verify the ANN performance.

Note that the test data must belong to the training data domain to avoid extrapolations that frequently lead to predictions subject to uncertainties. The ANN used here has sigmoid activation functions with the bias neuron ($z_0 = 1$) belonging to the intercept.

The algorithm used to train the network was the *Resilient Backpropagation with Weight Backtracking* (RPROP+), which, unlike the traditional Backpropagation algorithm, has a separate learning rate for each weight and can be changed during training. This solves the problem of setting a global learning rate appropriate to the whole network. Instead of the partial derivatives magnitudes, only their signals were used to update the weights, thus ensuring an equal influence of the learning rate on the network. Furthermore, the term *Weight Backtracking* refers to undoing the last weight iteration and adding a smaller value to it in the next step, thereby avoiding the jump over the minimum several times.

To reduce the possibility of overfitting, the neuron number in the hidden layer (NH) was chosen using the *k-fold cross validation* technique. Its basic idea is to re-perform the ANN calculations for different configurations and combinations of training and testing datasets, thus seeking the NH that minimizes the mean squared error (MSE) for the test set. This procedure confirms the applicability of the data extracted from different articles since they were all used for training the ANN (ROTHENBERG, 2008).

3.2.3 Sensitivity analysis

The sensitivity analysis of a process is one of the most important steps in understanding the relationship between their dependent and independent variables. It was carried out for evaluating tendencies, identifying the relevant model variables, and selecting the best catalyst configuration. Table 3.2 shows the input values used during this procedure, considered as a reference.

Table 3.2 – Variables values for the sensitivity analysis

Variable	Unit	Minimum value
Temperature	°C	300
Pressure	bar	1
Catalyst mass	g	0.1
Gas hourly space velocity	h ⁻¹	1000
Surface area	m ² /g	100
Calcination temperature	°C	300
Calcination time	h	4
CO feed composition	vol%	2
H ₂ O feed composition	vol%	10
Inert feed composition (N ₂ or He)	vol%	88
Active phase and its composition	wt%	Cu , 2
Support type	-	CeO ₂

Source: (CAVALCANTI *et al.*, 2019)

The rate of change of the CO conversion, X_{CO} , in relation to a considered input variable ξ is measured by the derivative $\partial X_{CO} / \partial \xi$ calculated at the reference base point, $\bar{\xi}$. However, it is practical to use relative values to the reference – $X_{CO}(\xi) / X_{CO}(\bar{\xi})$ and $\xi / \bar{\xi}$ – so that the result does not depend on the variable units. Therefore, the following equation was used to compute the CO conversion sensitivity analysis related to the ANN input variables (PERLINGEIRO, 2005):

$$S(X_{CO}; \xi) = \left. \frac{\partial [X_{CO}(\xi)/X_{CO}(\bar{\xi})]}{\partial (\xi/\bar{\xi})} \right|_{ref.} = \left. \frac{\partial X_{CO}}{\partial \xi} \right|_{ref.} \cdot \frac{\bar{\xi}}{X_{CO}(\bar{\xi})} \quad (3)$$

where S is the sensitivity, and *ref.* and *the bar* refer to the reference input conditions for performing the analysis described in Table 3.2.

The use of numerical approximation for the derivative in Eq. (3) leads to:

$$S(X_{CO}; \xi) = \frac{X_{CO}(\bar{\xi} + \Delta\xi) - X_{CO}(\bar{\xi})}{\Delta\xi} \cdot \frac{\bar{\xi}}{X_{CO}(\bar{\xi})} = \frac{X_{CO}(\bar{\xi} + \Delta\xi) - X_{CO}(\bar{\xi})}{X_{CO}(\bar{\xi})} \cdot \frac{\bar{\xi}}{\Delta\xi} \quad (4)$$

Taking a 1% increment from the reference values ($\Delta\xi/\bar{\xi} = 0.01$), Eq. (4) becomes:

$$S(X_{CO}; \xi) = \frac{X_{CO}(1.01 \cdot \bar{\xi}) - X_{CO}(\bar{\xi})}{X_{CO}(\bar{\xi})} \cdot 100 \quad (5)$$

and the sensitivity value, S , can be obtained.

3.3 Results and discussion

3.3.1 ANN performance and regression

For determining the number of neurons in the hidden layer, the data were partitioned 10 times ($k = 10$) in different training and testing sets for each NH value considered. Figure 3.4a illustrates the graph of the mean squared error for the testing set as a function of NH as a result of the application of the *k-fold cross validation* technique. As observed, the minimum MSE value occurs at $NH = 12$, and then it begins to rise and oscillate, indicating a possible overfitting. Therefore, 12 neurons were chosen for composing the ANN hidden layer, without loss of quality in the system representation performance, as will be seen in the prediction graphs. Also note that the MSE value for the training set (Figure 3.4b) always tends to decrease with the addition of more neurons – consequently more parameters – into the model, leading to a model overestimation.

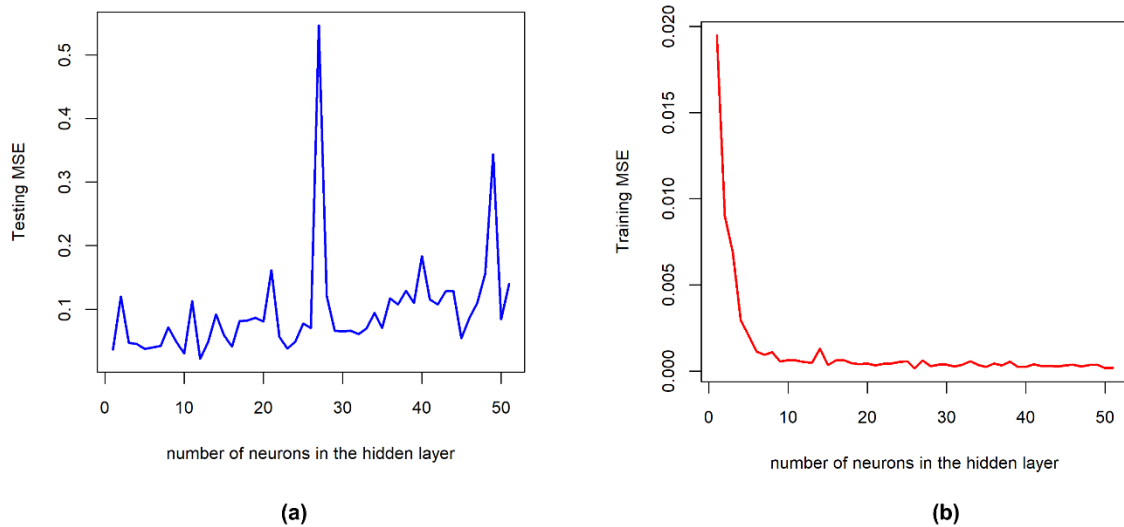


Figure 3.4 – Mean squared error *versus* number of neurons in the hidden layer (a) for the testing set and (b) for the training set.

Source: (CAVALCANTI *et al.*, 2019)

The training process for estimating the ANN weights required 5304 steps to converge, reaching an error of 0.04368. The prediction plot of the CO conversion for the training set is illustrated in Figure 3.5a. The R^2 value was 0.996, indicating an excellent fit of the ANN model to the data of this group. Its mean square error (MSE) between the observed and predicted value was 0.000366. The satisfactory values of these metrics – R^2 and MSE – can be explained by the fact that the training set contains most of the data collected – 80% of the entire dataset – and these data were used to estimate the ANN weights. In addition, the residues histogram (Figure 3.5b) certifies the good prediction agreement, presenting normal behavior with an average of approximately zero.

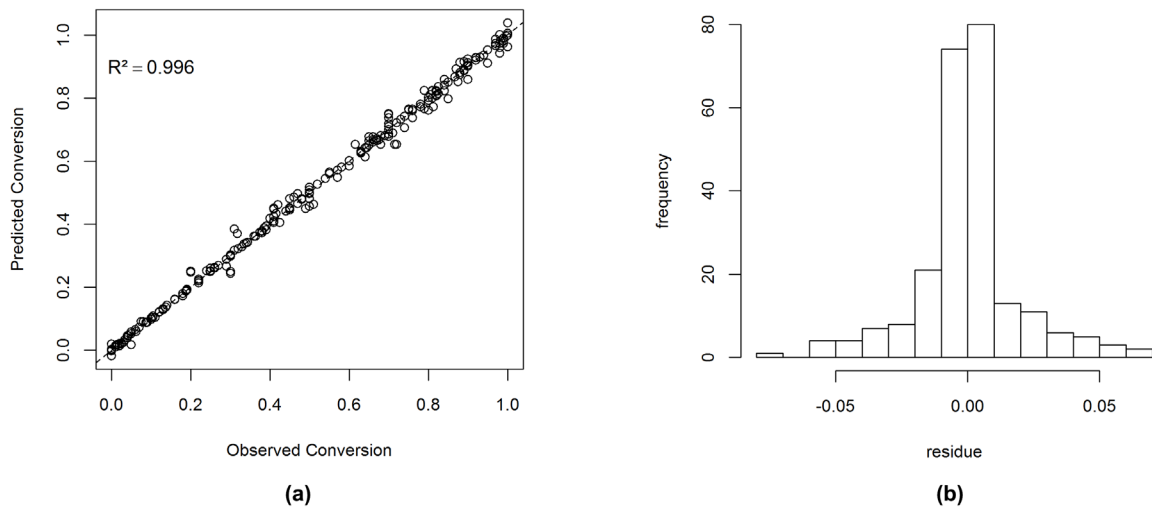


Figure 3.5 (a) Comparison between prediction and observed CO conversion values for the training set
(b) Histogram of residues for the training set.

Source: (CAVALCANTI *et al.*, 2019)

As can be seen in Figure 3.6a, for validating the ANN model, the test set was used, obtaining a R^2 of 0.914 and a MSE of 0.00909 – slightly worse than the previous ones – which show a plausible predictivity ability of the network for the data that were not used to estimate its weights. The residues histogram for this validation is presented in Figure 3.6b, which ratifies the conclusions obtained for this series, resembling a wider normal distribution with a less frequent zero-centered average than the training set.

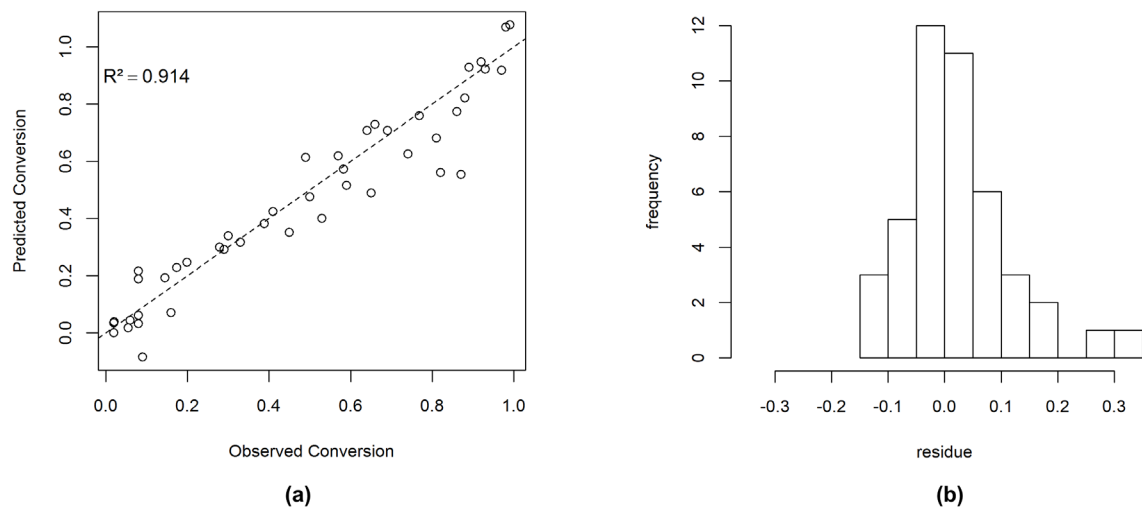


Figure 3.6 (a) Comparison between prediction and observed CO conversion values for the testing set
(b) Histogram of residues for the testing set.

Source: (CAVALCANTI *et al.*, 2019)

Figure 3.7 presents these results for the entire dataset. The values of R^2 (0.983) and MSE (0.00172), as well as the normal shape of the residue histogram, demonstrate an acceptable agreement between the predicted and observed values, and the lack of trend in the adjustment. These numbers lie between the ones related to the training and the testing sets, however closer to the former, since it contains 80% of the whole dataset and it was used to estimate the parameters of the neural network.

An important fact is that few points are not well predicted by the ANN, somewhat away the 45° line. This can be explained by a possible biased selection of the training dataset (BAUMES *et al.*, 2004), or the poor quality of the experimental kinetic data. The latter can be related to reproducibility problems caused by the failure to carry out statistical analyses, the availability of few materials and little time at the laboratory (BAKER; PENNY, 2016).

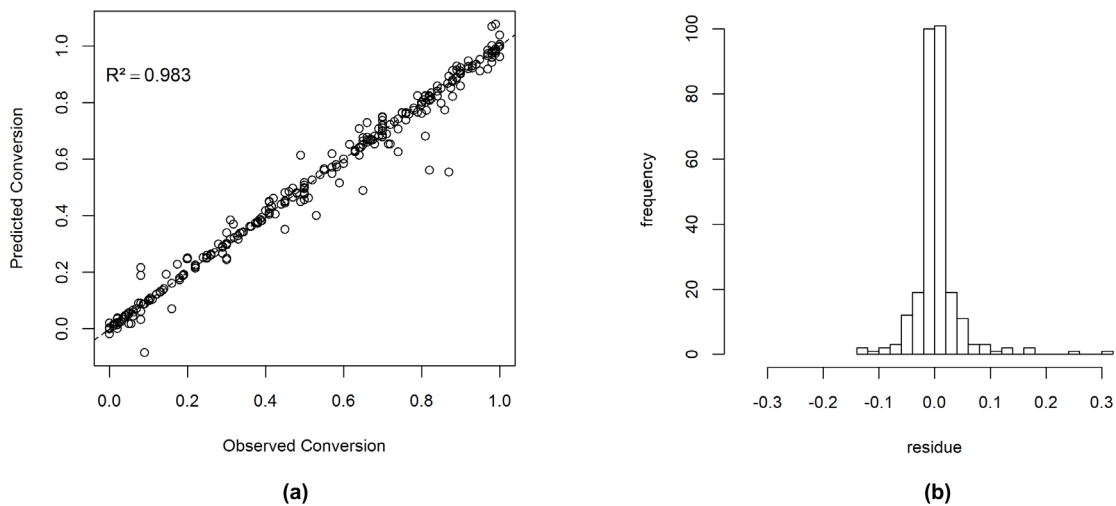


Figure 3.7 (a) Comparison between prediction and observed CO conversion values for all dataset (b) Histogram of residues for all dataset.

Source: (CAVALCANTI *et al.*, 2019)

Figure 3.8 shows the ANN topology with 1 input, 1 hidden and 1 output layer, and the estimated weights computed during the training step. The hidden layer contains 12 neurons ($NH = 12$) – calculated by the *k-fold cross validation* technique. The labels CO, H₂O, CO₂, H₂, N₂, He and CH₄ refer to the feed composition in vol%; the labels Fe₂O₃, AC, CNT, Mo₂C, CeO₂, La₂O₃, ZrO₂, MgO, Al₂O₃, and TiO₂ refer to the support type; the labels Co, Ni, Cu, Ru, Pd, Ag, Ir, Pt, and Au refer to the active phase composition in wt%; and finally, the labels Cr, Zn, Na, K, Mg, Ba, B, Al, Si, Pb, S, Hg, Y, Ti, Zr, La, Ce, and Fe refer to the promotor/dopant concentration in wt%. In

total, there are 51 input neurons and 1 output neuron. Moreover, there are bias neurons ($z_0 = 1$, in blue) belonging to the intercept, not being directly affected by any covariate. This ANN scheme was generated by the **neuralnet** package.

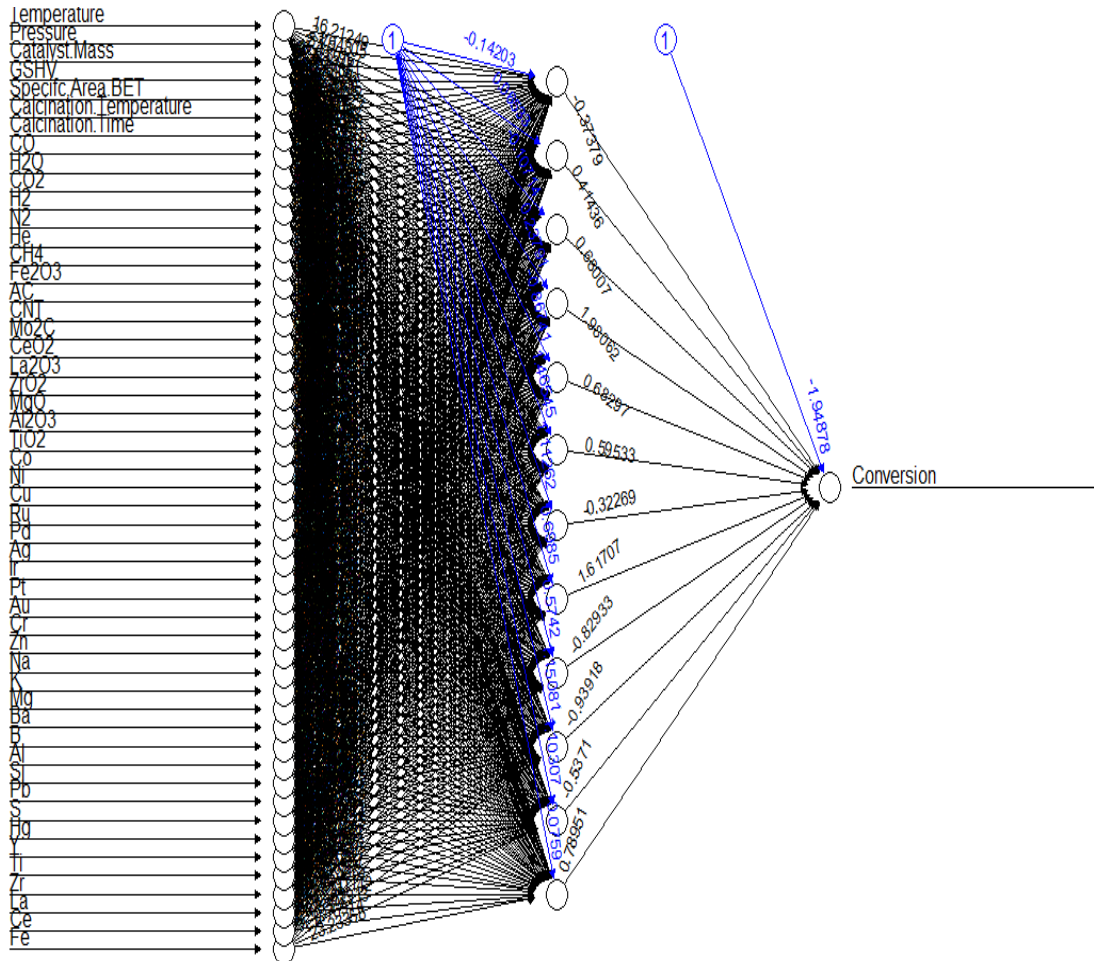


Figure 3.8 – ANN structure with 3 layers – 1 input, 1 hidden and 1 output layer – and the estimated weights computed during the training step (NH = 12, error = 0.04368, steps = 5304).

Source: (CAVALCANTI *et al.*, 2019)

More detailed results related to the ANN regression analysis are shown in APPENDIX B. Table B.1 exhibits the estimated weight values of the developed ANN represented in Figure 3.8.

3.3.2 Sensitivity analysis findings

The sensitivity analysis is an efficacious mechanism for predicting the behavior of the process and for using its results for decision-making. Therefore, this tool was

used with the ANN model to select suitable catalysts for the WGS reaction, besides providing better operating conditions for the process, and identifying crucial variables.

Figure 3.9 shows the CO conversion behavior with the active phase composition in the catalyst (the copper was the metal chosen) and keeping all the other conditions constant. It can be inferred that the higher the active phase composition, the greater the CO conversion due to the higher availability of active sites on the catalyst surface. However, caution must be taken in extrapolating these results since a greater increase in the metal concentration can lead to an agglomeration of particles, reducing their dispersion on the support, and thereby decreasing the catalytic activity.

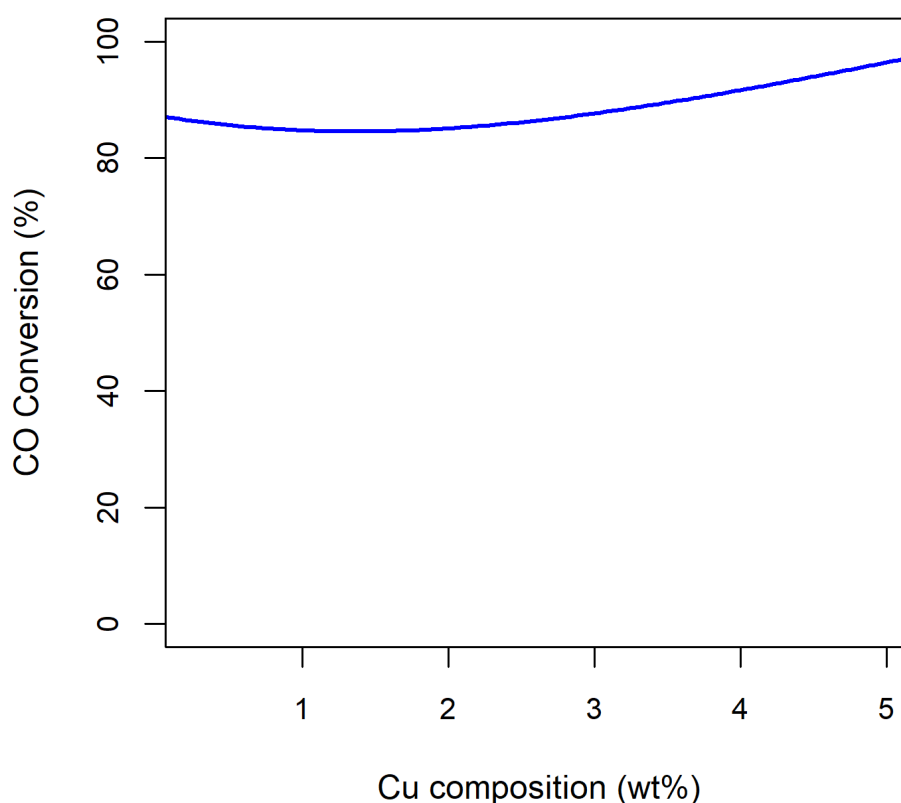


Figure 3.9 – CO conversion *versus* Cu composition (NH = 12, Cu/CeO₂, T = 300°C, P = 1 bar, m_{cat} = 0.1 g, GHSV = 1000 h⁻¹, surface area = 100 m²/g, T_{calc} = 300°C, t_{calc} = 4 h, feed composition: 2% CO, 10% H₂O, 88% N₂).

Source: (CAVALCANTI *et al.*, 2019)

Figure 3.10 presents the CO conversion with the temperature for different active phases (metal composition of 2 wt%). Ru, Ni, and Cu appear as the best metals for improving the catalyst performance for the WGS reaction, requiring further experimental confirmation. Thus, this catalyst selection method took into account

significant information from the review article adopted as a reference (LEVALLEY; RICHARD; FAN, 2014), through the artificial neural network applied to the kinetic data. It would be interesting to compare these results with theoretical molecular models such as the Density Functional Theory (DFT) to support them even more.

In addition, the behavior of the Pd and Co graphs at 300°C suggests the existence of inconsistencies in the ANN model, perhaps caused by the lack of data for these conditions or inconsistent kinetic data. Hence, it would be relevant to have more catalytic data for these metals at this temperature range for a better evaluation.

Furthermore, it is worth mentioning that there are CO conversion values greater than the thermodynamic limit of the WGS reaction and even greater than 100%. This very common occurrence may be due to the small dataset that was used to train the neural network, leading to an overparametrized model (more ANN weights than data used to estimate them). In this way, there are works that recommends performing Principal Component Analysis (PCA) to project the experimental data into an information space with identity regions that exhibit low- and high-predictability, thus scanning the experimental space in a more target manner (SMITH *et al.*, 2020).

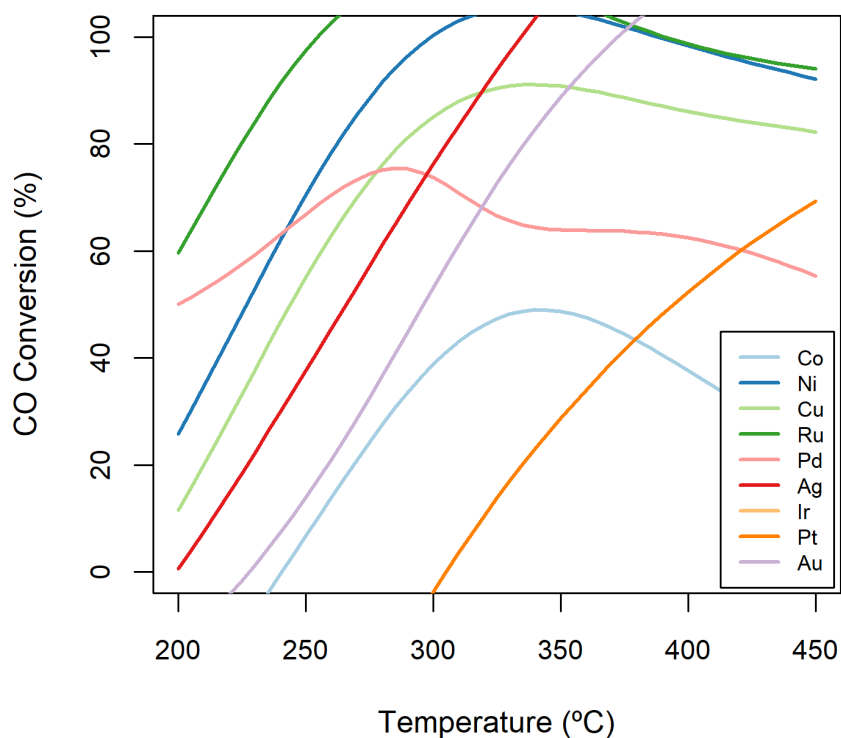


Figure 3.10 – CO conversion *versus* temperature for different active phases (NH = 12, Metal/CeO₂, Metal = 2 wt%, P = 1 bar, m_{cat} = 0.1 g, GHSV = 1000 h⁻¹, surface area = 100 m²/g, T_{calc} = 300°C, t_{calc} = 4 h, feed composition: 2% CO, 10% H₂O, 88% N₂).

Source: (CAVALCANTI *et al.*, 2019)

Figure 3.11 shows the surface plot for the CO conversion as a function of temperature and active phase composition, demonstrating better catalyst efficiency at higher temperatures – explained by the Arrhenius equation – and higher metal composition on the catalytic surface. As can be noted from this graph, the temperature has a higher impact over CO conversion than the active phase composition. However, note that the metals particle size and shape were not considered in this ANN model. The higher the active phase composition, the lower the metal dispersion (larger particle size) and availability to molecules adsorption, leading to a saturation state (ZHANG *et al.*, 2014). Thus, it is more favorable to increase the temperature than the active phase concentration for a better process performance.

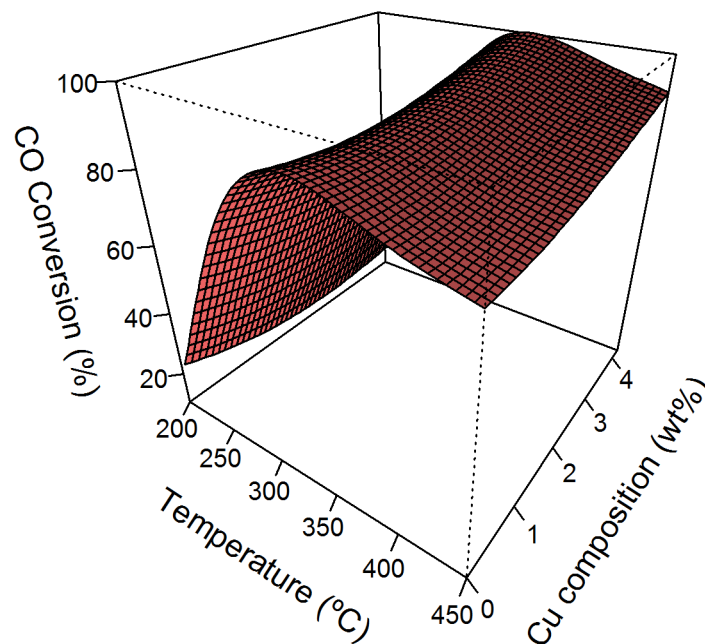


Figure 3.11 – CO conversion *versus* Cu composition and temperature (NH = 12, Cu/CeO₂, P = 1 bar, $m_{\text{cat}} = 0.1 \text{ g}$, GHSV = 1000 h⁻¹, surface area = 100 m²/g, $T_{\text{calc}} = 300^\circ\text{C}$, $t_{\text{calc}} = 4 \text{ h}$, feed composition: 2% CO, 10% H₂O, 88% N₂).

Source: (CAVALCANTI *et al.*, 2019)

As can be observed from Figure 3.12, the CO conversion decreases with the space velocity since the higher the flow through the reactor or the smaller the reactor size, the lower is the contact time of the reactants with the catalyst surface, leading to the non-occurrence of the reaction with the same frequency. However, if the catalyst

deactivation rate is low, high values for the space velocity are recommended (YAGHOBI, 2013). Stability tests need to be carried out to measure this rate. In addition, a decreasing linear dependence of the conversion with the GHSV can be verified, resulting in a constant rate of change between these variables. For this analysis, a consistent range of GHSV values was used, although the literature reports a very high unusual value of $1.2 \times 10^6 \text{ h}^{-1}$ for its extreme (RHODES *et al.*, 2002).

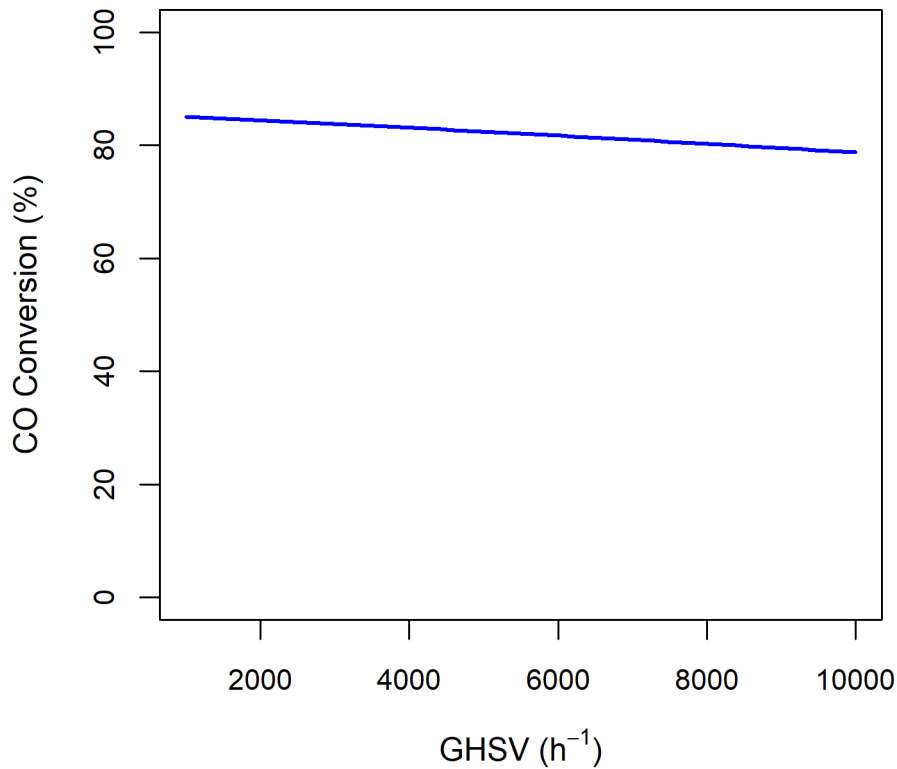


Figure 3.12 – CO conversion *versus* GHSV (NH = 12, Cu/CeO₂, Cu = 2wt%, T = 300°C, P = 1 bar, m_{cat} = 0.1 g, surface area = 100 m²/g, T_{calc} = 300°C, t_{calc} = 4 h, feed composition: 2% CO, 10% H₂O, 88% N₂).

Source: (CAVALCANTI *et al.*, 2019)

Furthermore, Figure 3.13 presents the surface plot of the CO conversion as a function of the temperature and GHSV, once again showing more variability with the temperature. Hence, this variable seems to be the most influential factor in the process, which will be confirmed by the sensitivity calculation at the end of this section. However, when the equilibrium state of the reaction is reached, one must work at lower temperatures to shift the reaction to the production of more hydrogen, since the WGS reaction is exothermic.

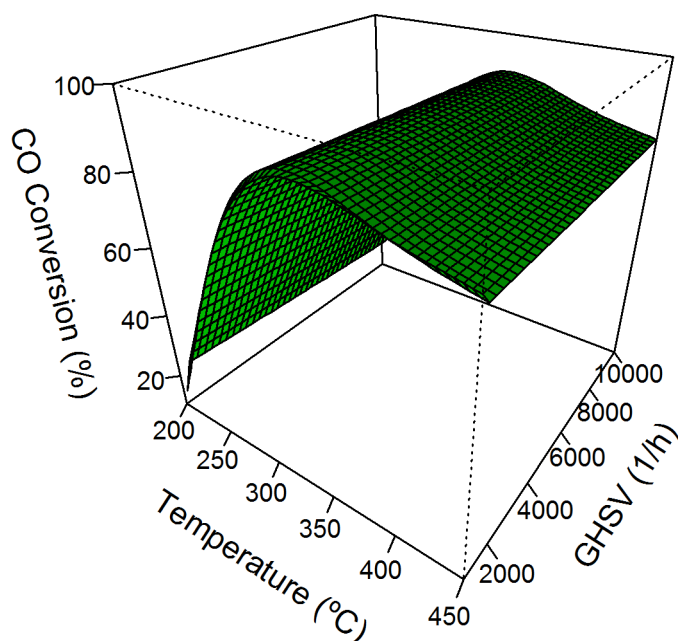


Figure 3.13 – CO conversion *versus* GHSV and temperature (NH = 12, Cu/CeO₂, Cu = 2 wt%, P = 1 bar, $m_{\text{cat}} = 0.1$ g, surface area = 100 m²/g, $T_{\text{calc}} = 300^{\circ}\text{C}$, $t_{\text{calc}} = 4$ h, feed composition: 2% CO, 10% H₂O, 88% N₂).

Source: (CAVALCANTI *et al.*, 2019)

The importance of the feed composition, mainly the steam/CO ratio, was also investigated. In Figure 3.14, the CO conversion shows to slightly grow with the increase of the steam/CO ratio, and the additional amount of H₂O appears to be an excess reagent. This small increase in the conversion can be explained there being more H₂O available to occupy the remaining available sites on the catalyst surface for conducting the reaction. In addition, the presence of H₂ and CO₂ in the feed (reformat case) seems to shift the equilibrium of the reactants, thus decreasing the conversion. In this case, the curve behavior seems to be somewhat incoherent, suggesting that the model was extrapolated under these conditions, thus requiring more data in this interval for a better representation.

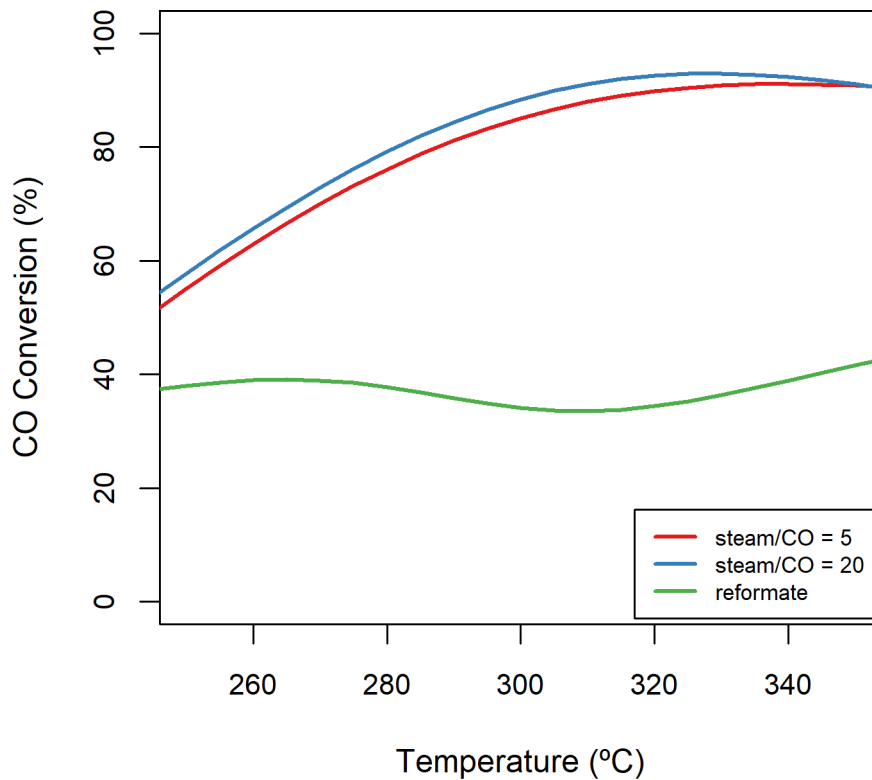


Figure 3.14 – CO conversion *versus* temperature for different feed compositions (NH = 12, Cu/CeO₂, Cu = 2 wt%, T = 300°C, P = 1 bar, m_{cat} = 0.1 g, GHSV = 1000 h⁻¹, surface area = 100 m²/g, T_{calc} = 300°C, t_{calc} = 4 h, feed composition: 2% CO, 10% H₂O, 88% N₂ – steam/CO = 5 (reference); 2% CO, 40% H₂O, 58% N₂ – steam/CO = 20; 10.7% CO, 28.6% H₂O, 5% CO₂, 39.3% H₂, 16.4% N₂ – reformat).

Source: (CAVALCANTI *et al.*, 2019)

Regarding the calcination temperature, Figure 3.15 illustrates its influence on the CO conversion. The latter slightly rises with the former. In fact, the calcination process changes the catalyst textural and morphological features, altering its surface area, pore volumes, particle sizes, metal dispersion, and structures (SCHMAL, 2016). In this case, there was a catalytic activity enhancement, possibly as a result of the precursors removal from the material matrix (through the decomposition of nitrate or sulphate compounds), thus increasing the catalyst surface area, as an example. Nevertheless, it is of considerable importance to pay attention to the catalyst deactivation when working at higher temperatures owing to its sintering or to the agglomeration of its particles.

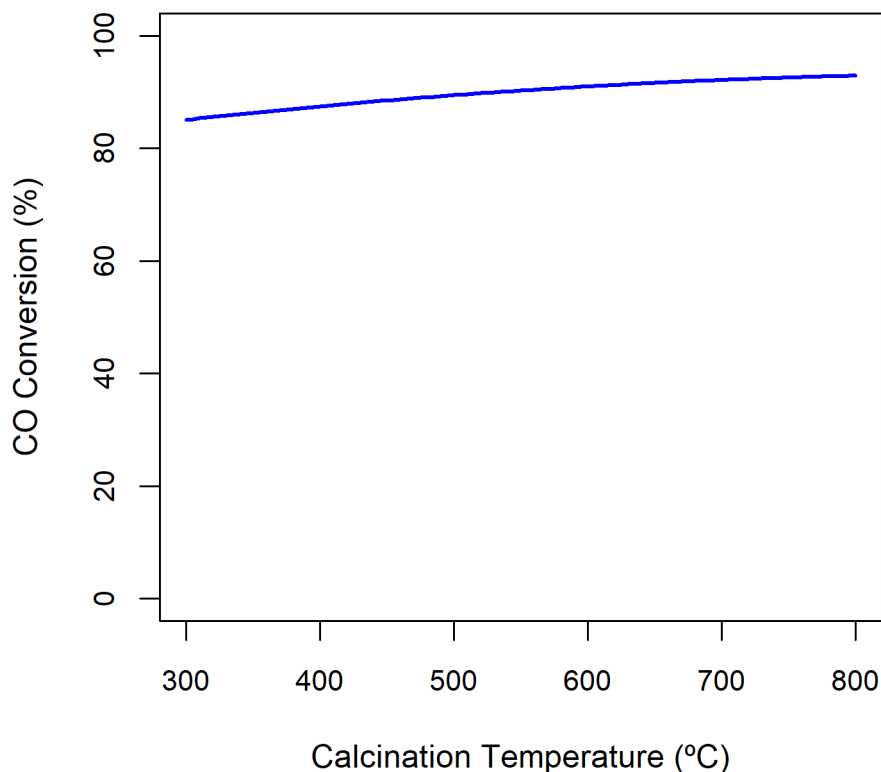


Figure 3.15 – CO conversion *versus* calcination temperature (NH = 12, Cu/CeO₂, Cu = 2 wt%, T = 300°C, P = 1 bar, m_{cat} = 0.1 g, GHSV = 1000 h⁻¹, surface area = 100 m²/g, t_{calc} = 4 h, feed composition: 2% CO, 10% H₂O, 88% N₂).

Source: (CAVALCANTI *et al.*, 2019)

The surface area establishes the extension of the energy interaction between gas molecules and the solid surface through adsorption-desorption phenomena. As can be inferred from Figure 3.16, the higher this parameter, the greater the CO conversion, likely due to there being more available area for the active sites formation. These can be defects on the catalyst surface – holes, edges, or corners – which cause forces that attract reactant molecules to the surface (SCHMAL, 2016). This parameter seems to have a notable influence on the process efficiency due to its higher slope (rate of change) in relation to other studied parameters related to the catalyst design. In addition, it should be noted that, for this analysis, a coherent range of catalyst surface area values was used (100–300 m²/g), although a very high atypical value of 1487 m²/g is reported elsewhere (BUIRAGO *et al.*, 2012).

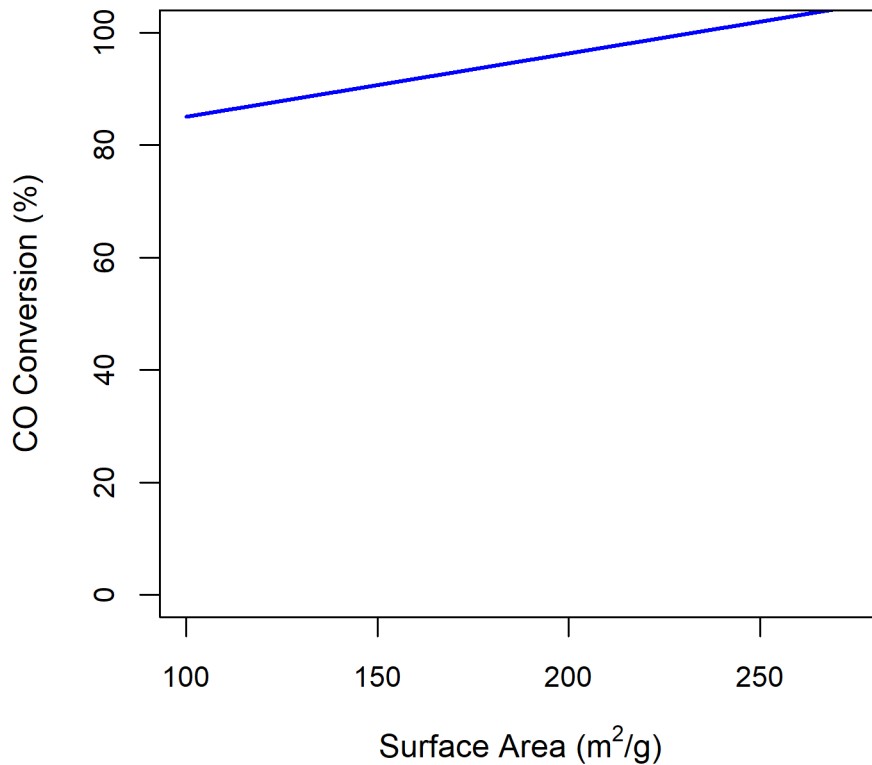


Figure 3.16 – CO conversion *versus* surface area (NH = 12, Cu/CeO₂, Cu = 2 wt%, T = 300°C, P = 1 bar, m_{cat} = 0.1 g, GHSV = 1000 h⁻¹, T_{calc} = 300°C, t_{calc} = 4 h, feed composition: 2% CO, 10% H₂O, 88% N₂).

Source: (CAVALCANTI *et al.*, 2019)

The results of the sensitivity calculations by applying Eq. (5) are presented in Table 3.3. The positive values mean that the quantities have the same behavior in the process: when one of them goes up, the CO conversion also goes up. In turn, the negative values imply the opposite, when an input variable goes up, the CO conversion comes down. The higher the sensitivity value, the greater this influence on the reaction performance. These characteristics were observed in the previous graphs, confirming that the temperature and the surface area are the most influential variables in the process.

Table 3.3 - CO conversion sensitivities related to the considered input variables.

Type of variable	Variable	Sensitivity
Catalyst design and texture	Cu composition	0.0389
	Surface area	0.424
	Calcination Temperature	0.0917
	Calcination Time	0.0197
Operating conditions	Temperature	1.14
	GHSV	-0.00740
	CO feed composition	0.0365
	H ₂ O feed composition	0.0180
	Inert feed composition	-0.0777

Source: (CAVALCANTI *et al.*, 2019)

3.3.3 Discussion

This work provides better guidelines for improving the managed use of the environment in relation to the catalytic production of hydrogen – a relevant zero emission fuel – through the WGS reaction using ANNs. The good management of the catalyst and operating conditions leads not only to a higher production of this non-polluting energy source but also to a reduction in the process energy expenditure due to the choice of higher conversion catalysts at lower temperatures.

The ANN regression presented good quality of the data adjustment, being demonstrated by the computed R^2 values (0.996 for the training set and 0.914 for the testing set). These results are in accordance with similar statistical review studies that also adopted this approach for analyzing different catalytic reactions. For instance, values of 0.986 / 0.944 for Selective CO Oxidation over Cu-based catalysts (GÜNAY; YILDIRIM, 2011), 0.962 / 0.922 for CO Oxidation over Au catalysts (GÜNAY; YILDIRIM, 2013), 0.972 / 0.905 for Water-Gas Shift Reaction over noble metal catalysts (ODABAŞI; GÜNAY; YILDIRIM, 2014), and 0.97 / 0.89 for Dry Reforming of Methane (ŞENER *et al.*, 2018) related to the training and testing sets were reported, respectively. As discussed earlier, the highest values for the training R^2 compared to the testing R^2 is explained by the former set containing most of the data, and it was used to estimate the ANN weights.

Unlike previous studies, a detailed sensitivity analysis using the developed ANN model was performed to examine the process behavior and to predict the dominant parameters to control it. An essential finding of this investigation is the proposition for future works on the WGS reaction of ceria-supported catalysts that exhibit larger surface areas, with Ru, Ni or Cu as active phases performed at medium temperatures ($\approx 300^\circ\text{C}$) and with plausible space velocities ($2000\text{--}6000\text{ h}^{-1}$).

As can be noted in Table 3.3, the variables related to the operating conditions have a slightly higher effect in the CO conversion than those associated to the catalyst design and textural characteristics, mainly because of the temperature, which exhibited the greatest sensitivity value (1.14). This makes sense, since all the reactions are strongly temperature-dependent, as demonstrated by the Arrhenius Equation. Nonetheless, the surface area presented the second highest value (0.424), indicating its importance to the development of industrial catalysts for the WGS reaction.

The relevance of the latter variable in the catalytic performance of the WGS reaction is observed in the literature. For example, higher surface area catalysts of Pt/CeO₂ ($187\text{ m}^2/\text{g}$) presented much higher activity than those with lower surface area ($78\text{ m}^2/\text{g}$) (JAIN *et al.*, 2015) due to the presence of more defect sites, thus attracting more molecules of CO and H₂O to the surface and favoring the reaction. Therefore, the novelty in including the surface area in the ANN model for the WGS reaction was really decisive since it was possible to verify its great influence on the process.

The neural network developed contributes to analyzing the past of the WGS reaction catalysis to design new catalysts for a more efficient process. However, the results from this empirical model are to be compared with advanced chemical theories, which explain the surface and interfacial phenomena of a catalyzed chemical reaction, such as the Density Functional Theory (DFT). Thereby, one can obtain more solid conclusions that justify the formulation of these new materials. Nevertheless, the ANNs are a good starting point for making a decision.

Also, note that most of the articles reported the CO conversion as the key variable for their conclusions. Nonetheless, we advise and encourage researchers in the catalysis field to publish the “real” reaction rate expressed by the turnover frequency (TOF), which considers the number of available active sites – information that can be acquired from the determination of the catalyst surface properties, such as the CO chemisorption or *in situ* characterization techniques – DRIFTS, XPS, Raman, and X-ray diffraction.

For developing future ANN models, it is essential to introduce more input variables in the network, taking into account the formation of active centers on the catalysts and the process mechanism. However, the conditions for creating active centers are not yet predictable due to the weakness of the catalyst preparation theory. It is based on a combination of various factors. In this work, some of these variables were introduced, for example, the catalyst composition (active phase, support and promotor), the calcination conditions, and the surface area. Nonetheless, we recommend that the scientific community reports more catalyst *micro*properties in papers (for being additional ANN inputs), for example, data from the X-ray Photoelectron Spectroscopy (XPS), such as the oxidation state, the phase dispersion on the surface, and the dependence of the atomic concentration with depth (SCHMAL, 2016). In addition, the report of how the reaction occurs at molecular level through the Temperature-Programmed Surface Reaction (TPSR) technique coupled to a mass spectrometer or DRIFTS can improve the ANN results with information about adsorbed species on the catalyst surface, reaction intermediates, elementary steps, and the catalytic function of each compound (ZHU; WACHS, 2016).

3.4 Conclusions

The use of ANNs showed interesting relationships among operational and catalyst design variables for the WGS reaction. In this chapter, a more complete model for this process in the environmental field was successfully developed from a catalytic review paper dataset, exhibiting the powerful tool of ANNs for predicting better catalysts and operating conditions through a sensitivity analysis. A relevant result for a better process performance is the use of larger surface area ceria-supported catalysts for the WGS reaction with Ru, Ni or Cu as active phases carried out at moderate temperatures ($\approx 300^{\circ}\text{C}$) and with reasonable space velocities (2000–6000 h^{-1}).

Furthermore, it was possible to predict some of the most relevant variables that influence CO conversion, such as the temperature and the surface area. Thus, the novelty in relation to previous similar ANNs studies of the insertion of this latter variable into the model was essential for its good predictive performance.

4 CHAPTER II – SYNTHESIS, CHARACTERIZATION AND CATALYTIC TESTS

4.1 Introduction

The worldwide demand for hydrogen (H₂) has increased over the last years steered by the growing number of environmental policies around the world to render it into the main clean energy source in the future (INTERNATIONAL ENERGY AGENCY, 2019). Its key applications are found in vehicle fuel cells – releasing almost only water, rather than carbon dioxide, into the environment – and in the production of high-value synthetic liquid fuels through the Fischer-Tropsch Synthesis (LEVALLEY; RICHARD; FAN, 2014; SAEIDI *et al.*, 2017). In this scenario, the Water-Gas Shift (WGS) Reaction ($\text{CO} + \text{H}_2\text{O} \rightleftharpoons \text{H}_2 + \text{CO}_2$) is a very relevant catalytic process for hydrogen production. It occurs e.g. during methane reforming and controls the H₂/CO ratio in the syngas (LEE *et al.*, 2013). In addition, the WGS reaction has received great importance worldwide because of the use of H₂ in chemical industry with application such as ammonia, fertilizers, methanol, oil refining, etc. (REDDY; SMIRNIOTIS, 2015). The WGS is typically performed in consecutive stages at high temperature (HT, 310-450°C) and low temperature (LT, 80-250°C), in which well-established industrial catalysts such as Fe₂O₃-Cr₂O₃ and Cu-ZnO-Al₂O₃, respectively, are generally employed. Ultimately, CO concentrations below 0.5 vol% in the effluent stream are achieved (BRASIL; ARAÚJO; SOUSA, 2011).

An extremely low CO concentration is required for the platinum electrode used in hydrogen fuel cells (HFCs) as CO acts as a poison when its content exceeds 2 ppm (PAL *et al.*, 2018). Also, the syngas derived from the gasification of waste, biomass, and coal has a higher CO content and impurities such as tar and sulfur, which can poison the catalyst (LEE *et al.*, 2023). Hence, the development of new WGS catalysts, which are more resistant to deactivation and exhibit suitable characteristics, e.g., restrictions on volume and weight, tolerance to sulfur compounds and are not pyrophorous, have received considerable attention in recent years (MENDES *et al.*, 2010). Studies were mainly focused on catalysts based on noble transition metal nanoparticles dispersed and supported on oxides, especially on ceria (CeO₂) (PAL *et al.*, 2018). This high dispersion of the active phase on CeO₂ reduces the content of

precious metals in the catalyst matrix and, consequently, their exorbitant cost, while maintaining their high catalytic activity (ZHOU *et al.*, 2023).

The extensive use of CeO₂ – a reducible oxide with several oxidation states – in current studies as a WGS catalyst support is related to its high oxygen storage capacity (OSC). This promotes mobility of the oxygen species over the catalyst surface as a result of the Ce⁴⁺ ↔ Ce³⁺ redox process. This stimulates a strong interaction between the metal and the support, thus enhancing the catalytic activity (GRADISHER; DUTCHER; FAN, 2015). Currently, due to the low availability of ceria, there is a tendency to synthesize optimized CeO₂-promoted catalysts for the WGS reaction supported on high surface area compounds, such as activated carbon (PASTOR-PÉREZ; BUITRAGO-SIERRA; SEPÚLVEDA-ESCRIBANO, 2014) and carbon nanotubes (DONGIL *et al.*, 2016). These carbon-based catalysts present incredibly high activity, reaching a CO conversion in the range of 80-100%. This high CO conversion is particularly high when paired with an additional dopant metal, such as sodium, Na (ZUGIC; BELL; FLYTZANI-STEPHANOPOULOS, 2014), or strontium, Sr (FIGUEIRA *et al.*, 2018).

In this context, the multi-walled carbon nanotubes (MWCNTs) have gained prominence in the catalysis field because of their high surface area and exceptional conductive properties related to the extended π -conjugation bonds, in which there is the delocalization of π -electrons across all the adjacent aligned p-orbitals (SCHMAL, 2016). This allotropic form of carbon with sp² hybridization, composed of rolled graphene sheets, is generally functionalized with oxygenated organic groups to create anchoring points (i.e., *defects*) for the deposition of metal nanoparticles on their surface (MELCHIONNA *et al.*, 2015). They are considered to be a promising catalyst support because of their capability of dispersing these active metal particles and facilitating electron transfer among them. Next, they exhibit a high resistance to carbon formation, coke deposition, and sintering (SCHMAL; TONIOLO; KOZONOE, 2018). Furthermore, their mesoporous structure minimizes the limitations imposed by mass transfer, as seen in activated carbon (FIGUEIRA *et al.*, 2018).

In this work, the powerful features of these MWCNTs were combined in a novel catalyst with cobalt (Co) as the active phase, and promoted by reduced amounts of CeO₂ and Sr. The choice for Co is related to its industrial relevance in alloys, batteries and catalysts, requiring a more competitive price in comparison to precious metals (as

palladium, platinum, and gold) (ECONOMICS, 2021), and its high tolerance to sulfur, a typical natural gas impurity (HLA *et al.*, 2011a)

The synthesized catalyst was characterized in detail to determine its properties and structure, and its catalytic activity for the WGS reaction was investigated at atmospheric pressure and temperatures ranging from 200 to 450°C and space times varying between 20 and 80 kg s mol⁻¹.

4.2 Literature review

This section includes a review of the state-of-the-art for the WGS reaction catalysts, besides the gradual employment of carbon nanotubes in catalysis. The most recent articles involving the use of catalysts supported on MWCNTs for the WGS reaction are reported and discussed, finding thus the gaps in the literature and the suitable directions for conducting further research on this topic.

4.2.1 Catalyst for the WGS reaction

The choice of the catalyst for the WGS reaction is a key design issue to produce H₂ in large-scale from syngas. (PAL *et al.*, 2018) suggested the following classification of the catalysts that have been frequently employed in this process:

- High temperature shift (HTS) catalysts.
- Low temperature shift (LTS) catalysts.
- Ceria and noble metal based catalysts.
- Carbon based catalysts; and
- Nanostructured catalysts.

The first two types of catalysts are successfully used in the traditional two-stage industrial process. As previously mentioned, the reaction is favored kinetically at higher temperatures and thermodynamically at lower temperatures and is unaffected by changes in pressure (SMITH R J; LOGANATHAN; SHANTHA, 2010). The HTS catalysts are composed by iron-chromium oxides (Fe₂O₃-Cr₂O₃). For activating it, hematite (Fe₂O₃) has to be reduced to magnetite (Fe₃O₄), which is the active phase.

Cr_2O_3 prevents the catalyst sintering and functions as a promoter; however, it is not environmentally friendly due to its carcinogenic nature and the toxicity of the water soluble Cr^{6+} ions. On the other hand, the LTS catalysts are usually constituted by $\text{CuO-ZnO-Al}_2\text{O}_3$. Copper metal crystallites compose the active phase and the $\text{ZnO-Al}_2\text{O}_3$ provides the structure for preventing its sintering. Moreover, ZnO still prevents against poisoning by sulfur and chlorine compounds present in the gas feed (RATNASAMY; WAGNER, 2009).

Nevertheless, those aforementioned catalysts present some drawbacks for use in portable fuel cells because of volume and weight restrictions, pyrophoricity, need for activation, chromium environmental harmfulness, deactivation in presence of condensed water or due to coke formation, among others. For this type of application, catalysts based on noble metals such as gold (Au) and platinum (Pt) at nanoscale and supported on oxides – especially on ceria (CeO_2) – have received great attention in recent years (POTDAR *et al.*, 2011; RODRIGUEZ, 2011).

Recently, Au nanoparticles supported on Zn-Al/Cr/Fe layered double hydroxides were evaluated for the WGS reaction, presenting an enhancement of the activity of these hydroxides (MENG *et al.*, 2020). The addition of Au altered the redox circles on the surface of the catalysis, by significantly lowering the activation barrier of the kinetically relevant step of H_2O dissociation.

The very large use of CeO_2 – a reducible oxide with several oxidation states – in current studies as a WGS catalyst support is due to the fact that this rare earth oxide has an oxygen storage capacity (OSC) that promotes the oxygen species mobility over the catalyst surface as a result of $\text{Ce}^{4+} \leftrightarrow \text{Ce}^{3+}$ redox process, stimulating a strong interaction between the metal and the support, hindering the active phase agglomeration, and enhancing thus the catalytic activity (GRADISHER; DUTCHER; FAN, 2015). Moreover, the addition of transition metals, as zirconium (Zr), or rare earth metals, as lanthanum (La), in the ceria lattice can increase this effect (LIANG; VESER, 2012).

In the WGS reaction, CO adsorbed on metal site is oxidized with the lattice oxygen atom on the CeO_2 surface to form CO_2 , which is accompanied by the formation of surface oxygen vacancy. Then, this vacancy is replenished by the O^* species originated from the dissociation of H_2O to yield H_2 (CHUNG *et al.*, 2021). For example, the LT-WGS activity of a Cu@CeO_2 catalyst was about three times higher than that of a pristine Cu catalyst without CeO_2 (LI *et al.*, 2023).

Currently, due to the low ceria availability, there is a tendency to synthesize optimized CeO₂-promoted catalysts for the WGS reaction supported on high surface area compounds, such as activated carbon (PASTOR-PÉREZ; BUITRAGO-SIERRA; SEPÚLVEDA-ESCRIBANO, 2014) and carbon nanotubes (DONGIL *et al.*, 2016), reducing thus the ceria amount in the catalyst composite and enhancing the synergy between the active phase and CeO₂ because of the capacity for achieving large ceria dispersions (BUITRAGO *et al.*, 2012). These carbon-based catalysts present extremely high activity, particularly if paired with an additional dopant metal, as sodium (ZUGIC; BELL; FLYTZANI-STEPHANOPOULOS, 2014). Also, transition metal carbides, such as Co-Mo/C, exhibit high activity and sulfur resistance, but they are deactivated during the reaction (NAGAI *et al.*, 2010).

Furthermore, it is noteworthy that the activity of nanostructured catalysts is strongly changed by the particle shape and size. For example, in transition metal NPs, size reduction effects lead to differentiated changes in relation to their bulk form in its electronic structure, providing new reactivity features (SCHMAL, 2016). The enhanced performance of these kind of catalysts for the WGS reaction is reported elsewhere and can be attributed to the uniform distribution of metal NPs on the support surface due to their small size, preventing thus sintering and agglomeration (JEONG *et al.*, 2015).

4.2.2 Use of carbon nanotubes in catalysis

Carbon nanotubes (CNTs) are considered one of the most significant pillars of Nanotechnology due to the combinations of their electronic, thermal and mechanical properties. The scientific community interest in potential applications of CNTs has grown rapidly, for example, in composites, electronics, computers, medicine efficiency, sensors, among others (LOOS, 2014). A CNT is an allotropic form of carbon, such as graphene and diamond, which is constituted by a hollow tubular structure of hexagonally arranged carbon atoms with sp² hybridization, such as a rolled graphene sheet. This cylinder has diameters of 2-50 nm, a length of a few micrometers, and extremes that may be open or closed with half of a fullerene (LOOS, 2014). They can be constituted by an unique single wall (SWCNTs – Single-Walled Carbon Nanotubes) or by multiple concentric walls (MWCNTs – Multi-Walled Carbon Nanotubes), as shown in Figure 4.1 (RIBEIRO *et al.*, 2017).

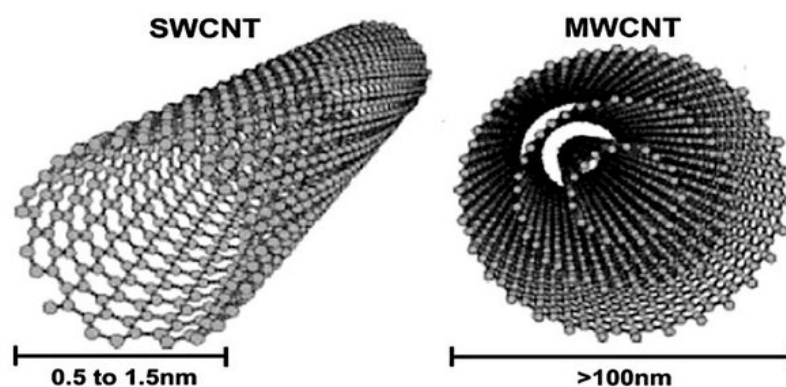


Figure 4.1 – Schematic representation of SWCNTs and MWCNTs.

Source: Adapted from (RIBEIRO *et al.*, 2017)

Due to its high surface area and its conductivity properties related to the extended π -conjugation and Van der Waals forces exerted between individual tubes, CNTs have been employed in new branches, such as in catalytic processes and adsorption systems for hydrogen storage (SCHMAL, 2016). In catalysis, MWCNTs are generally used as supports for catalysts with transition metal NPs deposited on their surface, or even as crude catalysts (MELCHIONNA *et al.*, 2015). To facilitate the anchoring of these NPs and their catalytic activity, the surface of the nanotubes are normally functionalized with oxygenated organic groups (MELCHIONNA *et al.*, 2015). In addition, this functionalization enables to obtain the nanotubes as uniform as possible in size, besides removing various undesirable impurities such as catalyst particles used in their synthesis, graphite and amorphous carbon (LOOS, 2014).

The functionalization by oxidative treatment using HNO_3 is efficient in the removal of carbonaceous impurities, generating several functional groups on the surface and at the extremes of the nanotubes, such as carboxylic ($-\text{COOH}$), hydroxyl ($-\text{OH}$), and carbonyl ($-\text{CO}$) groups, according to Figure 4.2 (ZUGIC; BELL; FLYTZANI-STEPHANOPOULOS, 2014). The oxidation occurs at the extreme of the nanotube and moves to the outermost layer of the bundle. In the case of MWCNTs the oxidation gradually moves from the outermost layer of the nanotube to its interior, resulting in the successive removal of graphene cylinders and thinner nanotubes (LOOS, 2014).

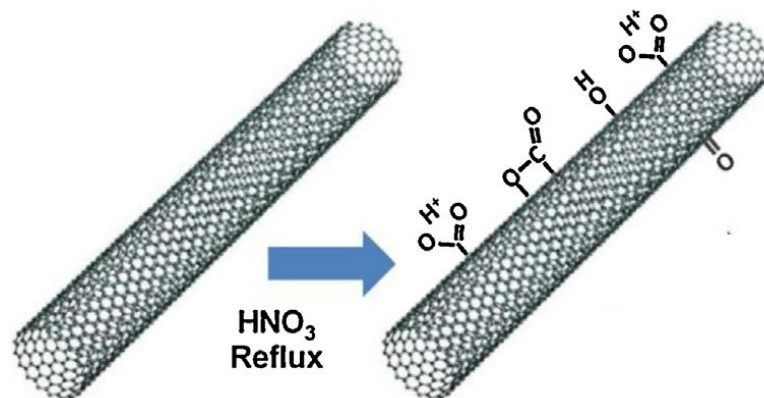


Figure 4.2 – Scheme of the oxidative treatment of CNTs with HNO_3 .

Source: Adapted from (ZUGIC; BELL; FLYTZANI-STEPHANOPOULOS, 2014)

Furthermore, a new distribution of defects is introduced on the surface of the nanotubes, which together with the functional groups, serve as a kind of anchorage for the active phase NPs to be impregnated, as well as for the adsorption of reactant molecules, increasing thus the catalytic activity (MELCHIONNA *et al.*, 2015). This good performance can be explained by the transfer of electrons from the active phase metal NPs to the CNTs, as reported in oxidation reactions of 1-phenylethanol with 5%Au/SWCNTs catalysts (SHANAHAN *et al.*, 2011). Also, its high thermal conductivity, which can reach double that of the diamond, contributes to the dissipation of the heat, preventing its sintering and the coke formation.

Although, in catalysis, the deposition of NPs on the CNT outer surface is preferred, there are studies on the increase of the reactant molecules adsorption when depositing NPs also on the CNT internal cavities. In this context, (TESSONNIER *et al.*, 2009) proposed a method for impregnating NPs inside and outside the nanotubes based on the differences between the interface energies of the organic and aqueous precursors solutions with the outer surface of the functionalized CNTs.

It is important to highlight that the use of CNTs as catalyst support, despite presenting good performance, is not yet an economically viable option for large-scale processes due to the high cost of their synthesis (MELCHIONNA *et al.*, 2015). Currently, the method of Chemical Vapor Deposition (CVD) produces the largest quantities of nanotubes at more affordable prices, but imperfections in the structure are common, which may negatively influence their catalytic activity. It is expected that in the next 5-10 years CNTs applications will increase, and demand will increase along

with the quality and the CNTs production rate, lowering thus their price and impacting the industry (LOOS, 2014).

4.2.3 Catalysts supported on CNTs for the WGS reaction

ZUGIC; BELL, and FLYTZANI-STEPHANOPOULOS (2014) conducted the WGS reaction at low temperatures using Pt catalysts supported on MWCNTs. The catalysts presented better performance in their activities with the addition of sodium ions (Na^+) in the structure, which functioned as promoters. During the preparation, the NTCMPs were oxidized by nitric acid (HNO_3) with the consequent increase of groups with oxygen (carboxylic, anhydride, among others) on the surface of the nanotubes. According to the authors, the presence of Na^+ ions modifies the ordering of these oxygenated groups in the MWCNTs and stabilizes the partial oxidation state of Pt in a conceivable structure of Pt-Na-OH_x , inferred through the X-ray photoelectron spectroscopy analysis. Thus, increasing the number of active sites, the consequent raise in the catalytic activity of the WGS reaction was observed. It was also concluded that the CNTs surface performance in carrying activated Pt sites promoted by Na^+ ions was not affected by the decrease of the oxygen content due to the calcination of the catalyst, performed at 800°C .

BELTRAM et al. (2015) used MWCNTs as support for the synthesis of palladium-ceria (Pd@CeO_2) catalysts in a shell-core structure. The integration of the carbonaceous supports improved the stability of the NPs by ordering the inorganic phase dispersion and increased the activity, suppressing the deactivation of the active phase which is commonly observed in conventional Pd@CeO_2 under reducing conditions. The post-synthetic removal of MWCNTs resulted in Pd@CeO_2 systems which, to a certain extent, retain the benefits introduced by the nanotubes, exhibiting moderate performances, although inferior to the analogs ones based on MWCNTs, with rapid deactivation at low temperature.

DONGIL et al. (2016) studied the WGS reaction at low temperatures using nickel (Ni) catalysts supported on ceria-promoted MWCNTs. Although many previous studies have employed CeO_2 as a support for metals, such as Pt, due to the strong stabilizing effect of this oxide on the metal, the authors decided to use CeO_2 as a promoter dispersed on a support of MWCNTs because of its high surface area and

low availability, promoting the reaction. Comparative studies with catalysts supported on activated carbon and HNO₃ oxidized MWCNTs (65%) were also performed.

It was observed that there are only three works with applications of carbon nanotubes as catalysts support for the WGS reaction. One realizes that the use of this prominent material in this important catalytic process for hydrogen production lacks deeper and more diversified studies, for example, with cheaper and traditionally industry-used active phase metals deposited on the surface of these nanotubes, which is one of the objectives of this work. Furthermore, the development of kinetic models for these types of catalysts was not yet reported in the WGS reaction literature.

4.3 Methodology

4.3.1 Catalyst synthesis

The synthesis of the 5wt%Co/7wt%Ce-3wt%Sr-MWCNT catalyst was performed following a methodology based on that of Figueira et al. (FIGUEIRA *et al.*, 2018). The commercial MWCNTs (acquired from Merck/Sigma-Aldrich) were used as the starting material (number: 412988, assay: > 7.5% MWCNT basis, composition: carbon content > 99% by TGA, outer diameter: 7-15 nm, length: 0.5-10 μm). The functionalization step was performed on 500 mg of nanotubes by adding 25 mL of a 1M nitric acid (HNO_3) solution for 16 h, while stirring at 500 rpm, at a temperature of 100°C (Figure 4.3). Hereby oxygenated groups are introduced on the surface of the carbon nanotubes and their tips are opened. Subsequently, they were cooled down to room temperature, filtered and washed with distilled water.

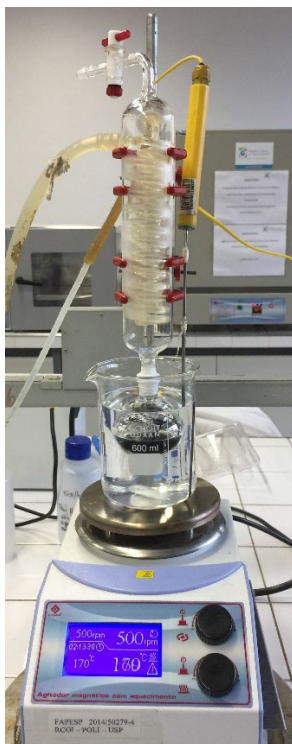


Figure 4.3 – Experimental apparatus for the functionalization of the MWCNTs.

The promoters, c.q. nanoparticles of Ce and Sr, were deposited on the MWCNT supports by wet impregnation with ethanolic solutions of the corresponding

amount of the precursors (purchased from Sigma-Aldrich): 130.2 mg of cerium III nitrate hexahydrate – $\text{Ce}(\text{NO}_3)_3 \cdot 6\text{H}_2\text{O}$ – and 43.5 mg of strontium nitrate – $\text{Sr}(\text{NO}_3)_2$, respectively. Both solutions were added dropwise to the functionalized MWCNTs, and then washed with distilled water. Figure 4.4 presents the MWCNTs being impregnated. After drying for 21 h at 50°C in a vacuum oven, the material was calcined with synthetic air (100 mL/min) for 2 h at 350°C , and then reduced with H_2 (100 mL/min) for 2 h at 400°C in a muffle furnace.

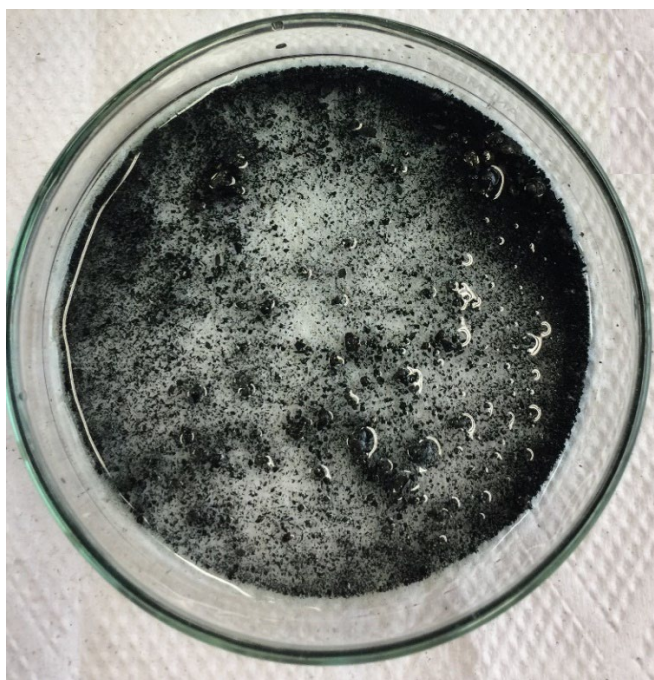


Figure 4.4 - MWCNTs being impregnated with the Cu-precursor solution aqueous solution.

Subsequently, the Co metallic active phase was deposited on the surface of the MWCNTs in a similar manner as the promoters. Firstly, 1.38 mL of ethylene glycol was added to fill the pores of the material, ensuring the deposition of Co nanoparticles on the external surface of the MWCNTs. Thereafter, an aqueous solution with 148.2 mg of cobalt (II) nitrate hexahydrate – $\text{Co}(\text{NO}_3)_2 \cdot 6\text{H}_2\text{O}$ (purchased from Sigma-Aldrich) was gradually added to the paste. The aforementioned steps of drying, calcination, and reduction were then repeated to obtain the Co/Ce-Sr-MWCNT catalyst.

4.3.2 Catalyst characterization

Several characterization techniques were performed to determine the properties, composition, and structure of the synthesized catalyst. An overview of these techniques, describing the equipment, the methodology, and the measured catalyst property are presented in this section.

4.3.2.1 Nitrogen Physisorption Isotherms

N₂ physisorption isotherms were acquired using a NOVA 1200e Surface Area & Pore Size Analyzer from Quantachrome Instruments located at the Institute of Chemistry (IQ) at Universidade de Sao Paulo (USP). 100 mg of the crude MWCNTs and the prepared catalyst were used for the analysis. The samples were first degassed under vacuum at 150°C for 17 h prior to N₂ adsorption at –196°C. The surface areas and pore volumes were determined following the BET (Brunauer, Emmet and Teller) and BJH (Barret, Jayner and Halenda) methods (BARRET; JOYNER; HALENDA, 1951; BRUNAUER; EMMETT; TELLER, 1938).

4.3.2.2 X-Ray Diffraction (XRD)

The powder method was employed with 80 mg of a catalyst sample in a Rigaku diffractometer (Miniflex model) with Cu K- α radiation ($\lambda = 1.54 \text{ \AA}$) located in the Catalysis Nucleus (NUCAT) of the Chemical Engineering Program/COPPE at Universidade Federal do Rio de Janeiro (UFRJ). The incidence angle (2θ) was varied between 10° and 90°, with a step size of 0.05° and an acquisition speed of 2° min⁻¹. The crystalline phases were identified by comparing the obtained diffractograms with the ICDD (International Center for Diffraction Data) data sheets using the MID JADE 5.0 software (MATERIALS DATA, 2017). Ultimately, the crystallite sizes were computed by applying the Scherrer Equation (PATTERSON, 1939):

$$d = \frac{0.89 \lambda}{\beta \cos \theta} \quad (6)$$

where λ is the X-ray radiation wavelength \AA , θ is the peak angle, and β is the width at half maximum (FWHM) of the respective XRD peak.

4.3.2.3 *Transmission Electron Microscopy (TEM) and Energy Dispersive X-Ray Spectroscopy (EDX)*

The images were obtained using an electronic transmission microscope JEOL JEM 2100 with 200 kV of acceleration voltage, 0.23 nm resolution at a point, and a maximum magnification of 1,500,000 times, located at the Sao Carlos' Institute of Chemistry (IQSC) at Universidade de Sao Paulo (USP). The samples (≈ 0.1 mg) were prepared dispersing the crude MWCNTs and the catalyst in toluene and sonicating them for a few minutes. Then, one drop of these suspensions was deposited on a 300-mesh copper-based grade (from Ted Pella Inc.). In addition, an Energy Dispersive X-Ray Spectroscopy (EDX) was performed with the characteristic X-rays emitted from the samples. The obtained spectrum was peaks related to the elements presented at the surface.

4.3.2.4 *Raman spectroscopy*

Raman spectroscopy method was used to characterize carbon structures and to evaluate the degree of graphitization, through the intensities of the characteristic D and G bands. The spectra of the samples – the crude MWCNTs and the prepared catalyst (≈ 5 mg) – were acquired using a Raman spectrometer HORIBA Jobin-Yvon LabRam HR800 UV, equipped with an Olympus microscope (BX41 model), a He-Ne laser ($\lambda = 633$ nm) lighting source, and a thermal conductivity detector ($T = -70^\circ\text{C}$). This analysis was performed in the Catalysis Nucleus (NUCAT) of the Chemical Engineering Program/COPPE at Universidade Federal do Rio de Janeiro (UFRJ). The spectra were collected from $100\text{-}1800\text{ cm}^{-1}$.

4.3.2.5 *Thermogravimetric Analysis (TGA)*

The thermograms were obtained using a HITACHI STA 7300 equipment located in the Catalysis Nucleus (NUCAT) of the Chemical Engineering Program/COPPE at Universidade Federal do Rio de Janeiro (UFRJ). About 2.5 mg of the synthesized catalyst was heated up at a rate of $10^\circ\text{C}/\text{min}$ from room temperature

to 1000°C under an inert atmosphere (N₂, 80 mL/min). The rate of mass loss was registered by a derivative thermogravimetric (DTG) curve with respect to time.

4.3.2.6 Hydrogen Temperature Programmed Reduction (H₂-TPR)

The analysis was performed with 200 mg of the synthesized catalyst in a Chemisorption Analyzer (Autochem II, from micromeritics®) with a U-shaped quartz reactor, located at the Laboratory for Chemical Technology (LCT) at Ghent University (Belgium). The sample was reduced under a flowing 5%H₂/Ar mixture (60 mL min⁻¹) from 50°C to 550°C (with a rate of 20°C/min), followed by passing He (60 mL min⁻¹) through the reactor for 30 min at 550°C. Hydrogen consumption was monitored by a thermal conductivity detector (TCD). Before the measurements, the sample was dried at 200°C (at a rate of 10°C/min) for 0.5 h with 60 mL min⁻¹ of He to eliminate moisture and adsorbed gases.

4.3.2.7 Pulsed CO chemisorption analysis

A pulsed CO chemisorption analysis was conducted in a Chemisorption Analyzer (Autochem II, from micromeritics®) equipped with a TCD to measure the CO consumption, located at the Laboratory for Chemical Technology (LCT) at Ghent University (Belgium). The sample (≈ 200 mg) was loaded into a U-shaped quartz reactor and was initially heated to 200°C (at a rate of 10°C/min) under He flow (60 mL min⁻¹) for 30 min, to eliminate possible residues. Afterwards, it was reduced under a flowing 5%H₂/Ar mixture (60 mL min⁻¹) from 50°C to 350°C (with a rate of 20°C/min) to activate the catalyst, followed by passing He through the reactor for 30 min at 350°C. Subsequently, the sample was purged with inert gas (60 mL min⁻¹ of He) for 1 h to remove the adsorbed H₂, and it was cooled down to room temperature (40°C). Then, every 3 min, CO pulses of 500 μL were fed to the system until the gas amount in the outlet was constant, i.e. the same peak areas were observed in the TCD responses. The amount of irreversibly adsorbed gas was calculated from the difference between saturation and the CO pulses introduced, and the active site density was calculated assuming a CO:Co stoichiometry of 1:1.

4.3.3 Catalyst activity tests

The catalytic activity tests were carried out in an automated Microactivity-Effi equipment (MAE18163 model) from PID ENG&TECH – a Micromeritics® company (Figure 4.5), located at the Laboratory for Research and Innovation in Catalytic Processes (LaPCat) of the Escola Politecnica (POLI) at Universidade de Sao Paulo (USP). The effluent was analyzed with an online gas chromatograph (Shimadzu GC-2010 Plus) equipped with a Carboxen-1010 PLOT column and a TCD detector. The reactor consisted of a Hastelloy X tube with an internal diameter of 9.1 mm and a total length of 304.8 mm, having a porous plate in the middle for loading the catalyst bed (made of Hastelloy C and 20 μm in size). A type-K thermocouple was used to measure the temperature inside the reactor tube by touching the catalyst bed, thereby ensuring a more accurate measurement and a better PID control for the isothermal operation of the reactor.

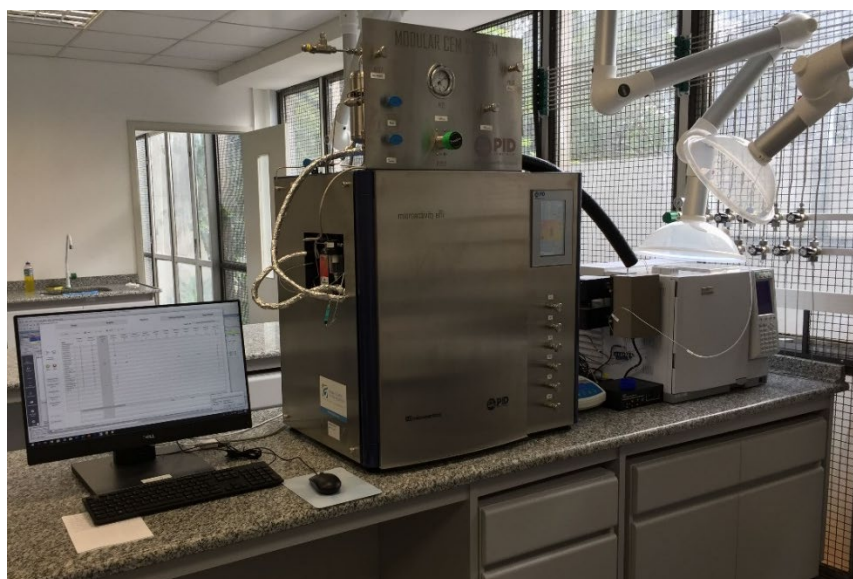


Figure 4.5 – Microactivity-EFFI coupled with GC.

For the catalytic tests of the WGS reaction over the Co/Ce-Sr-MWCNT catalyst, the feed was introduced into the system on a controlled manner by means of mass flow controllers for CO and N₂ (Bronkhorst) and a liquid flow meter (CORI-FLOW meter from Bronkhorst) for H₂O. The inert gas served as carrier to transport the liquid water droplets as aerosol, which were then heated and evaporated by a Controlled

Evaporator Mixer (CEM). The molar composition of the feed gas stream was 11% CO, 29% H₂O, and 60% N₂, with a total flow of 70 mL min⁻¹. The tests were performed using 0.100 g of catalyst, thus resulting in a gas hourly space velocity (GHSV) of 42,000 mL g_{cat}⁻¹ h⁻¹.

Prior to reaction, the catalyst was activated in-situ, by reduction with H₂ for 1 h at 300°C. The catalytic activity was then evaluated under atmospheric pressure at several temperatures in the range of 200-450°C, which encompasses the LT and HT processes. The reaction at each temperature was stabilized for 1 h to reach steady-state operation. Furthermore, additional tests were carried out varying the W_{cat}/F_{CO} ratio (space time) from 19 to 83 kg_{cat} s mol⁻¹ at three distinct temperatures: 300, 350, and 450°C. Finally, a 15-hour time-on-stream-test was also performed at 350°C to evaluate the catalyst deactivation at a CO conversion of 50%. This conversion level was selected to avoid an influence by the catalyst loading (ZHANG *et al.*, 2019). The catalytic activity was expressed by the degree of CO conversion and H₂ yield, respectively:

$$X_{CO} = \frac{F_{CO}^0 - F_{CO}}{F_{CO}^0} \times 100 \quad [\%] \quad (7)$$

$$Y_{H_2} = \frac{F_{H_2}}{F_{CO}^0} \times 100 \quad [\%] \quad (8)$$

Moreover, to calculate the chemical reaction equilibrium that limits the reactant conversion, the REquil pallet from ANSPEN PLUS® 8.0 was used with the Soave-Redlich-Kwong (SRK) Equation of State to consider the non-ideal behavior of the reaction medium.

4.3.4 Intrinsic kinetic measurements

The operating conditions, in which the kinetic data were acquired, were within the intrinsic kinetics regime. I.e. they were not disguised by mass and heat transfer limitations. This is critical to obtain reliable kinetic data (MARIN; YABLONSKY; CONSTALES, 2011). The corresponding criteria were used and satisfied using the worst-case scenario (i.e. at the highest temperature, lowest space velocity, and most

concentrated feed stream), which corresponds to 400°C, 0.025 mol s⁻¹ kg_{cat}⁻¹, 10% CO, 25.8% H₂O, 30.1% H₂, and 8.3% CO₂. The Carberry number used to assess the extent of external mass transfer between the gas phase and the catalyst surface was 8.8 x 10⁻⁵, which is 4 orders of magnitude lower than the maximum limit of 0.5 (CARBERRY, 1961). The internal diffusional effects were evaluated by the Weisz-Prater criterion. For an isothermal spherical catalyst particle, this parameter was equal to 4.3 x 10⁻⁴, well below the threshold value of 0.08, confirming the absence of concentration gradients inside the catalyst particles (FROMENT; BISCHOFF; WILDE, 2011). The absence of external and intraparticle heat transport limitations was also verified by the Mears criterion (MEARS, 1971). The corresponding temperature gradients amounted to 0.0384 K and 0.00052 K respectively, which are much lower than the corresponding limit of 5% deviation from the gradient of the observed reaction rate (1.75 K).

4.4 Results and discussion

The experimental assessment is composed of two main parts. The first one presents the characterization of the synthesized Co/Ce-Sr-MWCNT catalyst. The second part describes the catalytic testing of the WGS reaction, evaluating the CO conversion at different temperatures and space velocities.

4.4.1 Catalyst characterization

In this subsection, the results of the characterization of the Co/Ce-Sr-MWCNT catalyst are shown. The structure and composition aspects, relevant for understanding the catalytic behavior of this material, are highlighted in view of the catalytic tests described in section 4.3.2.

4.4.1.1 Nitrogen physisorption isotherms

The N₂ physisorption isotherms for the crude MWCNTs and the synthesized catalyst are presented in Figure 4.6. As can be observed, they exhibit a type IV adsorption curve with hysteresis, indicative of multilayer adsorption and capillary condensation in mesoporous materials (SCHMAL, 2016). However, the hysteresis loop ($p/p_0 > 0.7$), attributed to the nanotube cavities (DONGIL *et al.*, 2016), is not very broad for this specific type of MWCNTs acquired from Sigma-Aldrich (with > 7.5% MWCNT basis) compared to other carbon nanotubes with content of > 80% MWCNTs basis (DONGIL *et al.*, 2016; FIGUEIRA *et al.*, 2018). This can be explained by the existence of fewer cylindrical mesopores in the sample due to its lower content of MWCNTs (THOMMES *et al.*, 2015).

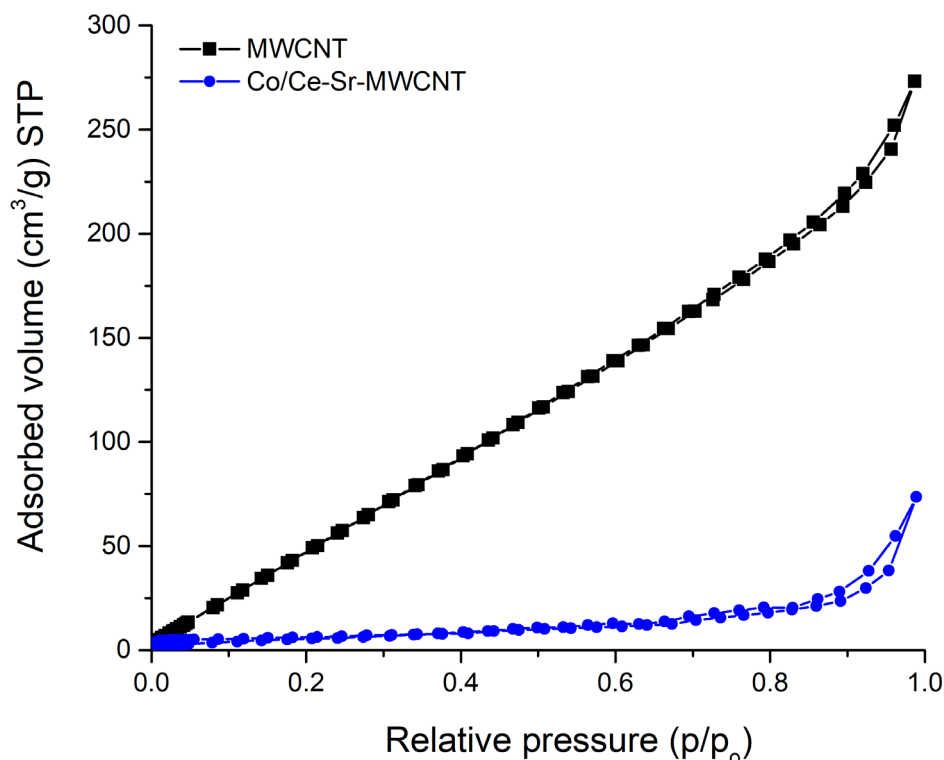


Figure 4.6 – N₂ physisorption isotherms at 77 K for the crude MWCNTs (black squares) and the synthesized catalyst of Co/Ce-Sr-MWCNT (blue circles)

As also evident from the isotherms, much lower amounts of nitrogen adsorb on the synthesized catalyst than on the raw MWCNTs, since the metal particles used for impregnation are agglomerated on the nanotubes surface (see also the XRD and TEM analysis in sections 4.4.1.2 and 4.4.1.3), thus blocking their tips, i.e., hindering the access to their pores. As can be seen in Table 4.1, this information can also be confirmed by the surface area and pore volume of the catalyst, S and V respectively, which are much smaller than those of the raw support. This is in agreement with what was reported in literature for MWCNT-supported catalysts (KOZONOE; BRITO; SCHMAL, 2020). Moreover, the pore diameters of the support and the catalyst are similar and in the range of mesoporous materials, $2 \text{ nm} < d < 50 \text{ nm}$ (SCHMAL, 2016), yet closer to the lower limit, thus, they can be considered as micro-mesoporous. Therefore, the majority of the particles impregnated on the MWCNTs must be mainly located at the outer surface, since the access to their interior cavities is obstructed.

Table 4.1 – Textural properties of the crude MWCNT and the Co/Ce-Sr-MWCNT catalyst as obtained from N₂ physisorption at 77 K

Sample	S _{BET} (m ² /g)	S _{BJH} (m ² /g)	V _{BJH} (cm ³ /g)	d _{BJH} (nm)
Crude MWCNT	267	218	0.40	3.2
Co/Ce-Sr-MWCNT	22	22	0.11	3.4

4.4.1.2 X-Ray Diffraction

Figure 4.7 shows the X-ray diffractograms for the synthesized catalyst. The characteristic peaks of MWCNTs at 26.2°, 43.1°, and 53.7° are apparent. At 77.7°, another characteristic peak with very low intensity was found by the MID JADE 5.0 software. These peaks can be attributed to the hkl graphite planes (002), (100), (004), and (110), respectively. This indicates that the graphitic structure of the MWCNTs was maintained after the different steps of catalyst synthesis. In addition, the higher peak intensity of the plane (002) in relation to (100) is an indication that these MWCNTs are made of concentric cylindrical graphene sheets with crystalline structure (PENG; LIU, 2006).

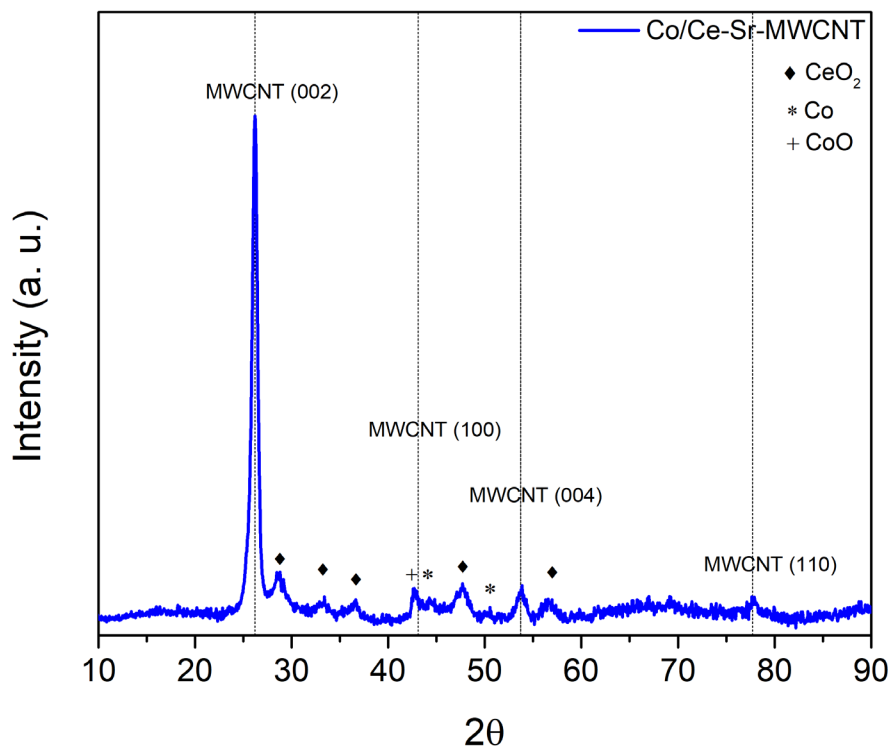


Figure 4.7 – X-ray diffractogram of the Co/Ce-Sr-MWCNT catalyst. The numbers between brackets correspond to the hkl planes of the MWCNT.

The peaks corresponding to the other components exhibit a lower intensity, since they are also present in a lower content in the material (< 10wt%), which sometimes makes them challenging to recognize, as is the case of Sr (3wt%). The peaks located at 44.2° and 51.5° correspond to the presence of metallic Co related to the crystallographic planes (111) and (200), respectively. In addition, the peak at 42.6° indicates the presence of cobalt oxide II, CoO, diffracted in the plane (200). The presence of Co⁰ in the diffractogram confirms that the reduction step in the synthesis method was properly performed. Moreover, Ceria (CeO₂) peaks were also identified at 28.6°, 32.9°, 36.6°, 48.1°, and 56.3°, which correspond to the planes (111), (200), (104), (214), and (311), respectively, of its face-centered cubic lattice structure.

By the application of the Scherrer equation, the crystallite sizes of the identified species were computed and are in the range of 3 to 7 nm (Table 4.2). In addition, since a particle is a cluster of agglomerated crystallites, the metallic nanoparticles are larger than 3-7 nm and, thus, they block the MWCNT ends (outer diameter: 7-15 nm), preventing their access to the internal pores of the nanotubes. This explains the reduction in the surface area after the impregnation of the metallic nanoparticles and

indicates that these nanoparticles are mainly located at the external surface of the carbon nanotubes.

Table 4.2 – Crystallite size of the compounds of the Co/Ce-Sr-MWCNT catalyst (calculated using the Scherrer equation)

Compound	Crystallite size (nm)
CeO ₂ (111)	3.8
CeO ₂ (200)	3.4
CeO ₂ (104)	3.2
CeO ₂ (214)	4.0
CeO ₂ (311)	4.0
CoO (200)	6.7
Co (111)	4.5
Co (200)	6.5

4.4.1.3 Transmission Electron Microscopy (TEM)

TEM images of the catalysts at different stages of the synthesis are shown in Figure 4.8. The first three images (a-c) show the crude MWCNTs. As can be observed, they are rather inflexible and rigid, unlike in other works that reported them as more malleable and softer (DONGIL *et al.*, 2016; FIGUEIRA *et al.*, 2018; KOZONOE *et al.*, 2019; KOZONOE; BRITO; SCHMAL, 2020). In addition, it is possible to observe some polygonal carbon nanoparticles around the nanotubes, as expected by the sample assay of > 7.5% MWCNT basis. Figure 4.8c illustrates the external (20 nm) and internal (3 nm) diameters of a nanotube, and allows determining the number of walls (about 30), by counting the number of parallel lines when moving away from the internal cavity of the nanotube. Figure 4.8d shows the functionalized MWCNTs with the tips opened. It can be observed that the crude MWCNTs have fragmented into smaller length tubes during the acid treatment (SERP; CORRIAS; KALCK, 2003).

Figure 4.8e and f depict the sample containing Ce and Sr particles deposited on the MWCNTs. As expected from the N₂ physisorption and XRD results, these large particles could not enter the inner cavities of the nanotubes because of their sizes. As

seen in Figure 4.8e, there is a cloud of particles covering the support, confirming that Ce and Sr were agglomerated, thus blocking the tips of the MWCNTs. In Figure 4.8f, it can be observed that these particles are mainly located on the external surface of the nanotubes. Very few of them were able to enter, filling the internal cavities, as shown in Figure 4.8g.

Furthermore, Figures 4.8h-l present the fully synthesized Co/Ce-Sr-MWCNT catalyst. It can be observed that the cobalt active phase particles and the promoter (Ce and Sr) particles were deposited on the external surface, wrapping around the nanotubes and building a metal-support interaction for the catalyst activity. Last but not least, the EDX spectrum taken from Figure 4.8i (shown in Figure 4.9) confirms the results from the XRD analysis, including the detection of Sr and the identification of copper and gold on the surface of the MWCNTs, which were the constituent compounds of the grid material.

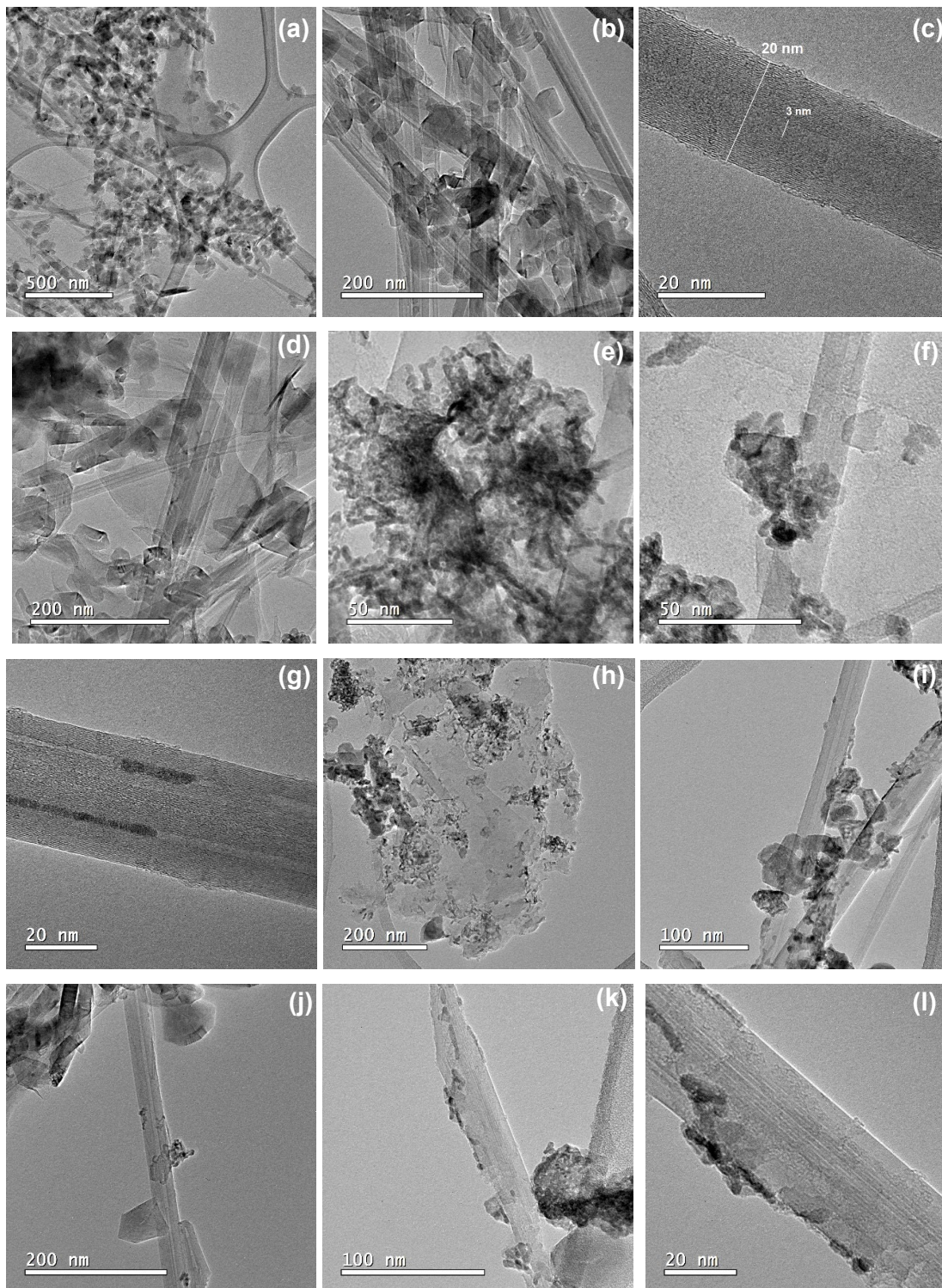


Figure 4.8 – TEM images of the catalysts during different steps of the preparation method: (a)-(c) crude MWCNTs, (d) functionalized MWCNTs, (e)-(g) Ce and Sr nanoparticles impregnated on the MWCNTs, and (h)-(l) Co, Ce, and Sr nanoparticles deposited on the MWCNTs.

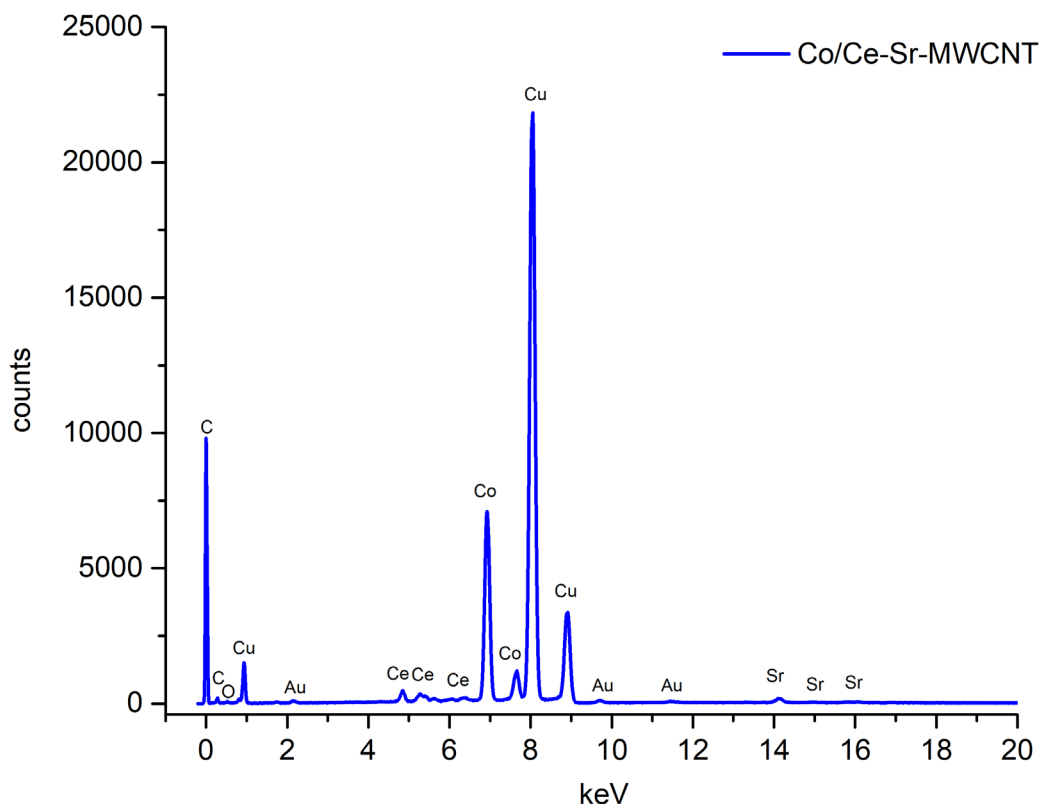


Figure 4.9 – EDX spectrum from Figure 3i of the Co/Ce-Sr-MWCNT catalyst

4.4.1.4 Raman spectroscopy

Figure 4.10 shows the Raman spectra for the crude MWCNTs and the synthesized catalyst. The characteristic D and G bands for the MWCNTs are presented at 1336 cm^{-1} and 1583 cm^{-1} , respectively. The former is related to the structural disorder of the carbonaceous material as a consequence of the presence of some amorphous carbon, sp^3 bonding defects, and curvatures of the nanotubes, while the latter is associated with high degree of order in sp^2 bonded carbon graphitic materials (OSSWALD; HAVEL; GOGOTSI, 2007).

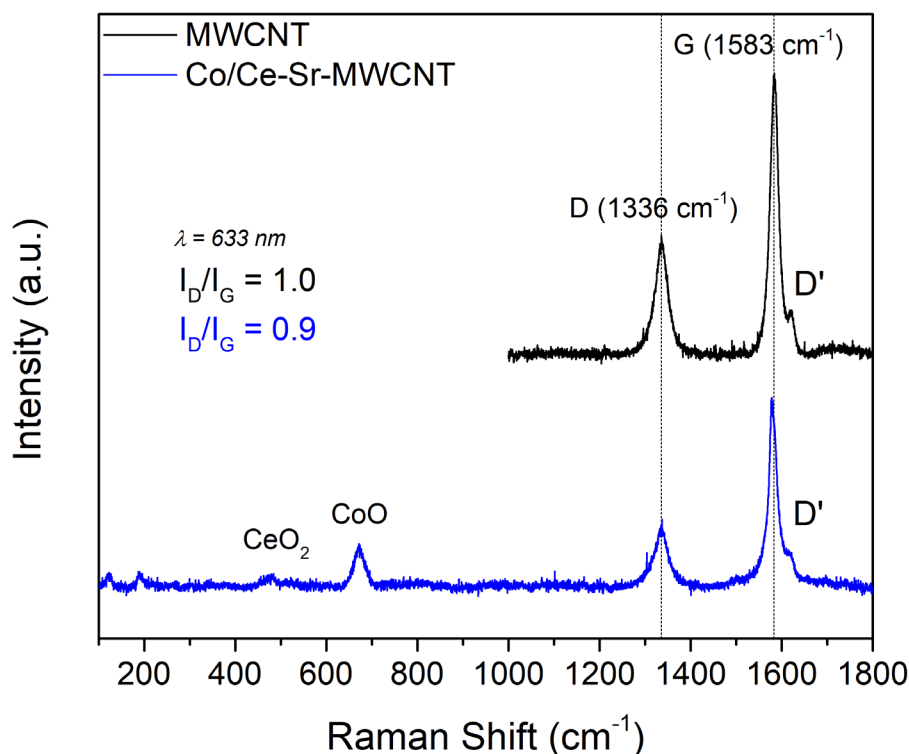


Figure 4.10 – Raman spectra of the raw MWCNT and the synthesized catalyst of Co/Ce-Sr-MWCNT

The graphitization degree, measured by the I_D/I_G area ratio, amounts to 1.0 for the raw MWCNTs and 0.9 for the Co/Ce-Sr-MWCNT catalyst. These low values, compared to the ratio of amorphous and defective MWCNTs (1.4 to 2.1) (OSSWALD; HAVEL; GOGOTSI, 2007), indicate that the acquired MWCNTs have a stronger graphitic character, as also evident from the TEM images, with inflexible and rigid nanotubes, and also presenting graphite polygonal nanoparticles. This high ordering can also be explained by the high number of walls presented in the MWCNTs. In addition, the D' band at 1619 cm^{-1} indicates the presence of intercalated graphite compounds (LEHMAN *et al.*, 2011).

Furthermore, the slight decrease of the I_D/I_G ratio and the peak intensities of the catalyst compared to the ones related to the raw support confirms that the impregnated species are wrapping around most of the carbon nanotube surface, as shown in the TEM images. This confirms that the deposition of Co, Sr, and Ce particles is predominantly on the external surface of the MWCNTs, in agreement with the characterization results discussed above. The bands of the interaction of the carbon nanotubes with other species in the catalyst are indicated at 675 cm^{-1} for CoO (LI *et*

al., 2016) and 456 cm^{-1} for CeO_2 (BELTRAM *et al.*, 2015), confirming the compounds identified by the XRD analysis.

4.4.1.5 Thermogravimetric Analysis (TGA)

Figure 4.11 illustrates the TGA and DTG results for the prepared Co/Ce-Sr-MWCNT catalyst. As observed, the catalyst begins to decompose at 632°C , when a large peak is observed in the DTG curve, and a pronounced slope is observed in the TGA thermogram. The peak at 690°C may be attributed to the formation of compounds with new crystalline structures, as Co-Ce alloys, or to the decomposition of the graphitic layers presented in the sample. Importantly, no significant weight loss was noticed in the temperature range of the WGS reaction ($200\text{--}450^\circ\text{C}$), confirming the graphitic character of the catalyst (LEHMAN *et al.*, 2011), as already reported in the previous characterization results. Thus, this material can withstand the operating conditions of the WGS without decomposing.

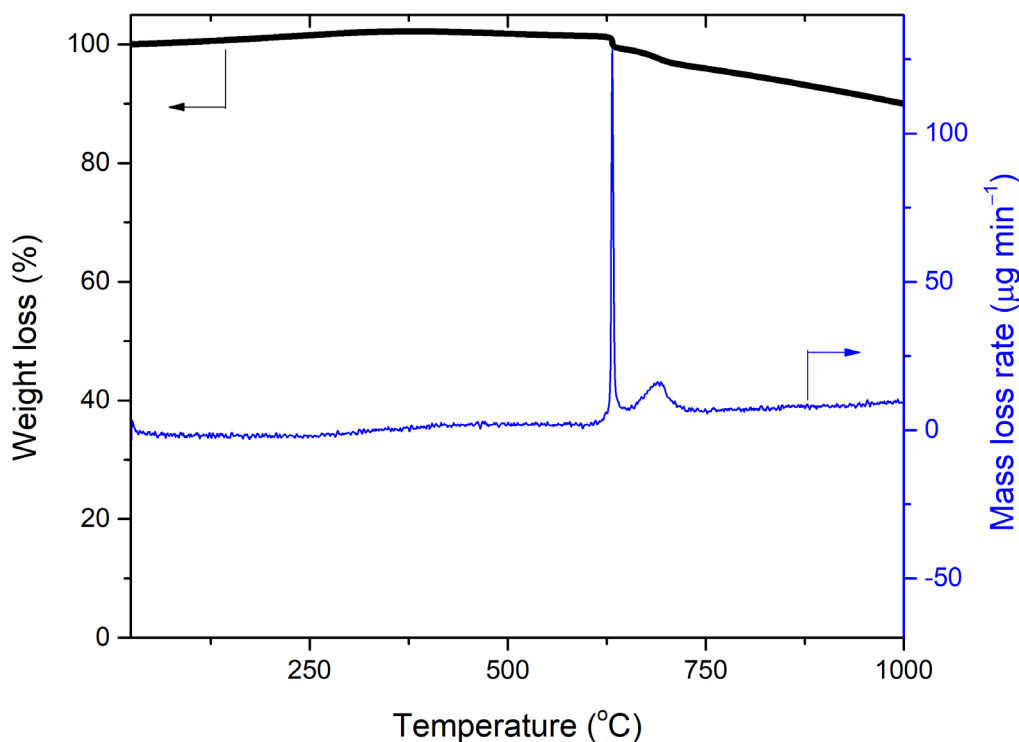


Figure 4.11 – TGA (black) and DTG (blue) curves of the catalyst of Co/Ce-Sr-MWCNT under N_2 atmosphere.

The thermal resistance of the MWCNTs is directly related to the extended π -conjugated bonds present in their structure, but it is also affected by the presence of the impregnated metallic nanoparticles of the catalyst, the existence of polygonal graphite nanoparticles, the number of walls of the nanotubes, the amount of defects on the MWCNT surface, etc. (LEHMAN *et al.*, 2011). In addition, the low number of peaks on the DTG curve indicates a high degree of purity of the material under study.

4.4.1.6 Hydrogen Temperature Programmed Reduction (H_2 -TPR)

Figure 4.12 shows the reduction profile as a function of temperature for the Co/Ce-Sr-MWCNT catalyst. The observed peaks at 255°C and 380°C correspond to the first reduction stages of $Co_3O_4 \rightarrow Co_{1-x}O \rightarrow CoO$, respectively (OLIVEIRA; FRANCESCHINI; PASSOS, 2014), showing the different reducible cobalt oxide species.

While the highest peak at 489°C is attributed to the full reduction to Co^0 . This temperature of 489°C is lower than the one reported in the literature, 591°C, for obtaining cobalt in the metallic state from the pure Co_3O_4 (RABEE *et al.*, 2022). This shift to lower temperatures demonstrates the pronounced interaction between these cobalt species with the promoter ceria, resulting in an easier reducibility (BUIRAGO *et al.*, 2012).

Furthermore, the peak at 536°C corresponds to the reduction of small crystallites of ceria with less interaction with the active phase (BUIRAGO *et al.*, 2012), leading to CeO_x phase formation (DAMYANOVA *et al.*, 2002).

As observed in the XRD results, the catalyst already consists of mostly of Co^0 nanoparticles, which are known to be the active sites for the WGS reaction (DE LA OSA *et al.*, 2011).

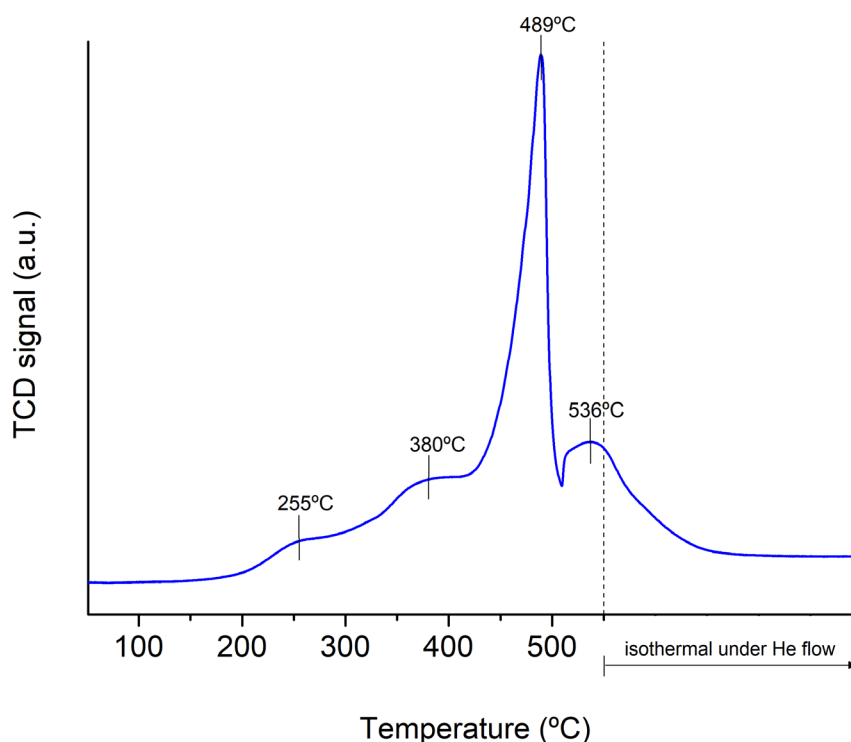


Figure 4.12 – H₂-TPR profile for the Co/Ce-Sr-MWCNT catalyst.

4.4.1.7 Pulsed CO chemisorption analysis

The CO chemisorption peaks in the effluent are visualized in Figure 4.13, showing the amount that was not chemically adsorbed. As can be noted, with the increase in the number of pulses, the gas is no longer chemisorbed, and therefore, the peak intensity reaches a plateau. The amount of irreversibly adsorbed gas is determined as the difference between saturation, i.e. the catalyst surface is fully covered by the gas, and the CO pulses that precede this equilibrium stage. The active site density has been calculated from these amounts, knowing the cobalt concentration in the catalyst (5 wt%) and assuming a chemisorption stoichiometry of CO:cobalt = 1:1. The most relevant parameters obtained from this analysis are shown in Table 4.3. The active site density ($0.012 \text{ mol}_{\text{Act.Surf.}}/\text{kg}_{\text{cat}}$) is of the same order of magnitude as that found by Mitchell *et al.* (2020) for a similar catalyst of Pt₃Co/MWCNT ($0.019 \text{ mol}_{\text{Act.Surf.}}/\text{kg}_{\text{cat}}$) (MITCHELL *et al.*, 2020). These findings show that CO is interacting with the interface Co-MWCNT because of the synergy of the support with the active phase.

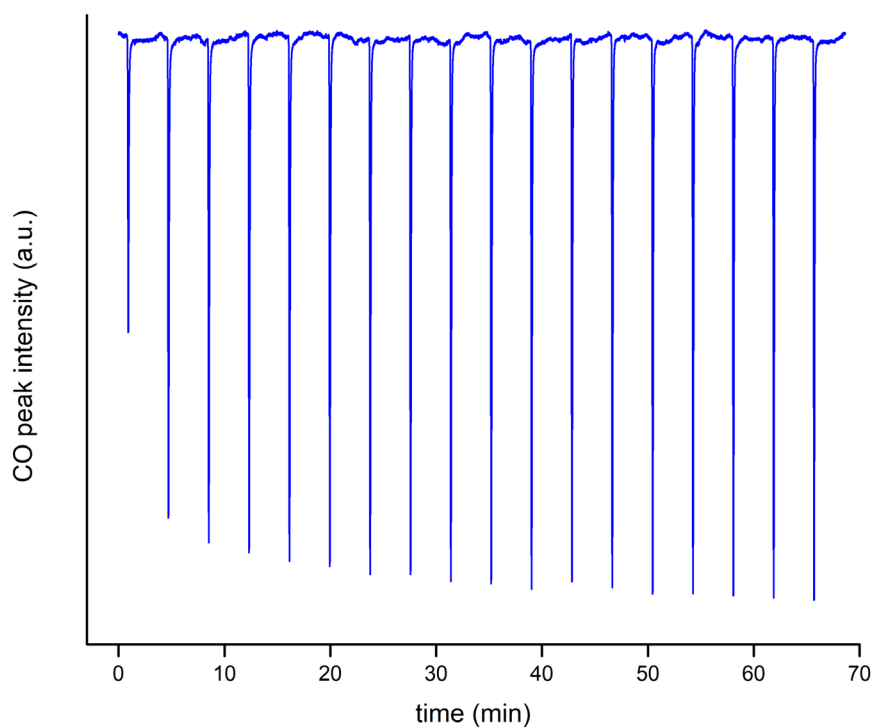


Figure 4.13 – Signal produced by successive injections of equal volumes of CO onto the catalyst of Co/Ce-Sr-MWCNT.

Table 4.3 – Properties obtained from the CO pulsed chemisorption analysis.

Property	Values
Volume of CO chemisorbed	0.257 cm ³ /g _{cat}
Metallic surface area	9.2 m ² /g _{metal}
Active site density	0.012 mol _{Act.Surf.} /kg _{cat}

4.4.2 Catalytic tests

Figure 4.14 shows the catalytic activity of the Co/Ce-Sr-MWCNT catalyst for the WGS reaction in terms of CO conversion as a function of the temperature in the range from 200 to 450°C. Firstly, the activation temperature was 400°C (empty points in the graph) based on the TPR results, with all cobalt particles in their metallic form. It

can be observed that the CO conversion increases with the temperature in agreement with the Arrhenius law. The catalyst presented activity for the high-temperature WGS process (300-450°C) (SAEIDI *et al.*, 2017), reaching CO conversions higher than 80%. It is also noteworthy that the H₂ yield stoichiometrically agreed with the CO conversions, assuring a closed molar balance for the system (Figure 4.15).

The performance curve for the activation temperature of 300°C is shown with filled points in Figure 4.14. At this condition, the CoO particles are reduced during the progress of the experiment with the H₂ produced by the reaction. It can be seen that CO conversion was a little bit lower than a previous run with catalyst activation at 400°C for temperatures below 350°C (before *in-situ* reduction), and a little bit higher for temperatures above 375°C (after *in-situ* reduction), reaching near-equilibrium conversions (~ 90%). The novel active sites of Co⁰ formed after the *in-situ* reduction (T > 380°C) were, thus, readily available for the WGS reaction, boosting the catalyst activity. Therefore, in the following, all catalytic tests were carried out with the activation temperature of 300°C.

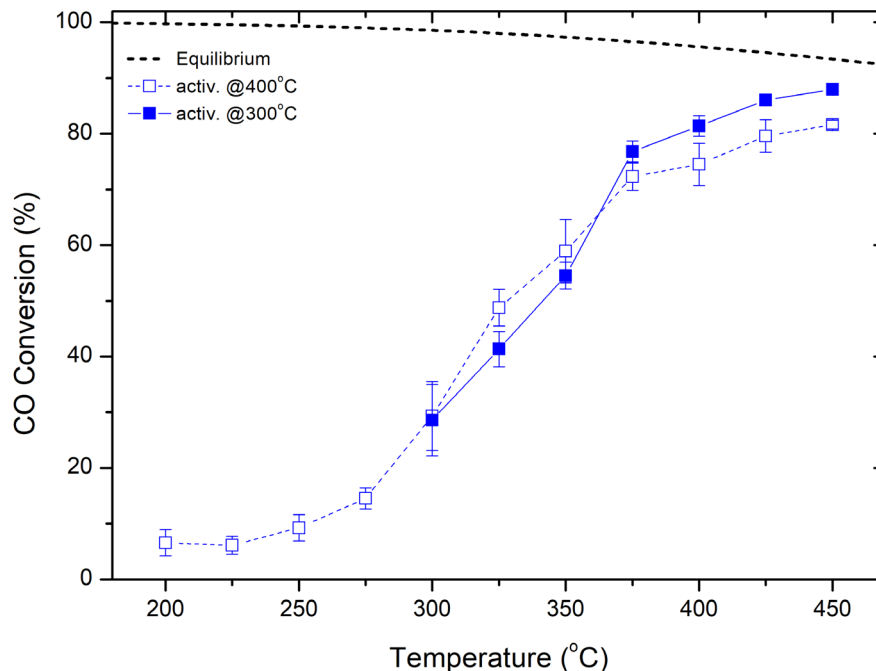


Figure 4.14 – CO conversion as a function of temperature for the WGS reaction over the Co/Ce-Sr-MWCNT catalyst with space time ($W/F_{CO,inlet}$) of 62.5 kg s mol⁻¹ for 2 different pretreatment temperatures (empty points at 400°C and filled points at 300°C). The dashed line represents the equilibrium conversions for the feed composition of the experiment: 11% CO, 29% H₂O, and 60% N₂ under atmospheric pressure (calculated using the REquil pallet from ASPEN PLUS® 8.0). Lines connecting the experimental points were added to guide the eye.

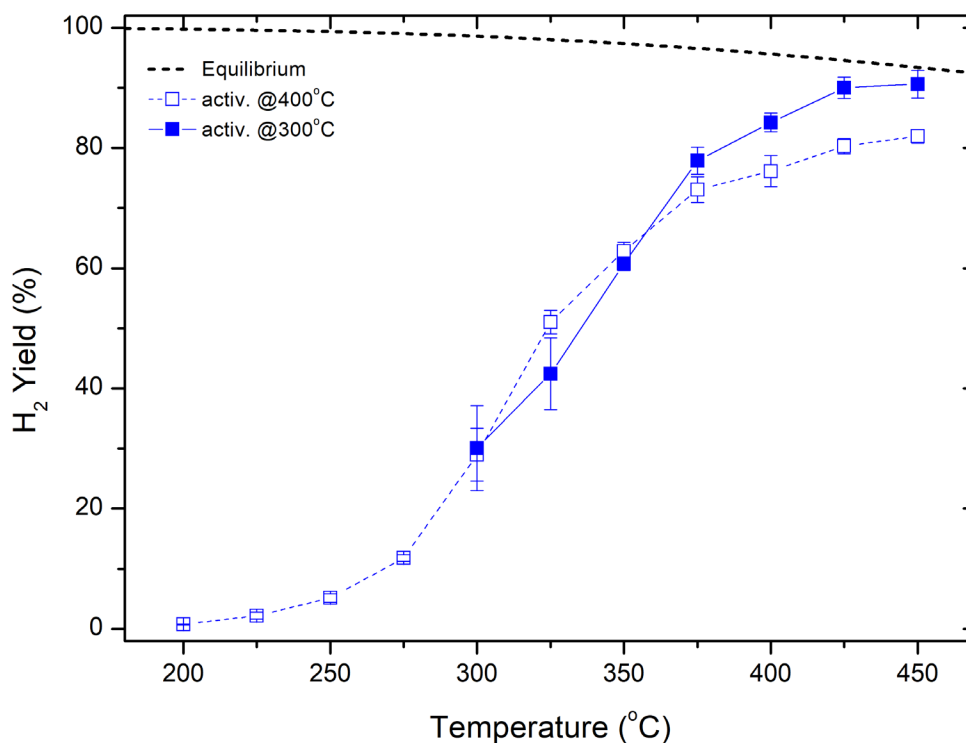


Figure 4.15 – H₂ yield as a function of temperature for the WGS reaction over the Co/Ce-Sr-MWCNT catalyst with space time ($W/F_{CO,inlet}$) of $62.5 \text{ kg s mol}^{-1}$ for 2 different pretreatment temperatures (empty points at 400°C and filled points at 300°C). The dashed line represents the equilibrium conversions for the feed composition of the experiment: 11% CO, 29% H₂O, and 60% N₂ under atmospheric pressure. (calculated using the REquil pallet from ASPEN PLUS® 8.0). Lines connecting the experimental points were added to guide the eye.

Figure 4.16 presents the CO conversion as a function of the space time, $W/F_{CO,inlet}$, for the catalytic tests performed at 300°, 350° and 400°C. It can be observed that the CO conversion increases with space time as expected. The increase in CO conversion with the space time is more pronounced at higher temperatures. Hence, the optimal WGS conditions are a temperature between 350 and 450°C and a space time between 70 and 80 kg s mol^{-1} . The CO conversion then approaches the equilibrium conversion. In addition, it can be seen that some points slightly deviate from the observed behavior (points outside the connecting dashed line), which could have happened due to some deactivation of the catalyst, possibly due to metal particle size growth (WANG; GORTE; WAGNER, 2002).

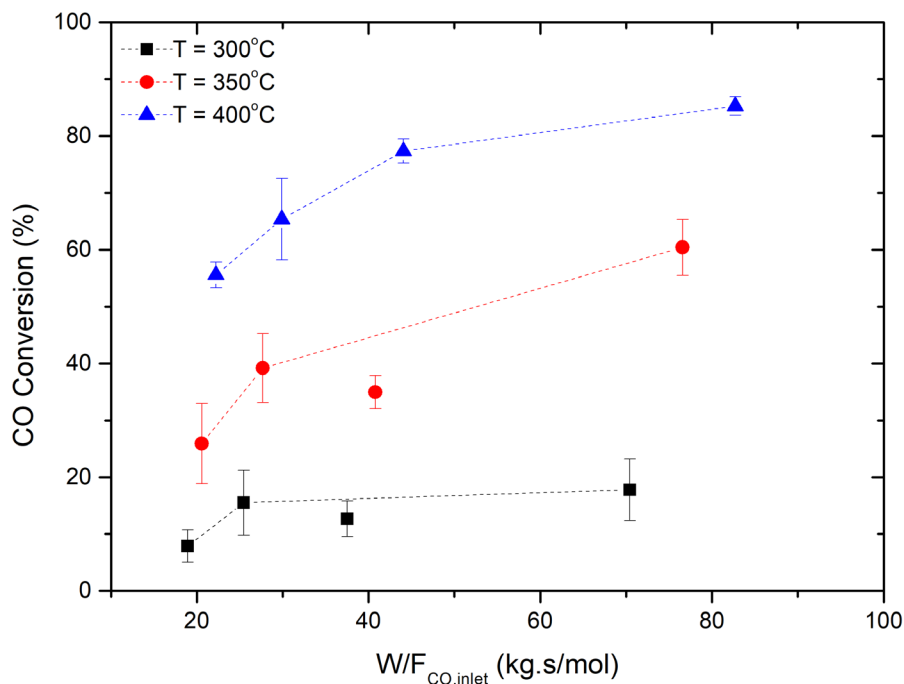


Figure 4.16 – CO conversion as a function of space time ($W/F_{CO,inlet}$) for the WGS reaction over the Co/Ce-Sr-MWCNT catalyst at three different temperatures: 300° (■), 350° (●) and 400°C (▲). The reaction was conducted with a feed composition of 11% CO, 29% H₂O, and 60% N₂, and under atmospheric pressure. Lines are added to guide the eye.

A 15-hour time-on-stream-test was carried out at 350°C, at conditions resulting in 50% CO conversion (Figure 4.17). The catalyst activity remained within 90% of its initial performance, which could be something expected for Pt and Pd ceria-supported catalysts (WANG; GORTE; WAGNER, 2002), thus demonstrating stability of the MWCNTs during this time period investigated. Studies of deactivation for the WGS reaction were also conducted for a platinum catalyst promoted by ceria supported on activated carbon, showing no considerable deactivation after 120h (BUIRAGO *et al.*, 2012).

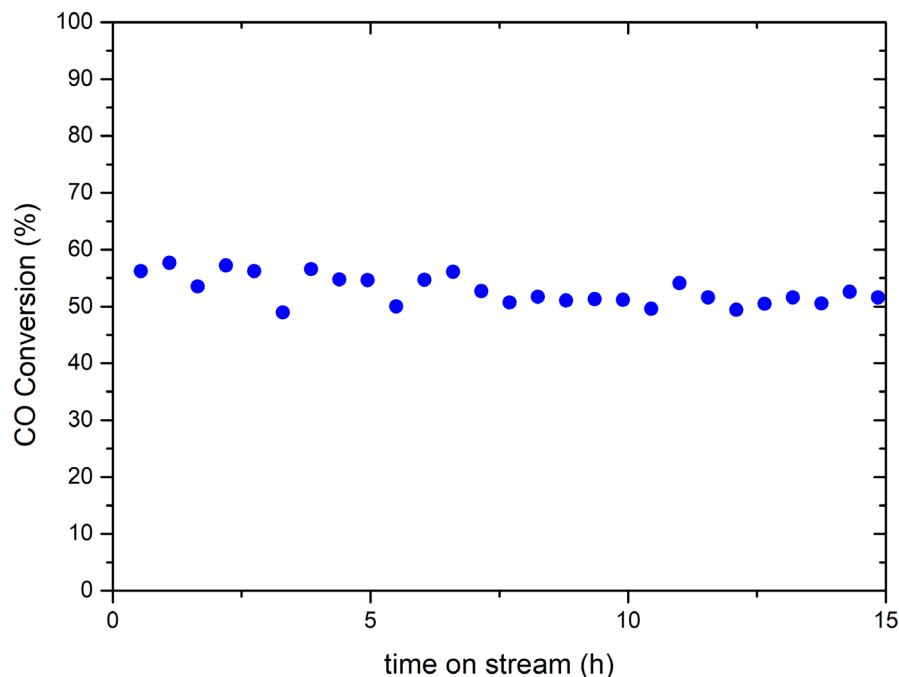


Figure 4.17 – 15-hour stability test for the WGS reaction over the Co/Ce-Sr-MWCNT catalyst at 350°C and a space time ($W/F_{\text{CO,inlet}}$) of $62.5 \text{ kg s mol}^{-1}$, a feed composition of 11% CO, 29% H₂O, and 60% N₂, and under atmospheric pressure.

4.5 Conclusions

All of these results show the high CO conversion obtained during the HT-WGS over the developed Co/Ce-Sr-MWCNT catalyst. This is the *first time* that the use of a non-noble catalyst supported on MWCNTs is successfully demonstrated for the HT-WGS. The interactions between cobalt and the functionalized carbon nanotubes (with *defects*) represents a charge transfer process (FIGUEIRA *et al.*, 2018) that stimulate the formation of active sites for the WGS reaction at 300-450°C. Strontium is responsible for enhancing this interaction as a donor species (FIGUEIRA *et al.*, 2018), and ceria promotes mobility of oxygen species on the surface as a result of the reduction of its cerium ions: $\text{Ce}^{+4} \leftrightarrow \text{Ce}^{3+}$ (DONGIL *et al.*, 2016). These characteristics enhance the electron movement in the catalyst structure, which is responsible for the adsorption of reactants, formation of intermediates, surface reactions, and the desorption of products.

5 CHAPTER III: (MACRO)KINETIC STUDY

5.1 Introduction

In order to optimize and fully understand the chemical reaction over the Co/Ce-Sr-MWCNT catalyst, and the consequent reactor design, kinetic models can be used to provide the most elegant way to quantify the reaction rate (DEVOCHT *et al.*, 2019). Two mechanisms are often considered in literature to explain the WGS reaction: the associative mechanism, in which adsorption-desorption reactions are considered with the formation of an intermediate, and the redox mechanism, in which oxidation and reduction cycles occur on the catalytic surface (DE QUEIROZ; DE MENEZES BARBOSA; DE ABREU, 2018; HOUSTON *et al.*, 2019).

Experimental evidence, through the use of mass spectroscopy, confirms that the HTS reaction follows the redox mechanism (ZHU; WACHS, 2016). On the other hand, many authors use both mechanisms to explain the LTS reaction. A fact to be highlighted is that there is no general consensus about the intermediary nature in the associative mechanism (SMITH R J; LOGANATHAN; SHANTHA, 2010).

The most well-known *macrokinetic* models in the literature for the WGS reaction process are of power laws and Langmuir-Hinshelwood (SMITH R J; LOGANATHAN; SHANTHA, 2010), with some derivations for the introduction of correction factors for porosity (ADAMS II; BARTON, 2009), the pressure (ZHAO; HU; LI, 1999), and the presence of impurities (NEWSOME, 1980).

In this kinetic study, the feed composition was varied in the range 11-18% (CO), 10-29% (H₂O), 0-38% (H₂), and 0-18% (CO₂). Conventional power-law and rate-determining step models have been adjusted to the WGS kinetic data obtained over numerous catalysts (SMITH R J; LOGANATHAN; SHANTHA, 2010). In this work, kinetic parameters have been estimated for the WGS over carbon-supported catalysts, to the best of our knowledge, for *the first time*, for different power-law and rate-determining step models. Next, model discrimination was performed in a pioneering effort to achieve quantitative information of the role of these materials in the WGS reaction.

5.2 Data for kinetic study

For the kinetic study of the WGS reaction over the Co/Ce-Sr-MWCNT catalyst, additional points were acquired varying also the feed composition: CO (11-18%), H₂O (10-29%), H₂ (0-38%), CO₂ (0-18%). These points were obtained according to a 2⁶⁻¹ fractional factorial design with a triplicate at the central point, which was selected to determine the experimental error. Co-feeding of the reaction products – H₂ and CO₂ – in some experiments aimed at capturing the effect of the equilibrium driving force, particularly in view of the model construction. In addition, extra points were acquired aiming at a more systematic variation of the operating conditions, thus totaling 60 data points for estimating the kinetic parameters.

Table 5.1 shows the experimental conditions for each run of the kinetic study of the WGS reaction over the Co/Ce-Sr-MWCNT catalyst (with variations in temperature, feed composition, and space velocity). The last column presents CO conversion for each input data.

Table 5.1 – Data acquired for the kinetic study of the WGS reaction over the Co/Ce-Sr-MWCNT under atmospheric pressure.

Run	T (°C)	y_{0CO} (%)	y_{0H_2O} (%)	y_{0H_2} (%)	y_{0CO_2} (%)	y_{0N_2} (%)	GHSV (mL g _{cat} ⁻¹ h ⁻¹)	X _{CO} (%)
1	300	12	12	0	0	76	20214	21.8
2	400	12	12	0	0	77	59034	55.2
3	300	17	11	0	0	72	59740	8.3
4	400	18	12	0	0	70	19908	55.2
5	300	12	23	0	0	65	58932	14.3
6	400	12	24	0	0	64	20010	91.9
7	300	17	23	0	0	60	21200	15.9
8	400	17	22	0	0	61	60064	53.4
9	300	11	11	35	0	44	58800	8.1
10	400	10	10	38	0	42	21000	72.1
11	300	15	10	38	0	37	21400	1.8
12	400	15	10	35	0	40	58930	25.2
13	300	10	20	37	0	33	21654	2.1
14	400	10	21	34	0	35	59256	49.5
15	300	15	20	34	0	31	59432	1.5
16	400	15	20	37	0	29	21304	70.2
17	300	11	11	0	18	59	71898	4.3
18	400	12	12	0	18	59	24174	79.6
19	300	17	11	0	18	54	25026	4.2
20	400	16	11	0	18	55	73216	45.5
21	300	11	23	0	18	48	26646	16.0
22	400	11	22	0	18	49	74562	73.4

Run	T (°C)	y_{0CO} (%)	y_{0H_2O} (%)	y_{0H_2} (%)	y_{0CO_2} (%)	y_{0N_2} (%)	GHSV (mL g _{cat} ⁻¹ h ⁻¹)	X _{CO} (%)
23	300	16	21	0	18	45	74240	4.2
24	400	17	22	0	18	44	25824	68.3
25	300	10	10	36	16	28	25842	4.5
26	400	10	10	34	17	30	70500	32.3
27	300	15	10	33	16	26	70360	-0.5
28	400	14	9	36	16	24	25732	25.8
29	300	10	19	33	16	22	71916	-0.2
30	400	10	20	35	16	19	25578	50.0
31	300	14	19	35	16	17	26568	4.4
32	400	15	19	33	16	17	72128	34.9
33	350	13	15	20	9	43	45404	8.2
34	350	13	15	20	9	43	45404	7.7
35	350	13	15	20	9	43	45404	5.9
36	300	11	11	0	0	77	60306	18.1
37	400	12	12	0	0	76	19722	87.1
38	300	18	12	0	0	70	19584	7.2
39	400	17	11	0	0	72	59792	60.6
40	300	12	23	0	0	65	19986	18.4
41	400	11	22	0	0	67	60534	87.0
42	300	16	22	0	0	62	59952	7.7
43	400	17	23	0	0	60	20624	87.5
44	300	11	29	0	0	60	25947	27.2
45	325	11	29	0	0	60	25947	42.1
46	350	11	29	0	0	60	25947	53.8
47	375	11	29	0	0	60	25947	76.7
48	400	11	29	0	0	60	25947	80.9
49	300	11	28	0	0	61	59304	15.0
50	350	11	28	0	0	61	59304	40.9
51	400	11	28	0	0	61	59304	66.8
52	300	12	29	0	0	59	20538	16.9
53	350	12	29	0	0	59	20538	60.5
54	400	12	29	0	0	59	20538	85.8
55	300	11	29	0	0	60	39354	13.0
56	350	11	29	0	0	60	39354	35.6
57	400	11	29	0	0	60	39354	78.0
58	300	11	28	0	0	61	80115	8.1
59	350	11	28	0	0	61	80115	27.8
60	400	11	28	0	0	61	80115	56.2

As can be observed in Table 5.1, generally, the higher the concentration of the reactants (CO and H₂O) for a fixed space velocity, the lower the CO conversion, with greater sensitivity to the variation of CO. This can be explained if the increase in

CO surface coverage leads to and is overcompensated by a decrease in water surface coverage due to their competition for active sites on the catalyst surface (THYBAUT; SAEYS; MARIN, 2002). Moreover, the inclusion of the WGS reaction products (H_2 and CO_2) in the feed caused the CO conversion to decrease drastically due to the activity of this catalyst also for the reverse water-gas shift (RWGS) reaction with the presence of its reactants. Thus, the importance of considering the equilibrium driving force in the reaction rate expressions in all kinetic models evaluated in this work.

In addition, Table 5.2 presents the same data acquired for the WGS kinetic study over the Co/Ce-Sr-MWCNT catalyst (Table 5.1), but in terms of input and output molar flow rates of the chemical species involved ($\mu\text{mol min}^{-1}$). This representation is in agreement with the ideal plug flow reactor model represented in Equation 3 (integral approach). Thus, these were the data used directly to estimate the several parameters of the rival kinetic models.

Table 5.2 – Data acquired in terms of molar flow rates for the kinetic study of the WGS reaction over the Co/Ce-Sr-MWCNT under atmospheric pressure.

Run	T (°C)	F_{0CO} ($\mu\text{mol min}^{-1}$)	F_{0H_2O} ($\mu\text{mol min}^{-1}$)	F_{0CO_2} ($\mu\text{mol min}^{-1}$)	F_{0H_2} ($\mu\text{mol min}^{-1}$)	F_{0N_2} ($\mu\text{mol min}^{-1}$)	F_{CO} ($\mu\text{mol min}^{-1}$)
1	300	86	86	0	0	544	67
2	400	207	207	0	0	1367	93
3	300	361	241	0	0	1515	331
4	400	106	71	0	0	423	48
5	300	240	481	0	0	1368	206
6	400	72	144	0	0	387	6
7	300	128	171	0	0	452	108
8	400	302	403	0	0	1107	141
9	300	225	225	721	0	913	207
10	400	66	66	238	0	264	18
11	300	113	75	287	0	282	111
12	400	271	181	618	0	708	203
13	300	78	157	281	0	252	77
14	400	186	372	611	0	619	94
15	300	319	425	718	0	645	314
16	400	94	126	238	0	185	28
17	300	285	285	0	463	1515	273
18	400	84	84	0	133	428	17
19	300	147	98	0	164	478	141
20	400	361	241	0	402	1205	197
21	300	107	214	0	167	456	90
22	400	244	487	0	407	1112	65
23	300	421	561	0	462	1187	403
24	400	129	172	0	137	341	41

Run	T (°C)	F_{0CO} ($\mu\text{mol min}^{-1}$)	F_{0H_2O} ($\mu\text{mol min}^{-1}$)	F_{0CO_2} ($\mu\text{mol min}^{-1}$)	F_{0H_2} ($\mu\text{mol min}^{-1}$)	F_{0N_2} ($\mu\text{mol min}^{-1}$)	F_{CO} ($\mu\text{mol min}^{-1}$)
25	300	89	89	330	147	260	85
26	400	212	212	714	357	632	144
27	300	369	246	831	409	639	371
28	400	110	73	281	125	187	82
29	300	248	497	836	418	549	249
30	400	76	152	272	122	149	38
31	300	133	177	328	146	157	127
32	400	316	421	717	354	368	206
33	350	189	227	300	130	634	174
34	350	189	227	300	130	634	175
35	350	189	227	300	130	634	178
36	300	244	244	0	0	1650	200
37	400	73	73	0	0	450	9
38	300	123	82	0	0	489	114
39	400	307	204	0	0	1293	121
40	300	82	165	0	0	461	67
41	400	203	406	0	0	1218	26
42	300	350	466	0	0	1309	323
43	400	107	142	0	0	374	13
44	300	105	262	0	0	553	76
45	325	100	251	0	0	530	58
46	350	96	241	0	0	508	45
47	375	93	232	0	0	489	22
48	400	89	223	0	0	471	17
49	300	236	589	0	0	1277	200
50	350	217	542	0	0	1175	128
51	400	201	502	0	0	1087	67
52	300	85	213	0	0	430	71
53	350	78	196	0	0	396	31
54	400	72	181	0	0	366	10
55	300	160	400	0	0	835	139
56	350	147	368	0	0	768	95
57	400	136	340	0	0	711	30
58	300	317	793	0	0	1730	291
59	350	292	729	0	0	1591	211
60	400	270	675	0	0	1473	118

5.3 Kinetic modeling and parameter estimation

The kinetic model for the WGS was constructed in an ideal plug flow reactor (PFR) with isothermal operation and negligible pressure drop, for which the mass balance of CO can be written as (SPRUNG *et al.*, 2015):

$$\frac{dF_{CO}}{dW} = R_{CO} \quad \text{with } F_{CO} = F_{CO,inlet} \text{ at } W_{cat} = 0 \quad (9)$$

As only the occurrence of the equimolar WGS reaction was taken into account, the net consumption rate for CO, R_{CO} , could be represented as the amount of CO consumed in that WGS reaction, with corresponding reaction rate, r_{WGS} :

$$R_{CO} = -r_{WGS} \quad (10)$$

In addition, as the WGS is described by a single reaction equation, the molar flow rates of the remaining species (H_2O , H_2 , and CO_2) can be calculated from the molar flow rate of CO, as follows:

$$F_{CO_2} = F_{CO_2,inlet} + F_{CO,inlet} - F_{CO} \quad (11)$$

$$F_{H_2O} = F_{H_2O,inlet} - F_{CO,inlet} + F_{CO} \quad (12)$$

$$F_{H_2} = F_{H_2,inlet} + F_{CO,inlet} - F_{CO} \quad (13)$$

The reactor equations were solved using the integration routine of the *odeint* function available in the SciPy library from Python (VIRTANEN *et al.*, 2020).

The reaction rate r_{WGS} was expressed by different kinetic model expressions based on power laws, associative and redox mechanisms with a rate-determining step, which are presented in Table 5.3. The associative mechanisms were represented by Langmuir-Hinshelwood-Hougen-Watson (LHHW) and Eley-Rideal approaches. In addition, the $(1 - \beta)$ term represents the reaction equilibrium driving force, with β expressed by Eq. (14) and the temperature dependence of the equilibrium coefficient indicated by Eq. (15) (SMITH R J; LOGANATHAN; SHANTHA, 2010).

$$\beta = \frac{p_{H_2} p_{CO_2}}{p_{CO} p_{H_2O}} \frac{1}{K_{eq}} \quad (14)$$

$$K_{eq} = \exp\left(\frac{4577.8}{T} - 4.33\right) \quad (15)$$

The rate coefficients, k , and the adsorption equilibrium coefficients for each species i , K_i , were described via the Arrhenius and van't Hoff equations in reparametrized form with the definition of a reference temperature, T_{ref} , equal to 350°C, as described in Eqs. (15) and (16), respectively (POISSONNIER *et al.*, 2018). Such an approach reduces the binary correlation between the pre-exponential factors and the

corresponding activation energy, E_a , or adsorption enthalpies, $\Delta H_{ads,i}$ (SCHWAAB; PINTO, 2007a).

$$k = k_{T_{ref}} \exp \left[-\frac{E_a}{R} \left(\frac{1}{T} - \frac{1}{T_{ref}} \right) \right] \quad (16)$$

$$K_i = K_{T_{ref},i} \exp \left[-\frac{\Delta H_{ads,i}}{R} \left(\frac{1}{T} - \frac{1}{T_{ref}} \right) \right] \quad (17)$$

Table 5.3 – Rival kinetic models considered for the WGS reaction rate conducted on the Co/Ce-Sr-MWCNT catalyst.

Kinetic model	Expression
<i>Simplified Power Law (M1)</i>	$r_{WGS} = k p_{CO} p_{H_2O} (1 - \beta)$
<i>Power Law (M2)</i>	$r_{WGS} = k p_{CO}^a p_{H_2O}^b (1 - \beta)$
<i>LHHW: dual-site surface reaction as RDS (M3)</i>	
$CO + * \rightleftharpoons CO^*$	
$H_2O + * \rightleftharpoons H_2O^*$	
$CO^* + H_2O^* \rightleftharpoons H_2^* + CO_2^*$	
(RDS)	
$H_2^* \rightleftharpoons H_2 + *$	
$CO_2^* \rightleftharpoons CO_2 + *$	
	$r_{WGS} = \frac{k p_{CO} p_{H_2O} (1 - \beta)}{(1 + K_{CO} p_{CO} + K_{H_2O} p_{H_2O} + K_{H_2} p_{H_2} + K_{CO_2} p_{CO_2})^2}$
<i>Eley-Rideal: single-site surface reaction as RDS (M4)</i>	
$CO + * \rightleftharpoons CO^*$	
$CO^* + H_2O \rightleftharpoons H_2 + CO_2^*$ (RDS)	
$CO_2^* \rightleftharpoons CO_2 + *$	
	$r_{WGS} = \frac{k p_{CO} p_{H_2O} (1 - \beta)}{1 + K_{CO} p_{CO} + K_{CO_2} p_{CO_2}}$
<i>Redox: CO oxidation as RDS (M5)</i>	
$H_2O + * \rightleftharpoons O^* + H_2$	
$CO + O^* \rightleftharpoons * + CO_2$ (RDS)	
	$r_{WGS} = \frac{k \frac{p_{CO} p_{H_2O}}{p_{H_2}} (1 - \beta)}{1 + \frac{K_{H_2O} p_{H_2O}}{p_{H_2}}}$

The kinetic parameters were estimated *via* the Maximum Likelihood Method, assuming that the error on the measurements is normally distributed, without correlation, and the independent variables are not subject to error (SCHWAAB; PINTO, 2007b). Hence, nonlinear regression was performed by minimizing the objective function of the weighted least squares between the experimental and calculated outlet flow rates of the response F_{CO} , as in Eq. (18). In this case, the weights were the inverse of the experimental errors for the response variables, σ_j (POISSONNIER *et al.*, 2018).

$$\sum_{i=1}^{NE} \sum_{j=1}^{NY} \left(\frac{F_{ij}^{exp} - F_{ij}^{calc}}{\sigma_j} \right)^2 \xrightarrow{k_{Tref}, K_{Tref,i}, E_a, \Delta H_{ads,i}} Min \quad (18)$$

A hybrid strategy was used to reach the optimal parameters. First, the Particle Swarm Optimization (PSO) algorithm (KENNEDY; EBERHART, 1995), available in the *pyswarm* package from Python, was applied. The selection of a heuristic method as a first stage was to overcome the potential numerical challenges related to the nonlinearity of the objective function and to obtain a set of initial estimates with a high probability for converging to the global minimum in the second step (PARK; FROMENT, 1998; SCHWAAB *et al.*, 2008). In this stage, the sum of squares of the residuals is further minimized using the Levenberg-Marquardt algorithm (MARQUARDT, 1963), available in the *curve_fit* function from SciPy, which exhibits a very fast convergence provided that the initial guesses are good (CONSTALES *et al.*, 2017).

5.4 Model discrimination

In this section, the construction of kinetic models for this active WGS catalyst, together with the estimation of the kinetic parameters, is discussed, followed by the discrimination of the best model. The rival kinetic models considered in Table 5.3 were adjusted to the experimental data of the molar flow rates of CO, as shown in Table 5.2. The use of one response variable is enough to represent this single reaction, hence the rank of the stoichiometric matrix is 1. The statistical significance of the individual parameter estimates had a greater importance in the final decision more than the accuracy of the model, as the estimation of reliable parameters is critical to represent the catalytic reaction phenomenon with confidence. The metrics to evaluate the regression performance for each kinetic model are presented in Table 5.4, such as the multiple correlation coefficient (R^2), the residual sum of squares (SSQ), the root-mean-squared deviation (RMSD) and the calculated and tabulated values from the F -test (F_{calc} and F_{tab}).

The discrimination procedure was based on the choice of the best model to describe the data with the lowest root mean square deviation (RMSD) and that have statistically significant parameters. In this way, the statistical meaning of the parameters was assessed using the individual 95% confidence interval (computed from a t -test with $NE.NY - NP$ degrees of freedom), which should not include zero. The global significance of the regression was verified with a F -test to evaluate if the model is better than simply averaging, i.e., if the regression sum of squares significantly overtakes the residual sum of squares divided by the corresponding degrees of freedom (TOCH; THYBAUT; MARIN, 2014). Furthermore, visual tools, such as parity plots and performance curves were also generated to assist in the determination of the statistical significance, and in the assessment of the physico-chemical meaning of the parameter estimates, respectively (TOCH, 2015).

Table 5.4 – Metrics to evaluate the regression performance for each kinetic model.

	M1	M2	M3	M4	M5
R²	0.9607	0.9681	0.9854	0.9616	0.9833
Residual SSQ ($\mu\text{mol min}^{-1}$)²	$2.3 \cdot 10^4$	$1.8 \cdot 10^4$	$8.4 \cdot 10^4$	$2.2 \cdot 10^4$	$9.6 \cdot 10^3$
RMSD $\mu\text{mol min}^{-1}$	19	17	12	19	13
F_{calc} > F_{tab} ?	$1 \times 10^3 > 4$	$6 \times 10^2 > 3$	$4 \times 10^2 > 2$	$3 \times 10^2 > 2$	$1 \times 10^3 > 3$

The simplified power-law model (M1) is the simplest model among all considered. This expression represents a direct proportionality between the reaction rate and the reactant partial pressures. The regression metrics obtained can already be considered accurate to describe the WGS kinetics, with an R² of 0.9607 and a RMSD of 19 $\mu\text{mol min}^{-1}$. Moreover, the two estimated parameters (Table 5.5) are statistically significant, i.e., their 95%-confidence intervals computed do not include zero (SCHWAAB; PINTO, 2007b). The activation energy of 101 kJ mol^{-1} is in agreement with those reported by Hutchings et al. (1992) with Co:Cr and Co:Mn catalysts (89-168 kJ mol^{-1}) (HUTCHINGS *et al.*, 1992). The parity plot and performance curves, shown in Figure 5.1, confirm these findings.

Table 5.5 – Estimated kinetic parameters for the WGS reaction over the Co/Ce-Sr-MWCNT catalyst of the model represented by the simplified power law model (M1).

Parameter	Value
$k_{T_{ref}}$	$(3.1 \pm 0.7) \times 10^4 \mu\text{mol g}^{-1}\text{atm}^{-2}\text{min}^{-1}$
E_a	$101 \pm 18 \text{ kJ/mol}$

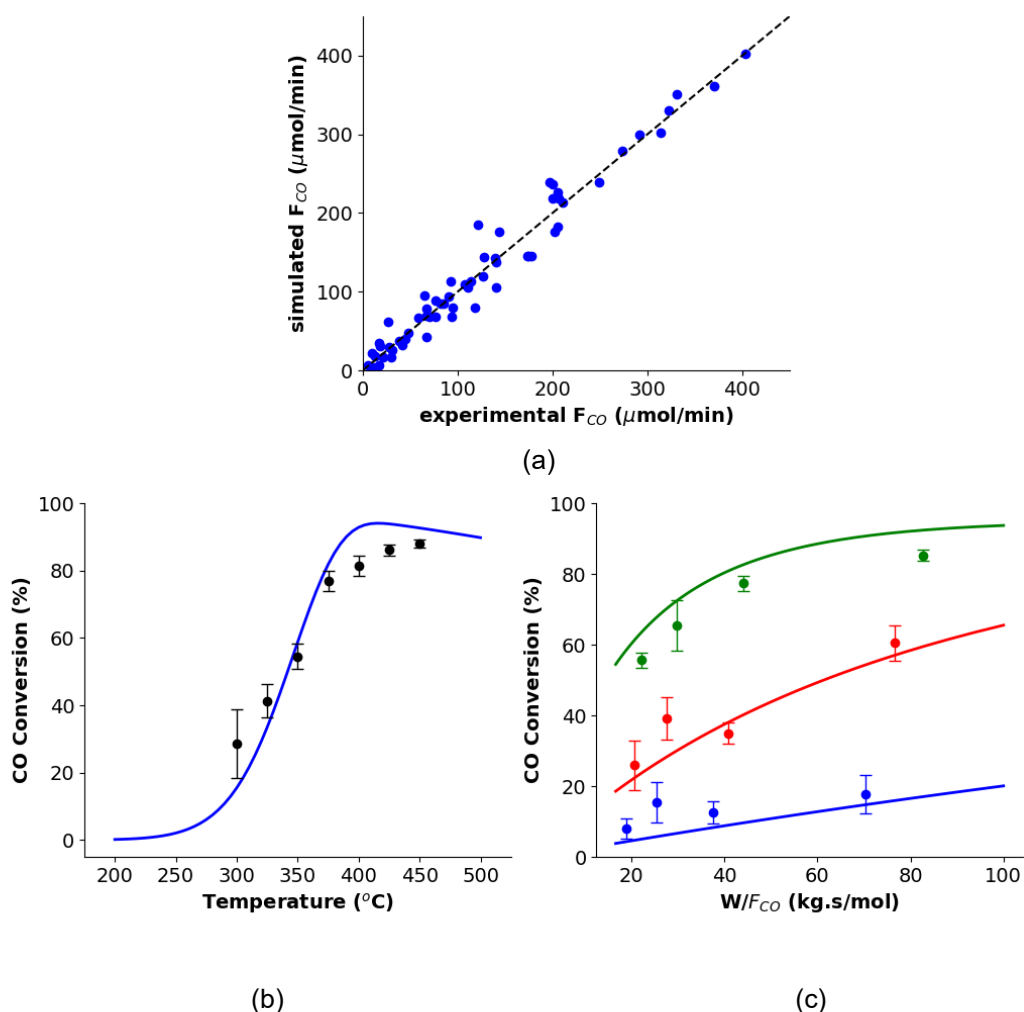


Figure 5.1 – (a) Parity plot of molar flow rates of CO. Performance curves of CO conversion as a function (b) of temperature and (c) of space time, for the WGS reaction over the Co/Ce-Sr-MWCNT catalyst using model M1.

The power-law model (M2) is an elaborated version of M1, by considering the reaction orders of CO and H₂O (4 parameters in total). Nevertheless, M2 is also an empirical model, without a reaction mechanism behind it. The regression quality is similar to that of M1. All parameters are statistically significant, see Table 5.6, and the parity plot and performance curves, see Figure 5.2, show the good agreement of the model simulated flow rates with the experimental ones. The reaction orders of CO and H₂O, 0.51 and 0.21, respectively, are close to the ones reported in Hal et al. (2011) (HLA *et al.*, 2011b) for a commercial sulfide Co/Mo catalysts, 0.52 and 0.21. Evidently, they differ from values obtained for different more noble metals as active phase, such as Fe:Cr, Cu, Ru, Ni, Rh, Pt, and Pd (SMITH R J; LOGANATHAN; SHANTHA, 2010). The activation energy estimated of 83 kJ/mol was also similar to the work from de la

Osa et al. (2011), which studied the kinetics of a commercial CoMo catalyst and obtained an activation energy of 85 kJ mol^{-1} (DE LA OSA *et al.*, 2011). These results are attributed to cobalt being the common denominator in these catalytic systems.

Table 5.6 – Estimated kinetic parameters for the WGS reaction over the Co/Ce-Sr-MWCNT catalyst of the model represented by power-law (M2).

Parameter	Value
$k_{T_{ref}}$	$(2.6 \pm 0.6) \times 10^3 \text{ } \mu\text{mol g}^{-1}\text{atm}^{-0.66}\text{min}^{-1}$
E_a	$83 \pm 14 \text{ kJ/mol}$
a	0.51 ± 0.19
b	0.21 ± 0.16

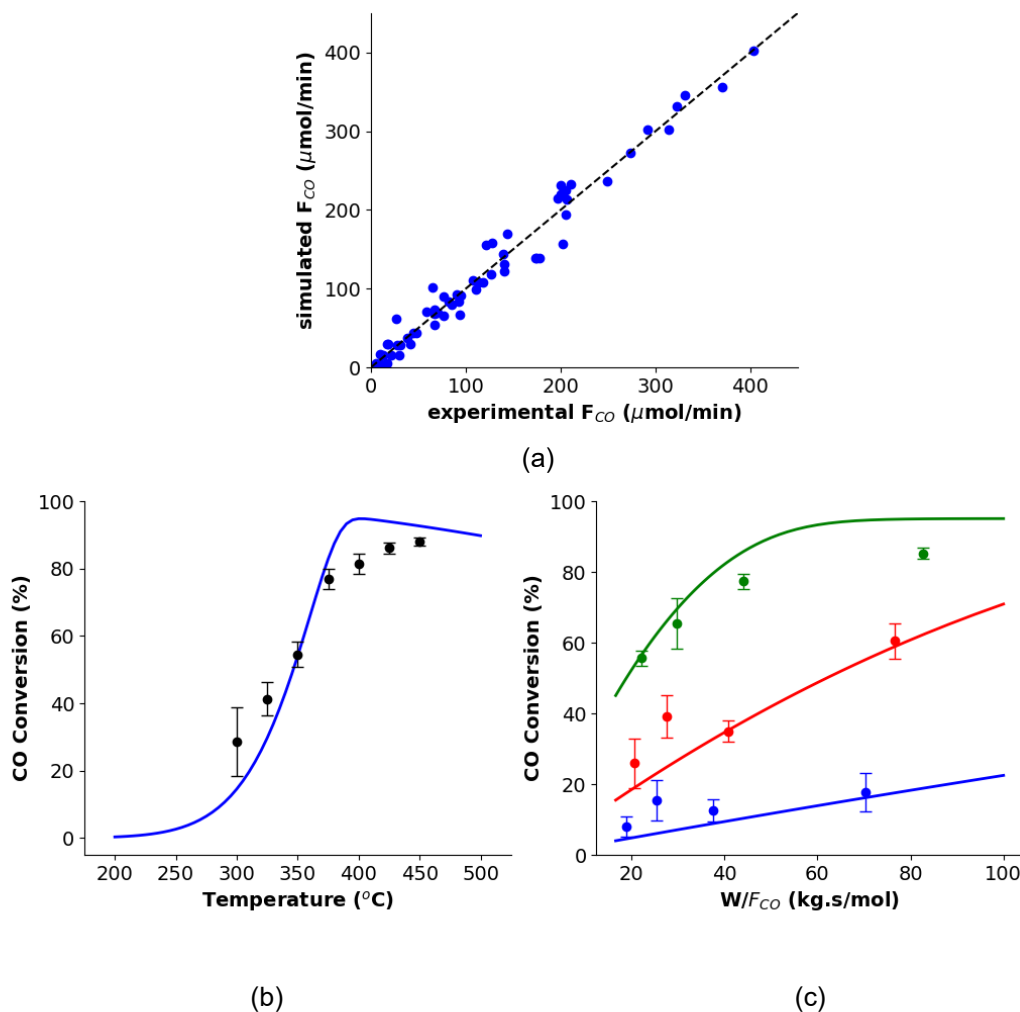


Figure 5.2 – (a) Parity plot of molar flow rates of CO. Performance curves of CO conversion as a function (b) of temperature and (c) of space time, for the WGS reaction over the Co/Ce-Sr-MWCNT catalyst using model M2.

The Langmuir-Hinshelwood-Hougen-Watson (LHHW) model (M3) investigated in this work assumed that the rate-determining step (RDS) was the dual-site surface reaction $\text{CO}^* + \text{H}_2\text{O}^* \rightleftharpoons \text{H}_2^* + \text{CO}_2^*$. In this approach, it is assumed that all species (reactants and products) are adsorbed on the catalyst surface, which substantially increases the number of parameters to be estimated (10 parameters: $k_{T_{ref}}$, $K_{T_{ref},\text{CO}}$, $K_{T_{ref},\text{H}_2\text{O}}$, K_{T_{ref},H_2} , K_{T_{ref},CO_2} , E_a , $\Delta H_{ads,\text{CO}}$, $\Delta H_{ads,\text{H}_2\text{O}}$, $\Delta H_{ads,\text{H}_2}$, and $\Delta H_{ads,\text{CO}_2}$). Despite having the lowest RMSD value and the best R^2 (very close to 1) among all models, the dual-site LHHW (M3) presented confidence intervals greater than the values of the parameters themselves, including zero and negative values for kinetic constants (Table 5.7 and Figure 5.3), which are misleading. This points overparameterization, when the degree of detail of the model is beyond the information available in the kinetic data (DEVOCHT *et al.*, 2019). Given that this novel catalyst has been tested in a broad range of conditions, which include the industrially most relevant ones, the added value of acquiring kinetic data outside this range is considered to be limited. Therefore, M3 is not further considered.

Table 5.7 – Estimated kinetic parameters for the WGS reaction over the Co/Ce-Sr-MWCNT catalyst of the model represented by the LHHW mechanism (M3).

Parameter	Value
$k_{T_{ref}}$	$(2.6 \pm 17.3) \times 10^6$
$K_{T_{ref},\text{CO}}$	$(1.2 \pm 7.4) \times 10^1 \text{ atm}^{-1}$
$K_{T_{ref},\text{H}_2\text{O}}$	$(2.2 \pm 8.0) \times 10^1 \text{ atm}^{-1}$
K_{T_{ref},H_2}	$(4.4 \pm 14) \times 10^1 \text{ atm}^{-1}$
K_{T_{ref},CO_2}	$(6.0 \pm 2909) \times 10^{-2} \text{ atm}^{-1}$
E_a	$53 \pm 433 \text{ kJ/mol}$
$\Delta H_{ads,\text{CO}}$	$20 \pm 406 \text{ kJ/mol}$
$\Delta H_{ads,\text{H}_2\text{O}}$	$1 \pm 231 \text{ kJ/mol}$
$\Delta H_{ads,\text{H}_2}$	$-130 \pm 240 \text{ kJ/mol}$
$\Delta H_{ads,\text{CO}_2}$	$-365 \pm 28850 \text{ kJ/mol}$

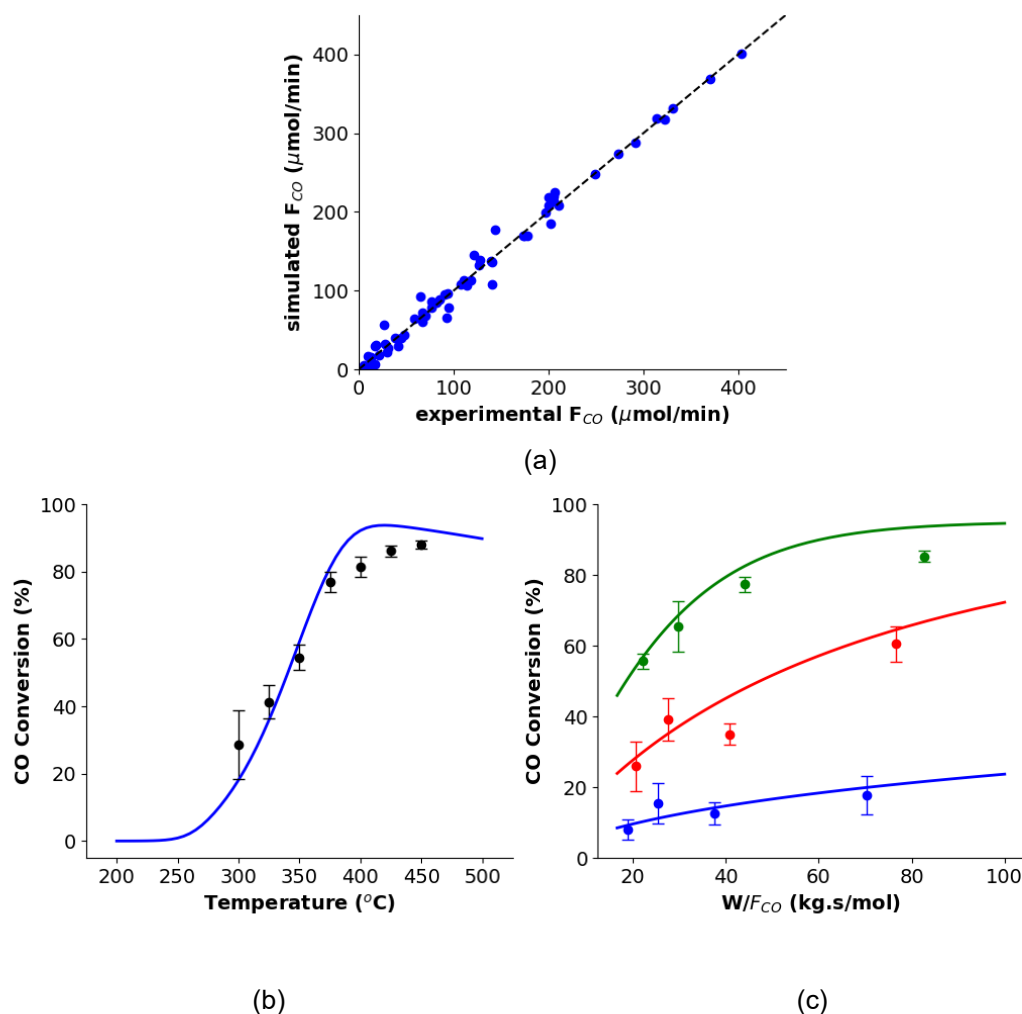


Figure 5.3 – (a) Parity plot of molar flow rates of CO. Performance curves of CO conversion as a function (b) of temperature and (c) of space time, for the WGS reaction over the Co/Ce-Sr-MWCNT catalyst using model M3.

Considering that H_2O and H_2 are weakly adsorbed on the catalyst surface, an Eley-Rideal mechanism was proposed (M4), with a single-site surface reaction as the RDS: $\text{CO}^* + \text{H}_2\text{O} \rightleftharpoons \text{H}_2 + \text{CO}_2^*$. The total number of parameters in this case was 6: $k_{T_{ref}}$, $K_{T_{ref},CO}$, K_{T_{ref},CO_2} , E_a , $\Delta H_{ads,CO}$, and $\Delta H_{ads,CO_2}$. The regression metrics are lower than those of M3, and similar to those of M1 and M2. Nevertheless, as can be seen in Table 5.8 and Figure 5.4, the estimated adsorption coefficients of CO and CO_2 are again statistically nonsignificant, i.e., there are enough statistical arguments to remove them from the model.

Table 5.8 – Estimated kinetic parameters for the WGS reaction over the Co/Ce-Sr-MWCNT catalyst of the model represented by the Eley-Rideal mechanism (M4).

Parameter	Value
$k_{T_{ref}}$	$(4.1 \pm 3.3) \times 10^4 \mu\text{mol g}^{-1}\text{atm}^{-2}\text{min}^{-1}$
$K_{T_{ref},CO}$	$0 \pm 4 \text{ atm}^{-1}$
K_{T_{ref},CO_2}	$7.6 \pm 20.2 \text{ atm}^{-1}$
E_a	$86 \pm 52 \text{ kJ/mol}$
$\Delta H_{ads,CO}$	$-104 \pm 0 \text{ kJ/mol}$
$\Delta H_{ads,CO_2}$	$-159 \pm 235 \text{ kJ/mol}$

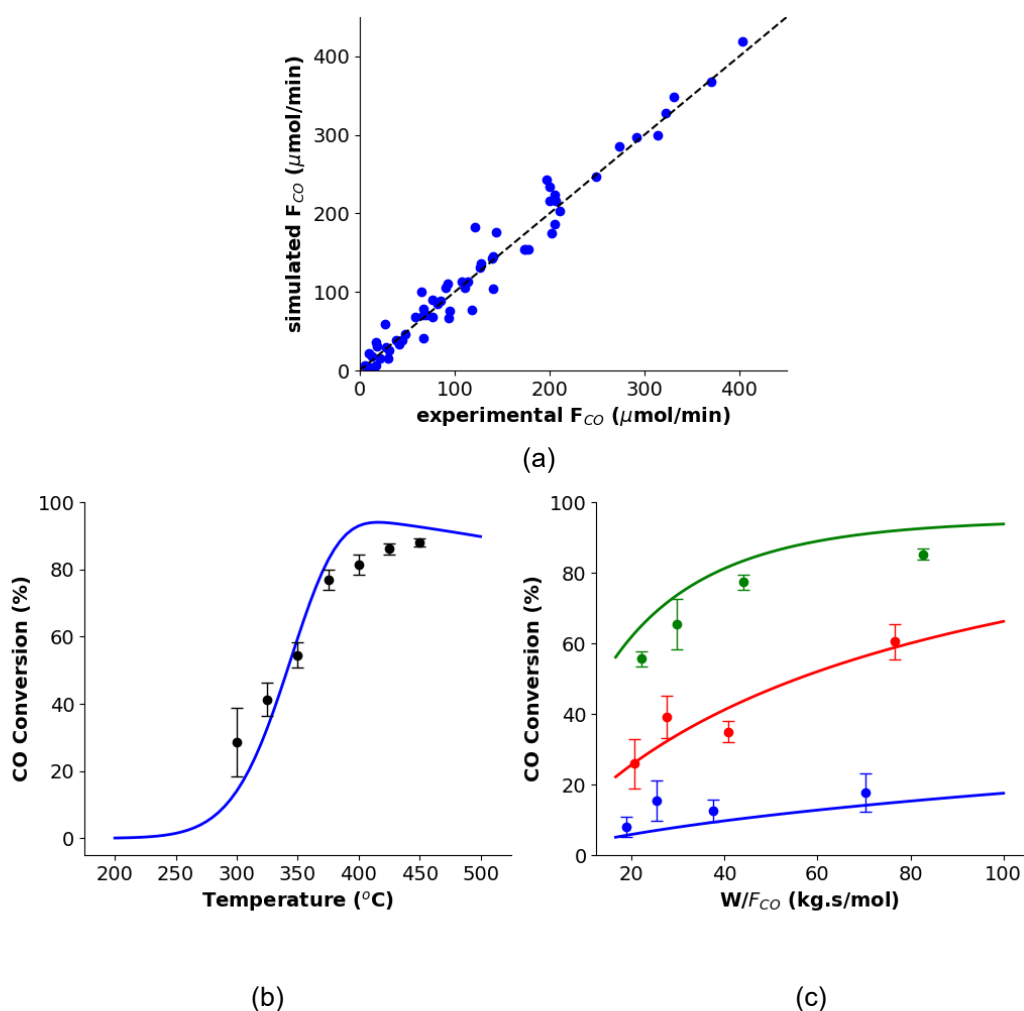


Figure 5.4 – (a) Parity plot of molar flow rates of CO. Performance curves of CO conversion as a function (b) of temperature and (c) of space time, for the WGS reaction over the Co/Ce-Sr-MWCNT catalyst using model M4.

The perfect balance between the degree of detail and acquired kinetic data was found with the redox mechanism (M5). In this formulation, H₂O is reduced on the catalyst surface forming H₂ and O*, followed by CO oxidation to CO₂, which was assumed to be the RDS. Thus, the number of estimated parameters amounts to 4 (same number of M2, which was the last statistically reliable one). The kinetic parameters are present in Table 5.9. As can be noted, all the estimated parameters are statistically significant, thus having a clear meaning and value reasons to be maintained in the model.

Moreover, the difference $E_a - \Delta H_{ads,H_2O} = 54 \text{ kJ mol}^{-1}$ represents the overall activation energy that is in agreement with the range reported by Newsome et al. (1980) for the WGS reaction: 49-89 kJ mol⁻¹ (NEWSOME, 1980). The parity plot (Figure 5.5a) confirms the great model adjustment to the data, with the lowest RMSD value (compared to M1 and M2, which also presented reliable parameters). In addition, the performance curves of CO conversion as a function of temperature and of space time (Figure 5.5b-c) visualize this excellent agreement, showing that the experimental data can be accurately reproduced by the model simulations successfully describing the observed behavior of the catalytic tests. Finally, the model was globally significant with the calculated *F*-value of 1 x 10³ greatly exceeding the tabulated one of 3.

Table 5.9 – Estimated kinetic parameters for the WGS reaction over the Co/Ce-Sr-MWCNT catalyst of the model represented by the redox mechanism (M5).

Parameter	Value
$k_{T_{ref}}$	$(3.1 \pm 1.8) \times 10^3 \text{ } \mu\text{mol g}^{-1}\text{atm}^{-1}\text{min}^{-1}$
K_{T_{ref},H_2O}	$(2.8 \pm 2.6) \times 10^{-1}$
E_a	$199 \pm 41 \text{ kJ mol}^{-1}$
$\Delta H_{ads,H_2O}$	$145 \pm 69 \text{ kJ mol}^{-1}$

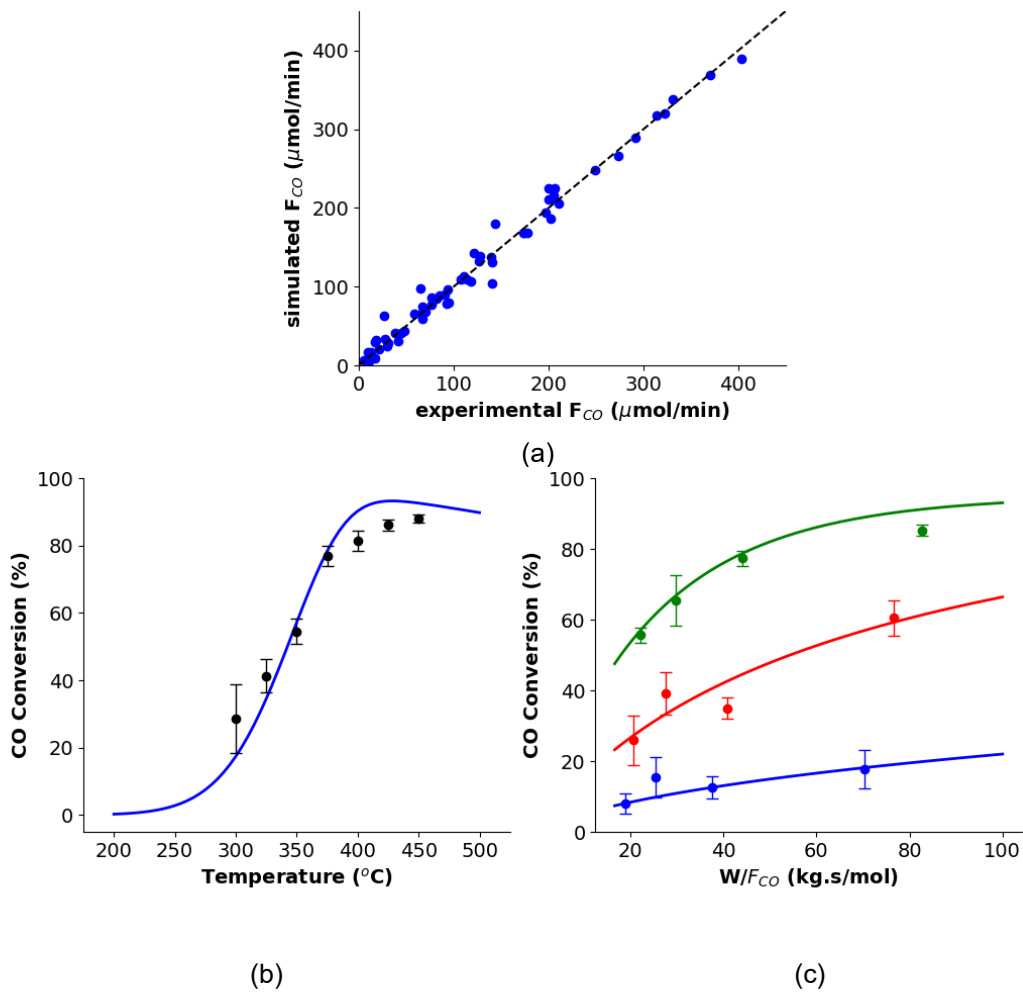


Figure 5.5 – (a) Parity plots of molar flow rates of CO. Performance curves of CO conversion as a function (b) of temperature and (c) of space time, for the WGS reaction over the Co/Ce-Sr-MWCNT catalyst using model M5.

It is noteworthy to mention that as the objective function, F_{obj} , in Eq. (17) is the appropriate definition of chi-square (χ^2). Thus, its value at the end of the estimation procedure follows the chi-square distribution with a degree of freedom DF of $NE.NY - NP$. In this way, a probability ϕ_m was computed for each model according to Eq. (19) (SCHWAAB; PINTO, 2011).

$$\phi_m = 1 - P(\chi_{DF}^2 \leq F_{obj}) \quad (19)$$

This statistical discrimination procedure is based on the chi-square distribution and provides an absolute probability, as each model is evaluated independently. If ϕ_m is low for the models under study (i.e., having high values of F_{obj}), an improvement of such models or the inclusion of new ones in the discrimination analysis should be

considered. In other words, if the model can represent the experimental data, Eq. (20) is satisfied, considering a 95% confidence level (chi-squared test):

$$\chi_{2,5\%,DF}^2 < F_{obj} < \chi_{97,5\%,DF}^2 \quad (20)$$

If $F_{obj} < \chi_{2,5\%,DF}^2$ (or $\phi_m < 2,5\%$), one can say that the model is inappropriate to represent the data, and must be removed from the analysis. In the other hand, if $F_{obj} > \chi_{97,5\%,DF}^2$ (or $\phi_m > 97,5\%$), the model is considered too good and should be revised: either the model is overparameterized or the experimental variances are very high (SCHWAAB; PINTO, 2011).

Moreover, the calculation of the relative probability P_m , Eq. (21), helps to discriminate a model from the others in the analysis of all M models considered:

$$P_m = \frac{\phi_m}{\sum_{n=1}^M \phi_m} \quad (21)$$

The results of this statistical analysis of the model discrimination procedure are presented in Table 5.10.

Table 5.10 – Statistical analysis of the model discrimination procedure

	M1	M2	M3	M4	M5
DF	58	56	50	54	56
$\chi_{2,5\%,DF}^2$	38,8	37,2	32,4	35,6	37,2
$\chi_{97,5\%,DF}^2$	80,9	78,6	71,4	76,2	78,6
F_{obj}	$4.5 \cdot 10^3$	$3.7 \cdot 10^3$	$1.7 \cdot 10^3$	$4.4 \cdot 10^3$	$1.9 \cdot 10^3$
$P(\chi_{DF}^2 \leq F_{obj})$	1	1	1	1	1
ϕ_m	0	0	0	0	0
P_m	NaN	NaN	NaN	NaN	NaN

*NaN – Not a Number (indeterminate form 0/0)

As can be noted, all values of the objective function, F_{obj} , are greater than $\chi_{2,5\%,DF}^2$, indicating that all models can reproduce the experimental data well. However, they are also greater than $\chi_{97,5\%,DF}^2$, indicating that none of the models are able to explain the experimental errors. Thus, the prediction errors may be significantly greater than the experimental ones, showing that the latter may be underestimated. In this situation, it is recommended to reevaluate the precision of the measures of the response flow rates of CO (computed from the replicated central point in the experimental design), since this encountered scenario (equal ϕ_m 's) leads to the conclusion that all rival kinetic models are statistically equal.

5.5 Discussion

There were previous WGS studies with other catalysts supported on MWCNTs, but at different conditions than this work, with activity reported in different formats, and/or with noble metals as active phases (more expensive). For instance, Dongil et al. (2016) developed a Ni/Ce-MWCNT catalyst for LT-WGS exhibiting higher conversions (~97%) at 260°C and similar operating conditions (DONGIL *et al.*, 2016), while the one built in this work presented approximately only 5% at 260°C. This confirms that the Co/Ce-Sr-MWCNT under this study is more suitable for the HT-WGS process. Zugic et al. (2014) investigated a Pt/Na-MWCNT catalyst, which presented better conversions (60-90%) at lower temperatures (250-350°C) (ZUGIC; BELL; FLYTZANI-STEPHANOPOULOS, 2014), again showing better performance for the LT-WGS reaction.

In addition, Mitchell et al. (2020) studied the cobalt addition to a Pt/MWCNT catalyst (MITCHELL *et al.*, 2020), however did not report the results in terms of CO conversion (they used the WGS turnover rate at 300°C), which makes comparison difficult. The power-law model used to estimate the kinetic parameters resulted in reaction orders (-0.26 to 0.1 for CO, and 0.75 to 1.1 for H₂O) very different from those found in this work, due to the presence of the noble metal Pt in the catalyst matrix. While Beltram et al. (2015) developed Pd@CeO₂/MWCNT catalysts, with higher surface area (64-186 m²/g) and the activity expressed in CO consumption. Also, they

did not perform a kinetic study (BELTRAM *et al.*, 2015), again making comparison difficult.

The kinetic model M5 derived from the redox mechanism was capable of nicely reproducing the WGS kinetics over the Co/Ce-Sr-MWCNT catalyst. Besides exhibiting a statistically significant regression $R^2 \approx 0.98$ and the lowest RMSD compared to the power law models (M1 and M2) which are also statistically significant. The statistical significance is very important for the prediction capacity of the model within the range of experimental operating conditions considered in tasks such as the design, simulation, and control of a chemical process.

Therefore, there are clear indications that the WGS reaction over the Co/Ce-Sr-MWCNT catalyst follows the redox mechanism, which is also known as the regenerative mechanism (REDDY; SMIRNIOTIS, 2015), by which the HT-WGS is better explained (SMITH R J; LOGANATHAN; SHANTHA, 2010). The catalyst surface is oxidized by water forming hydrogen gas, followed by the surface reduction to transform carbon monoxide to dioxide, as schematized in Table 5.3.

Further indication for this mechanism can be found in the structure and composition of the Co/Ce-Sr-MWCNT catalyst. As confirmed by XRD, Raman, and EDX, the presence of Co and CeO₂ in the catalyst matrix plays an important role for WGS activity. The presence of ceria shifts the reduction of cobalt oxides to lower temperatures, as demonstrated in H₂-TPR results. Ceria also promotes a high mobility of the oxygen species over the MWCNTs surface, which already has the presence of oxygenated groups because of the functionalization. This strong interaction between the catalyst components makes the cobalt a source of stabilization of water molecules, favoring the surface oxidation: $\text{H}_2\text{O} + * \rightleftharpoons \text{O}^* + \text{H}_2$ (BARAJ; CIAHOTNÝ; HLINČÍK, 2021). The existence of a high density of active phase (*) on the catalyst surface is confirmed by the CO chemisorption results. Therefore, the availability and mobility of O* surface species on the catalyst surface, which is also promoted by the extended π -conjugation bonds of the MWCNTs, plays an important role in accelerating the reaction rate: $\text{CO} + \text{O}^* \rightleftharpoons * + \text{CO}_2$.

Moreover, the presence of the metal nanoparticles mainly at the external surface of the MWCNTs, confirmed by N₂-physisorption, TEM images and Raman spectra, confirms that this whole process occurs at the external surface and not inside the nanotubes. The latter which could cause mass transfer limitations, which have clearly been avoided.

5.6 Conclusions

Via model discrimination, the redox mechanism was identified as most suitable to explain the WGS over the Co/Ce-Sr-MWCNT catalyst. Furthermore, this redox behavior was perfectly aligned with the catalyst characterization results. This was *the first time* that kinetic parameters for the well-studied WGS reaction have been estimated for carbon-support catalysts. Thus, this developed nanostructured catalyst appears to have a promising future for industrial use in the high-temperature WGS reaction. Furthermore, this model can be a useful tool for such future use, even more as the parameters have been estimated at industrially relevant CO conversions.

6 CHAPTER IV: MICROKINETIC STUDY

6.1 Introduction

For most catalytic reactor designs, *macrokinetic* models are used to describe the reaction. Rates are then generally represented in terms of power-law expressions or, in the best scenario, of Langmuir-Hinshelwood mechanisms. However, such models are limited to specific catalysts and provide little information for catalyst design, although they have a lower computational cost (SAW; NANDONG; GHOSH, 2016). The development of *microkinetic* models, on the other hand, allows gaining an understanding of fundamental catalyst surface phenomena in terms of elementary reaction steps, yielding more accurate reaction rates (DUMESIC *et al.*, 1993).

This methodology takes the physical and chemical catalyst properties into account as part of the model formulation. The corresponding parameters, referred to *catalyst descriptors*, can, ideally speaking, be computed from theoretical chemistry or experimentally measured, thus assisting in the search of new or improved catalysts for a particular process (THYBAUT *et al.*, 2011).

Some of these descriptors are the density of active sites, σ [$\text{mol}_{\text{Act.Surf.}} \text{m}_{\text{cat}}^{-2}$], which provides the number of available active sites on the catalyst surface, where the elementary steps of the reaction mechanism take place (SUN; THYBAUT; MARIN, 2008), and the specific surface area, S_P [$\text{m}^2 \text{kg}_{\text{cat}}^{-1}$], which quantifies the potential for interaction between gas molecules and the catalyst surface through adsorption-desorption steps (SCHMAL, 2016).

Moreover, they can also be chemisorption enthalpies, initial sticking probabilities, binding energies of intermediates, among others (SUN; THYBAUT; MARIN, 2008). Furthermore, the incorporation of these descriptors into *microkinetic* models is a powerful procedure to extract knowledge from high throughput experimentation in the search for new or improved catalysts for a process, allowing the prediction of reaction performance – conversion, activity, and selectivity – based on intrinsic catalyst properties (THYBAUT *et al.*, 2011). Hence, the catalyst composition and structure can be changed to adjust the appropriate rate parameters.

These *microkinetic* models are derived from the investigation of catalytic cycles and the catalyst surface, and they portray the reaction in terms of elementary

steps concerning adsorbed reactants, products, and reaction intermediates related to active sites (SUN; THYBAUT; MARIN, 2008). In addition, they can be employed for identifying the rate-determining step (RDS) or the most abundant reactive intermediates (MARI) without *a priori* assumptions on elementary reactions, since they can describe the reacting system behaviour under distinct operating conditions (MAESTRI *et al.*, 2009).

In addition, a matter of concern is about the computational time required in the implementation of *microkinetic* models due to the large number of differential equations to be solved, which come from the complex reaction network. However, model reduction techniques were developed elsewhere (MAESTRI *et al.*, 2008) to make feasible their applications in online process control and computational fluid dynamics (CFD) simulations (MAESTRI; CUOCI, 2013). For example, the Principal Component Analysis (PCA) method has been applied with this purpose, using information from Sensitivity Analysis (SA) in a full microkinetic model, and thus reducing the number of reactions in the mechanism (DE CARVALHO *et al.*, 2018).

For the WGS reaction over Cu-ZnO-Al₂O₃ catalysts, *microkinetic* models were applied using a systematic reaction route (RR) analysis, showing that only three RRs dominate its kinetics: the formate, the associative, and the redox mechanisms (CALLAGHAN *et al.*, 2003). From a *microkinetic* model based on the associative mechanism, it was proved that the oxidation of CO* by H₂O*, forming COOH* and H*, is the rate-determining step of WGS reaction on Pt (MHADESHWAR; VLACHOS, 2005). Moreover, a more robust model was developed with a closed catalytic cycle suggested from DFT calculation results, identifying that intermediate binding energies are relevant parameters for the process (MADON *et al.*, 2011). There are other works regarding the WGS reaction *microkinetics* over other catalysts, such as Au/MgO (ZHAO *et al.*, 2017) and Pd-Cu/CeO₂ (LUO *et al.*, 2018), showing the critical influence of the metal/support interface on the catalysis.

Moreover, *in situ* characterization techniques can help in elucidating the WGS reaction mechanism. For instance, *in situ* DRIFTS showed that the production of CO₂ goes through the reaction between CO and O* species coming from the dissociation of OH* species on catalysts of Au supported on Zn-Al/Cr/Fe layered double hydroxides (MENG *et al.*, 2020). Such result can be supported by DFT calculations, which showed

that the redox mechanism has the lowest energy barriers and is the most potential reaction pathway to be used in microkinetic modeling.

The aggregate analysis of DFT, microkinetic, and experimental studies are essential key kinetic descriptors for reactions occurring at metal/oxide interface. Using this combination, a dual-site microkinetic model was built to explain the role of the interface of a Pt/MgO catalyst for the WGS reaction with 17 elementary steps and 16 species, revealing that the carboxyl mechanism is the governing pathway when accounting for relevant CO coverages (GHANEKAR *et al.*, 2020).

This chapter aimed at developing a microkinetic model that best describes the Water-Gas Shift (WGS) reaction, i.e., one of the major routes for hydrogen production over the Co/Ce-Sr-MWCNT catalyst under study. In this way, an appropriate and comprehensive reaction mechanism for the WGS reaction was proposed to describe the kinetics over this catalyst.

6.2 Methodology

The microkinetic methodology is based on the elementary steps that constitute the reaction mechanism without considering, in principle, a rate-determining step. Although it is computationally intensive, such a detailed description of the reaction chemistry allows understanding the fundamental catalyst surface phenomena taking place, justifying the additional (computational) effort. In this study, we formulated the microkinetic model based on a well-known mechanism for the WGS reaction involving a highly reactive surface intermediate – the carboxyl (COOH*), according to the following elementary steps in Table 6.1 (GOKHALE; DUMESIC; MAVRIKAKIS, 2008).

Table 6.1 – Reaction mechanism considered for the microkinetic model of the WGS over a Co catalyst supported on MWCNT with its parameter values (the estimated ones are shown in bold with the corresponding 95% confidence interval. The adsorption/desorption steps are shown in blue, while the surface reaction ones are shown in red. The fixed parameters were used from GOKHALE; DUMESIC; MAVRIKAKIS (2008).

#	Elementary steps	k_o [min^{-1}]	E_a [kJ mol^{-1}]
1	$\text{CO} + * \rightarrow \text{CO}^*$	$4.62 \times 10^{11} \text{ atm}^{-1}$	0
-1	$\text{CO}^* \rightarrow \text{CO} + *$	7.79×10^{14}	42.3
2	$\text{H}_2\text{O} + * \rightarrow \text{H}_2\text{O}^*$	$5.76 \times 10^{11} \text{ atm}^{-1}$	0
-2	$\text{H}_2\text{O}^* \rightarrow \text{H}_2\text{O} + *$	7.79×10^{14}	54.3
3	$\text{H}_2\text{O}^* + * \rightarrow \text{OH}^* + \text{H}^*$	$6.57 \times 10^{14} \text{ g } \mu\text{mol}^{-1}$	20.7
-3	$\text{OH}^* + \text{H}^* \rightarrow \text{H}_2\text{O}^* + *$	$6.57 \times 10^{14} \text{ g } \mu\text{mol}^{-1}$	0
4	$\text{CO}^* + \text{OH}^* \rightarrow \text{COOH}^* + *$	$6.57 \times 10^{14} \text{ g } \mu\text{mol}^{-1}$	48.1 ± 12.3
-4	$\text{COOH}^* + * \rightarrow \text{CO}^* + \text{OH}^*$	$4.10 \times 10^{14} \text{ g } \mu\text{mol}^{-1}$	112.9 ± 8.0
5	$\text{COOH}^* + * \rightarrow \text{CO}_2^* + \text{H}^*$	$9.03 \times 10^{14} \pm 4.02 \times 10^5 \text{ g } \mu\text{mol}^{-1}$	20.1 [†]
-5	$\text{CO}_2^* + \text{H}^* \rightarrow \text{COOH}^* + *$	$6.57 \times 10^{14} \text{ g } \mu\text{mol}^{-1}$	0.01
6	$2\text{H}^* \rightarrow \text{H}_2 + 2^*$	7.79×10^{14}	47.4 ± 11.3
-6	$\text{H}_2 + 2^* \rightarrow 2\text{H}^*$	$(3.86 \pm 0.41) \times 10^8 \text{ g } \mu\text{mol}^{-1} \text{ atm}^{-1}$	0
7	$\text{CO}_2^* \rightarrow \text{CO}_2 + *$	7.79×10^{14}	32.0
-7	$\text{CO}_2 + * \rightarrow \text{CO}_2^*$	$3.68 \times 10^{11} \text{ atm}^{-1}$	0

[†] thermodynamic constraint

Source: (CAVALCANTI *et al.*, 2020)

In Table 6.1, * represents the free active sites and X* the adsorbed species on the catalyst surface (intermediates). The adsorption/desorption steps are shown in blue, while the surface reaction ones are shown in red. In this microkinetic methodology, apart from the set of ordinary differential equations describing the mass balance of each bulk species (Eq. (21)), the pseudo-steady state approximation for the intermediates (Eq. (22)), and the mass balance of the active sites (Eq. (23)) were also taken into account (POISSONNIER *et al.*, 2018):

$$\frac{dF_i}{dW} = R_i \quad \text{with} \quad F_i = F_{i,inlet} \quad \text{at} \quad W = 0 \quad (22)$$

$$R_{intermediate} = 0 \quad (23)$$

$$C_{total} = C_* + \sum C_{intermediate} \quad (24)$$

F_i is the molar flow rate of component i ($\mu\text{mol min}^{-1}$), W the catalyst mass (g), R_i the net production rate of component i ($\mu\text{mol g}^{-1} \text{min}^{-1}$), $R_{intermediate}$ the net production rate of each intermediate ($\mu\text{mol g}^{-1} \text{min}^{-1}$), C_{total} the total active site concentration (mol g^{-1}), C^* the free active site concentration (mol g^{-1}), and $C_{intermediate}$ the occupied active site concentration (mol g^{-1}). The resulting system of differential-algebraic equations (DAEs) (21)-(23) was solved using the DDAPLUS package, and the regression made by the GREGPLUS package, both as available in Athena VISUAL Studio. The kinetic data used for the model adjustment were collected from 60 experiments (Table 5.1), varying the temperature, feed composition, and space velocity.

The microkinetic modeling uses kinetic parameters that exhibit a clear physicochemical meaning. As the model has a large set of adjustable parameters (a total of 28), only a subset of them could be estimated from the kinetic data without compromising the accuracy. Therefore, the others were calculated using theoretical prediction models, such as the Collision Theory and Transition-State Theory, respectively and kept fixed during the regression (SPRUNG *et al.*, 2015):

$$k_{io} = \frac{S_P}{\sigma} \frac{1}{\sqrt{2\pi MRT}} \quad (25)$$

$$k_{io} = \frac{N_A}{S_P} \frac{k_B T}{h} \frac{Q_{AB\ddagger}''}{Q_{A^*}'' Q_{B^*}''} \quad (26)$$

k_{io} is the pre-exponential factor for adsorption [$\text{Pa}^{-1} \text{s}^{-1}$], reaction [$\text{kg mol}^{-1} \text{s}^{-1}$] or desorption [s^{-1}], S_P is the catalyst specific surface area [$\text{m}^2 \text{kg}_{\text{cat}}^{-1}$], σ the active site density [$\text{mol}_{\text{Act.Surf.}} \text{kg}_{\text{cat}}^{-1}$], M the molar mass of the gas species [kg mol^{-1}], N_A the Avogadro constant [mol^{-1}], k_B the Boltzmann constant [J K^{-1}], h the Planck constant [J s], and Q_i'' the molecular partition function of the involved species i [m^{-2}].

In other words, these theories were used to complement the available information presented in the experimental data, which was not sufficient to estimate all rate coefficients (DEVOCHT *et al.*, 2019). In addition, in order to further reduce the number of estimated parameters, beyond the theoretical calculations, some of the activation energies values were obtained from other modeling efforts performed on a similar catalyst (SPRUNG *et al.*, 2015).

The catalyst descriptors (S_p and σ) used in those expressions were experimentally determined from characterization techniques. The catalyst specific surface area was acquired from N_2 physisorption isotherms (NOVA 1200e Surface Area & Pore Size Analyzer, from Quantachrome Instruments), using the BET method: $S_p = 2200 \text{ m}^2 \text{ kg}_{cat}^{-1}$ (section 4.4.1.1). While, the catalyst activity site density was computed from CO pulse chemisorption measurements (Autochem II, from micromeritics®) assuming an equimolar stoichiometry of CO-cobalt: $\sigma = 0.012 \text{ mol}_{Act.Surf.} \text{ kg}_{cat}^{-1}$ (section 4.4.1.7).

In addition, energetic consistency is ensured in the model, by expressing that the appropriate sum of the activation energies for all elementary steps must be equal to the overall standard enthalpy of the WGS reaction (DUMESIC *et al.*, 1993; SPRUNG *et al.*, 2015):

$$\sum_j \nu_j(E_{j,for}) - \sum_j \nu_j(E_{j,rev}) = \Delta H_{WGS}^0 = -41 \text{ kJ mol}^{-1} \quad (27)$$

ν_j is the stoichiometry number of the elementary steps in the reaction mechanism, E_j the activation energy of the forward (for), and reverse (rev) steps [kJ mol^{-1}], and ΔH_{WGS}^0 the standard enthalpy of the WGS reaction [kJ mol^{-1}].

6.3 Results and discussion

The estimated kinetic parameter values with their corresponding confidence intervals are presented in Table 6.1. As can be noted, five parameters were estimated from the collected kinetic data (all statistically significant), while the other 23 were determined *a priori* as discussed above. The main challenge in the parameter estimation was to find and tune the balance between the amount of information available in the kinetic data and the degree of detail retained in the model.

In Figure 6.1, the performance curves and the parity plots are presented, showing that the microkinetic model seems to reasonably describe the behavior of the experimental data, with the catalyst presenting an optimal performance ($X_{CO} = 85\text{-}95\%$) at elevated temperatures (350-450°C) and space times (70-80 kg s mol^{-1}). As expected, the higher the temperature and space velocity, the greater the CO conversion.

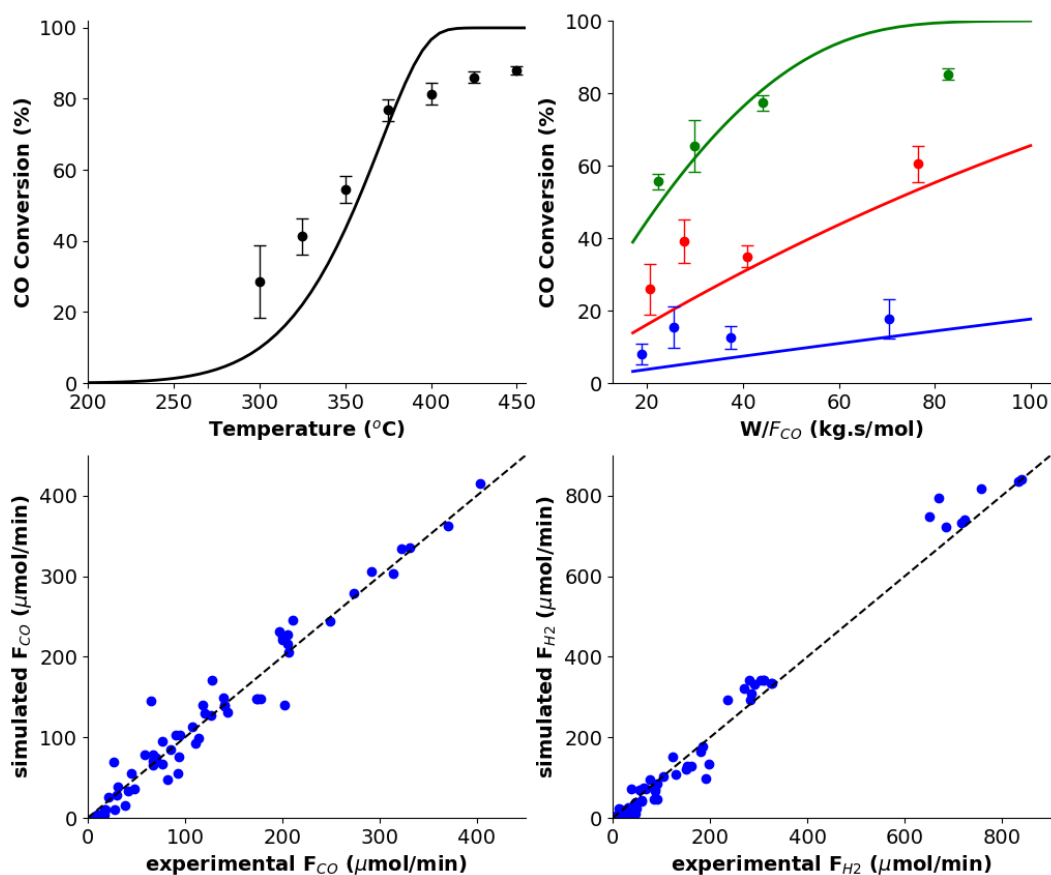


Figure 6.1 – Performance curves and parity plots. In the former, points are experimental data, and lines represent the model predictions. The CO conversion as a function of the temperature curve was carried out with space time of 88 kg s mol^{-1} . For the CO conversion as a function of space time graphs, the blue line represents the reaction performed at 300°C , the red at 350°C , and the green at 400°C .

Source: (CAVALCANTI *et al.*, 2020)

This appropriate agreement between observed and predicted values is also confirmed by the R^2 value of 0.96, and the F -test for verifying the global significance of the regression: $F_{\text{calc}} = 10^3 (> F_{\text{tab}} = 4)$. Also, the experimental points show a good distribution along the 45° line in the parity plots, being more symmetrical for CO. However, model simulated data at temperatures above 400°C are exceeding the equilibrium conversion, hence indicating where the discrepancy between experimental and model simulated data originates from. This may be overcome by considering the calculation of the reverse reaction rate coefficients, not by using the Collision and Transition-State theories, but rather by enforcing thermodynamic equilibrium for each elementary step ($K_j = k_{j,\text{for}}/k_{j,\text{rev}}$), which involves the knowledge of the standard Gibbs energy of all the intermediate species presented in the mechanism (DE CARVALHO *et al.*, 2018). In this way, together with the energetic constraint in Eq. (26), the overall

thermodynamic consistency would be guaranteed. In addition, for the CO conversion as a function of space time graphs, the higher the temperature, the better seems the adjustment for lower W/F_{CO} values. Thus, the model seems to work well in high temperature regions, but far from equilibrium and with small space times, potentially indicating that chemical kinetics are no longer dominating at this point and effects of heat and mass transfer are present.

It is worth noting that the macrokinetic models developed in CHAPTER III: (MACRO)KINETIC STUDY presented better model fits to the data. In addition to the reasons related to the thermodynamic equilibrium mentioned above, the worse fit may be emerged from various sources: inadequate calculation of partition functions, small dataset to perform a microkinetic regression, choice of the wrong parameters to be estimated, and failure to account for other elementary steps in the mechanism. In other words, the microkinetic model was formulated by invoking many approximations that ultimately lower its quantitative accuracy. In summary, the challenge of microkinetic modeling lies in the need to have quality information regarding the model parameter values, for which relatively little input is available.

Furthermore, the COOH* formation reaction ($CO^* + OH^* \rightarrow COOH^* + *$) has the highest activation energy of all surface reactions, as can be observed in the energy diagram (Figure 6.2) constructed with the activation energies in Table 6.1. Since k_o values are almost the same in all reactions, it can be inferred with the Arrhenius law ($k_j = k_{o,j} \exp(-E_{a,j}/RT)$) that the higher the activation energy, the lower the rate coefficient. Therefore, reaction #4 can be considered the rate-determining step for the WGS reaction over the Co/MWCNT catalyst, as its rate has the greatest sensitivity with temperature variation. In addition, the partial equilibrium ratio ($= r_{j,for}/r_{j,for}+r_{j,rev}$) for this elementary reaction (with a value of 0.99, greater than 0.5) proves that it is forward favorable, and the conclusion above can be actually supported. Finally, in the diagram, the thermodynamic constraint incorporated into the model (Eq. 6) can be observed by the energy difference between the reactants and the products, being equal to $\Delta H_{WGS}^o = -41 \text{ kJ mol}^{-1}$ (PAL *et al.*, 2018).

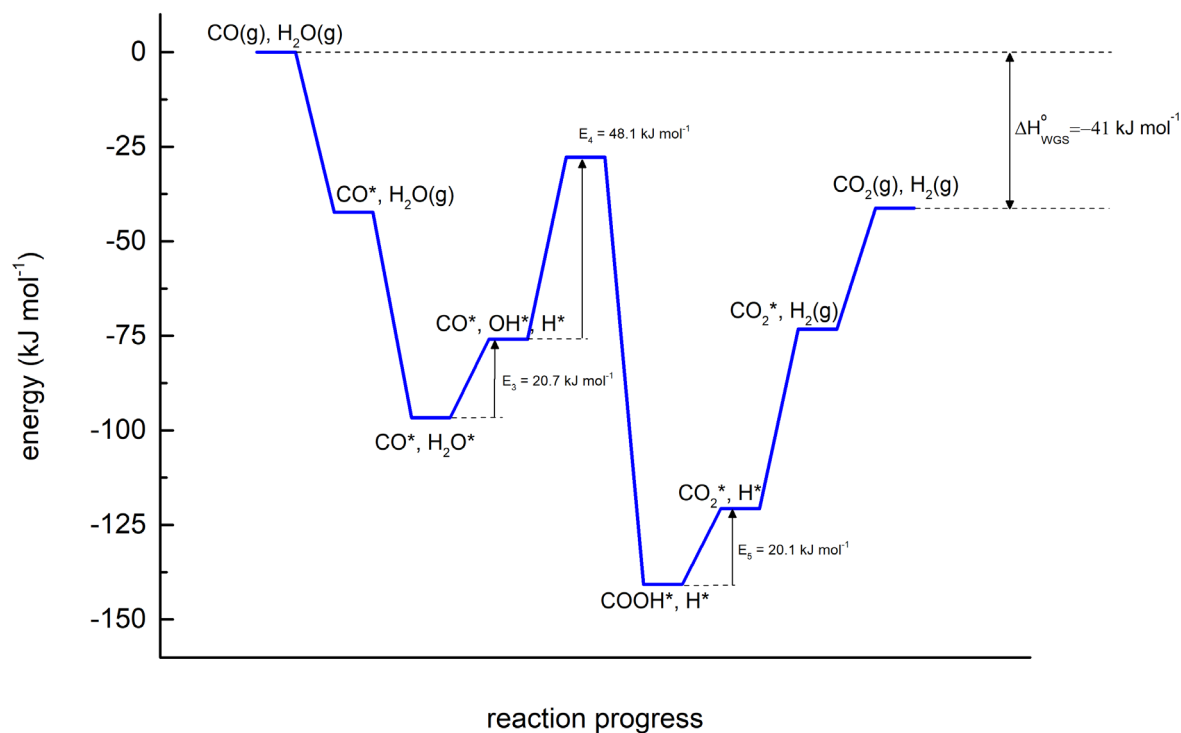


Figure 6.2 – Energy diagram of the WGS reaction mechanism according to the values in Table 6.1.

Source: (CAVALCANTI *et al.*, 2020)

6.4 Conclusions

The development of this microkinetic model allowed the determination of more detailed kinetics for the WGS reaction over the Co/MWCNT catalyst, considering catalyst surface properties, such as its specific surface area and its density of active sites. The incorporation of these catalyst descriptors into this model confirms that the COOH^* formation reaction ($\text{CO}^* + \text{OH}^* \rightarrow \text{COOH}^* + *$) is the rate-determining step and allows describing the optimal catalyst performance at elevated temperatures (350-450°C) and space times (70-80 kg.s/mol), as indicated by the experimental results. Therefore, it is a robust procedure for predicting reaction performance based on intrinsic catalyst properties, thus assisting in future catalyst design and optimization research.

However, it is important to mention that the macrokinetic models presented better adjustments in comparison to the microkinetic one developed in this chapter. In other words, despite the huge theoretical potential of the microkinetic approach, there is not always a practical advantage to use it due to the little input available to estimate its parameters.

7 CONCLUSIONS AND SUGGESTIONS FOR FUTURE WORKS

The developed and characterized Co/Ce-Sr-MWCNT catalyst presented activity for the HT-WGS with CO conversion close to the thermodynamic limit. The redox mechanism was identified as the most suitable to describe its kinetics with oxidation and reduction cycles occurring on the catalyst surface. This fact can be explained by the extended π -conjugation bonds of the MWCNTs and the oxygen storage capacity brought by CeO₂. Moreover, this was corroborated by the kinetic study which confirmed that the Langmuir-Hinshelwood model based on the redox mechanism was capable of nicely reproducing the WGS kinetics. It is noteworthy that this was *the first time* that kinetic parameters have been estimated for WGS reaction over carbon-support catalysts. A microkinetic approach with an understanding of fundamental catalyst surface phenomena in terms of elementary steps has also been developed to comprehend the detailed kinetics of this catalytic reaction. All this work together with the constructed ANN model is a robust consultancy material to assist in future catalyst design and optimization for industrial reactor projects.

For future works on this topic, the following suggestions are presented:

- Construction of a more robust ANN model with the use of a wider range of operating conditions in the experimental data to avoid some inconsistencies found in the results.
- Performance of economic viability studies related to the large-scale synthesis of the Co/Ce-Sr-MWCNT catalyst for industrial use.
- Execution of robust catalyst characterization techniques, such as Temperature-Programmed Superficial Reaction (TPSR) and *in situ* XRD to better understand the connection between the elementary steps of the microkinetic model with the surface reactions that occur in the catalyst structure.
- Use of machine learning techniques to improve the microkinetic model accuracy: using surrogate models to compute partition functions and activation energies.

- Introduction of macro and microkinetic models into a multiscale fixed-bed reactor design equation to identify the dominant phenomena at the different scales: nano, micro and macro.

REFERENCES¹

- ADAMS II, T. A.; BARTON, P. I. A dynamic two-dimensional heterogeneous model for water gas shift reactors. **International Journal of Hydrogen Energy**, v. 34, n. 21, p. 8877–8891, 2009.
- ALVES, R. M. B.; NASCIMENTO, C. A. O. Neural network based approach applied to for modeling and optimization an industrial isoprene unit production. **AIChE Annual Meeting, Conference Proceedings**, p. 7663–7682, 2004.
- BAKER, M.; PENNY, D. Is there a reproducibility crisis? **Nature**, v. 533, n. 7604, p. 452–454, 2016.
- BARAJ, E.; CIAHOTNÝ, K.; HLINČÍK, T. The water gas shift reaction: Catalysts and reaction mechanism. **Fuel**, v. 288, n. November 2020, 2021.
- BARRET, E.; JOYNER, L.; HALENDA, P. The Determination of Pore Volume and Area Distributions in Porous Substances. I. Computations from Nitrogen Isotherms. **Journal of the American Chemical Society**, v. 73, n. 1, p. 373–380, 1951.
- BAUMES, L.; FARRUSSENG, D.; LENGELIZ, M.; MIRODATOS, C. Using artificial neural networks to boost high-throughput discovery in heterogeneous catalysis. **QSAR and Combinatorial Science**, v. 23, n. 9, p. 767–778, 2004.
- BAYSAL, M.; GÜNAY, M. E.; YILDIRIM, R. Decision tree analysis of past publications on catalytic steam reforming to develop heuristics for high performance: A statistical review. **International Journal of Hydrogen Energy**, v. 42, n. 1, p. 243–254, 2017.
- BELTRAM, A.; MELCHIONNA, M.; MONTINI, T.; NASI, L.; GORTE, R. J.; PRATO, M.; FORNASIERO, P. Improved activity and stability of Pd@CeO₂ core–shell catalysts hybridized with multi-walled carbon nanotubes in the water gas shift reaction. **Catalysis Today**, v. 253, n. July, p. 142–148, 2015. Disponível em: <<http://linkinghub.elsevier.com/retrieve/pii/S0920586115002011>>.
- BRASIL, N. I.; ARAÚJO, M. A. S.; SOUSA, E. C. M. **Processamento de Petróleo e Gás: Petróleo e seus derivados, Processamento Primário, Processos de Refino, Petroquímica, Meio Ambiente**. 1st. ed. Rio de Janeiro: LTC, 2011.
- BROUWER, R. A Hybrid Network for Input that is both Categorical and Quantitative. **International Journal of Intelligent Systems**, v. 19, n. 10, p. 979–1001, 2004.

¹ De acordo com ABNT.

BRUNAUER, S.; EMMETT, P. H.; TELLER, E. Adsorption of Gases in Multimolecular Layers. **Journal of the American Chemical Society**, v. 60, n. 2, p. 309–319, 1938.

BUITRAGO, R.; RUIZ-MARTÍNEZ, J.; SILVESTRE-ALBERO, J.; SEPÚLVEDA-ESCRIBANO, A.; RODRÍGUEZ-REINOSO, F. Water gas shift reaction on carbon-supported Pt catalysts promoted by CeO₂. **Catalysis Today**, v. 180, n. 1, p. 19–24, 2012. Disponível em:

<<http://dx.doi.org/10.1016/j.cattod.2011.07.032>%5Cn<http://linkinghub.elsevier.com/retrieve/pii/S0920586111005761>>.

BUTLER, K. T.; DAVIES, D. W.; CARTWRIGHT, H.; ISAYEV, O.; WALSH, A. Machine learning for molecular and materials science. **Nature**, v. 559, n. 7715, p. 547–555, 2018.

CALLAGHAN, C.; FISHTIK, I.; DATTA, R.; CARPENTER, M.; CHMIELEWSKI, M.; LUGO, A. An improved microkinetic model for the water gas shift reaction on copper. **Surface Science**, v. 541, n. 1–3, p. 21–30, 2003.

CARBERRY, J. J. The catalytic effectiveness factor under nonisothermal conditions. **AIChE Journal**, v. 7, n. 2, p. 350–351, 1 jun. 1961.

CAVALCANTI, F. M.; POISSONNIER, J.; VANDEVYVERE, T.; GIUDICI, R.; BRITO ALVES, R. M.; SCHMAL, M.; THYBAUT, J. W. Microkinetic Modeling of the Water-Gas Shift Reaction over Cobalt Catalysts Supported on Multi-Walled Carbon Nanotubes. **Chemistry Proceedings**, v. 2, n. 1, p. 11, 2020.

CAVALCANTI, F. M.; SCHMAL, M.; GIUDICI, R.; BRITO ALVES, R. M. A catalyst selection method for hydrogen production through Water-Gas Shift Reaction using artificial neural networks. **Journal of Environmental Management**, v. 237, p. 585–594, maio 2019.

CHUNG, C. H.; TU, F. Y.; CHIU, T. A.; WU, T. T.; YU, W. Y. **Critical roles of surface oxygen vacancy in heterogeneous catalysis over ceria-based materials: A selected review** **Chemistry Letters** Chemical Society of Japan, 1 maio 2021.

CONSTALES, D.; YABLONSKY, G. S.; D’HOOGE, D. R.; THYBAUT, J. W.; MARIN, G. B. **Advanced Data Analysis and Modelling in Chemical Engineering**. 1st. ed. Amsterdam, Netherlands: Elsevier, 2017. 414 p.

DAMYANOVA, S.; PEREZ, C. A.; SCHMAL, M.; BUENO, J. M. C. Characterization of ceria-coated alumina carrier. **Applied Catalysis A: General**, v. 234, n. 1–2, p. 271–282, 2002.

- DE CARVALHO, T. P.; CATAPAN, R. C.; OLIVEIRA, A. A. M.; VLACHOS, D. G. Microkinetic Modeling and Reduced Rate Expression of the Water-Gas Shift Reaction on Nickel. **Industrial and Engineering Chemistry Research**, v. 57, n. 31, p. 10269–10280, 2018.
- DE LA OSA, A. R.; DE LUCAS, A.; ROMERO, A.; VALVERDE, J. L.; SÁNCHEZ, P. Kinetic models discrimination for the high pressure WGS reaction over a commercial CoMo catalyst. **International Journal of Hydrogen Energy**, v. 36, n. 16, p. 9673–9684, 2011.
- DE QUEIROZ, G. A.; DE MENEZES BARBOSA, C. M. B.; DE ABREU, C. A. M. Mechanism-based kinetics of the water–gas shift reaction at low temperature with a ruthenium catalysts. **Reaction Kinetics, Mechanisms and Catalysis**, v. 123, n. 2, p. 573–583, 2018.
- DEVOCHT, B. R.; THYBAUT, J. W.; TOCH, K.; OYAMA, S. T.; MARIN, G. B.; KAGEYAMA, N.; TOCH, K.; OYAMA, S. T.; MARIN, G. B. Balance between model detail and experimental information in steam methane reforming over a Ni/MgO-SiO₂ catalyst. **AIChE Journal**, v. 65, n. 4, p. 1222–1233, 2019.
- DONGIL, A. B.; PASTOR-PÉREZ, L.; ESCALONA, N.; SEPÚLVEDA-ESCRIBANO, A. Carbon nanotube-supported Ni-CeO₂ catalysts. Effect of the support on the catalytic performance in the low-temperature WGS reaction. **Carbon**, v. 101, p. 296–304, 2016.
- DUMESIC, J. A.; RUDD, D. F.; APARICIO, L. M.; REKOSKE, J. E.; TREVIÑO, A. A. **The Microkinetics of Heterogeneous Catalysis**. 1st. ed. Washington, DC, USA: American Chemical Society, 1993.
- ECONOMICS, T. **Cobalt 2010-2021 Data | 2022-2023 Forecast | Price | Quote | Chart | Historical**. Disponível em: <<https://tradingeconomics.com/commodity/cobalt>>.
- FIGUEIRA, C. E.; MOREIRA, P. F.; GIUDICI, R.; ALVES, R. M. B.; SCHMAL, M. Nanoparticles of Ce, Sr, Co in and out the multi-walled carbon nanotubes applied for dry reforming of methane. **Applied Catalysis A: General**, v. 550, n. December, p. 297–307, 2018. Disponível em: <<https://doi.org/10.1016/j.apcata.2017.11.019>>.
- FROMENT, G. F.; BISCHOFF, K. B.; WILDE, J. De. **Chemical Reactor Analysis and Design**. 3rd. ed. Hoboken, USA: John Wiley & Sons, Inc., 2011. 860 p.
- GHANEKAR, P.; KUBAL, J.; CUI, Y.; MITCHELL, G.; DELGASS, W. N.; RIBEIRO, F.; GREELEY, J. Catalysis at Metal/Oxide Interfaces: Density Functional Theory and Microkinetic Modeling of Water Gas Shift at Pt/MgO Boundaries. **Topics in Catalysis**, v. 63, n. 7–8, p. 673–687, 1 ago. 2020.

- GHASEMZADEH, K.; AGHAEINEJAD-MEYBODI, A.; BASILE, A. Hydrogen production as a green fuel in silica membrane reactor: Experimental analysis and artificial neural network modeling. **Fuel**, v. 222, n. October 2017, p. 114–124, 2018.
- GOKHALE, A. A.; DUMESIC, J. A.; MAVRIKAKIS, M. On the mechanism of low-temperature water gas shift reaction on copper. **Journal of the American Chemical Society**, v. 130, n. 4, p. 1402–1414, 2008.
- GRADISHER, L.; DUTCHER, B.; FAN, M. Catalytic hydrogen production from fossil fuels via the water gas shift reaction. **Applied Energy**, v. 139, p. 335–349, 2015.
- GÜNAY, M. E.; YILDIRIM, R. Neural network Analysis of Selective CO Oxidation over Copper-Based Catalysts for Knowledge Extraction from Published Data in the Literature. **Industrial & Engineering Chemistry Research**, v. 50, n. 22, p. 12488–12500, 2011.
- GÜNAY, M. E.; YILDIRIM, R. Developing global reaction rate model for CO oxidation over Au catalysts from past data in literature using artificial neural networks. **Applied Catalysis A: General**, v. 468, p. 395–402, 2013.
- GÜNTHER, F.; FRITSCH, S. neuralnet: Training of Neural Networks. **The R Journal**, v. 2, n. 1, p. 30–38, 2010.
- HLA, S. S.; DUFFY, G. J.; MORPETH, L. D.; COUSINS, A.; ROBERTS, D. G.; EDWARDS, J. H. Investigation into the performance of a Co-Mo based sour shift catalyst using simulated coal-derived syngases. **International Journal of Hydrogen Energy**, v. 36, n. 11, p. 6638–6645, 2011a.
- HLA, S. S.; DUFFY, G. J.; MORPETH, L. D.; COUSINS, A.; ROBERTS, D. G.; EDWARDS, J. H. Investigation into the performance of a Co-Mo based sour shift catalyst using simulated coal-derived syngases. **International Journal of Hydrogen Energy**, v. 36, n. 11, p. 6638–6645, 2011b.
- HOLEŇA, M.; BAERNS, M. Feedforward neural networks in catalysis: A tool for the approximation of the dependency of yield on catalyst composition, and for knowledge extraction. **Catalysis Today**, v. 81, n. 3, p. 485–494, 2003.
- HOUSTON, R.; LABBÉ, N.; HAYES, D.; DAW, C. S.; ABDOULMOUMINE, N. Intermediate temperature water-gas shift kinetics for hydrogen production. **Reaction Chemistry and Engineering**, v. 4, n. 10, p. 1814–1822, 2019.
- HUTCHINGS, G. J.; COPPERTHWAITET, R. G.; GOTTSCHALK, F. M.; HUNTER, R.; MELLOR, J.; ORCHARD, S. W.; SANGIORGIO, T. A comparative evaluation of cobalt

chromium oxide, cobalt manganese oxide, and copper manganese oxide as catalysts for the water-gas shift reaction. **Journal of Catalysis**, v. 137, n. 2, p. 408–422, 1992.

INTERNATIONAL ENERGY AGENCY. **The Future of Hydrogen - Seizing today's opportunities (Report)**. [s.l.: s.n.].

JAIN, R.; POYRAZ, A. S.; GAMLIEL, D. P.; VALLA, J.; SUIB, S. L.; MARIC, R. Comparative study for low temperature water-gas shift reaction on Pt/ceria catalysts: Role of different ceria supports. **Applied Catalysis A: General**, v. 507, p. 1–13, 2015.

JEONG, D. W.; JANG, W. J.; SHIM, J. O.; HAN, W. B.; KIM, H. M.; LEE, Y. L.; BAE, J. W.; ROH, H. S. Optimization of a highly active nano-sized Pt/CeO₂ catalyst via Ce(OH)CO₃ for the water-gas shift reaction. **Renewable Energy**, v. 79, n. 1, p. 78–84, 2015.

KARACI, A.; CAGLAR, A.; AYDINLI, B.; PEKOL, S. The pyrolysis process verification of hydrogen rich gas (H-rG) production by artificial neural network (ANN). **International Journal of Hydrogen Energy**, v. 41, n. 8, p. 4570–4578, 2016.

KENNEDY, J.; EBERHART, R. Particle swarm optimization. Em: Proceedings of ICNN'95 - International Conference on Neural Networks, 1995, Perth, Australia. [...]. Perth, Australia: 1995. v. 4, p. 1942–1948.

KOBAYASHI, Y.; OMATA, K.; YAMADA, M. Screening of additives to a Co/SrCO₃ catalyst for preferential oxidation of CO in excess hydrogen. **Catalysis Communications**, v. 8, n. 1, p. 1–5, 2010.

KOZONOE, C. E.; BRITO, R. M.; SCHMAL, M. Influence of feed rate and testing variables for low-temperature tri-reforming of methane on the Ni@MWCNT/Ce catalyst. **Fuel**, v. 281, n. July, p. 118749, 2020. Disponível em: <<https://doi.org/10.1016/j.fuel.2020.118749>>.

KOZONOE, C. E.; DE PAIVA FLORO BONFIM, R.; BRITO ALVES, R. M.; SCHMAL, M. The Fe-Co-Cu supported on MWCNT as catalyst for the tri-reforming of methane – Investigating the structure changes of the catalysts. **Fuel**, v. 256, n. April, 2019.

LEE, D. W.; LEE, M. S.; LEE, J. Y.; KIM, S.; EOM, H. J.; MOON, D. J.; LEE, K. Y. The review of Cr-free Fe-based catalysts for high-temperature water-gas shift reactions. **Catalysis Today**, v. 210, p. 2–9, 2013. Disponível em: <<http://dx.doi.org/10.1016/j.cattod.2012.12.012>>.

LEE, Y. L.; KIM, K. J.; HONG, G. R.; ROH, H. S. **Target-oriented water–gas shift reactions with customized reaction conditions and catalysts** *Chemical Engineering Journal* Elsevier B.V., 15 fev. 2023.

LEHMAN, J. H.; TERRONES, M.; MEUNIER, V.; MANSFIELD, E.; HURST, K. E.; MEUNIER, V. Evaluating the characteristics of multiwall carbon nanotubes. *Carbon*, v. 49, n. 8, p. 2581–2602, 2011.

LEVALLEY, T. L.; RICHARD, A. R.; FAN, M. The progress in water gas shift and steam reforming hydrogen production technologies - A review. *International Journal of Hydrogen Energy*, v. 39, n. 30, p. 16983–17000, 2014.

LI, Y.; QIU, W.; QIN, F.; FANG, H.; HADJIEV, V. G.; LITVINOV, D.; BAO, J. Identification of Cobalt Oxides with Raman Scattering and Fourier Transform Infrared Spectroscopy. *Journal of Physical Chemistry C*, v. 120, n. 8, p. 4511–4516, 2016.

LI, Z.; WANG, M.; JIA, Y.; DU, R.; LI, T.; ZHENG, Y.; CHEN, M.; QIU, Y.; YAN, K.; ZHAO, W.-W.; WANG, P.; WATERHOUSE, G. I. N.; DAI, S.; ZHAO, Y.; CHEN, G. CeO₂/Cu₂O/Cu Tandem Interfaces for Efficient Water–Gas Shift Reaction Catalysis. *ACS Applied Materials & Interfaces*, v. 15, n. 26, p. 31584–31594, 5 jul. 2023. Disponível em: <<https://doi.org/10.1021/acsami.3c06386>>.

LIANG, S.; VESER, G. Mixed lanthana/ceria nanorod-supported gold catalysts for water-gas-shift. *Catalysis Letters*, v. 142, n. 8, p. 936–945, 2012.

LIMA, D. F. B.; ZANELLA, F. A.; LENZI, M. K.; NDIAYE, P. M. Modeling and Simulation of Water Gas Shift Reactor : An Industrial Case. *Petrochemicals*, n. May 2014, p. 53–74, 2012.

LIU, K.; SONG, C.; SUBRAMANI, V. **Hydrogen and Syngas Production and Purification Technologies**. [s.l: s.n.]1–533 p.

LOOS, M. R. **NANOCIÊNCIA E NANOTECNOLOGIA: Compósitos Termofixos Reforçados com Nanotubos de Carbono**. Rio de Janeiro: Editora Interciência, 2014.

LUO, W.; CHEN, Y.; DU, Z.; CHEN, C. Theoretical Study on PdCu/CeO₂ - Catalyzed Water – Gas Shift Reaction : Crucial Role of the Metal/Ceria Interface and O₂ Enhancement Effects. *The Journal of Physical Chemistry C*, v. 122, n. 3, p. 28868–28883, 2018.

MADON, R. J.; BRADEN, D.; KANDOI, S.; NAGEL, P.; MAVRIKAKIS, M.; DUMESIC, J. A. Microkinetic analysis and mechanism of the water gas shift reaction over copper catalysts. *Journal of Catalysis*, v. 281, n. 1, p. 1–11, 2011.

- MAESTRI, M.; CUOCI, A. Coupling CFD with detailed microkinetic modeling in heterogeneous catalysis. **Chemical Engineering Science**, v. 96, p. 106–117, 2013.
- MAESTRI, M.; VLACHOS, D. G.; BERETTA, A.; GROPPPI, G.; TRONCONI, E. Steam and dry reforming of methane on Rh: Microkinetic analysis and hierarchy of kinetic models. **Journal of Catalysis**, v. 259, n. 2, p. 211–222, 2008.
- MAESTRI, M.; VLACHOS, D. G.; BERETTA, A.; GROPPPI, G.; TRONCONI, E. A C1 Microkinetic Model for Methane Conversion to Syngas on Rh/Al₂O₃. **AIChE Journal**, v. 55, n. 4, p. 993–1008, 2009.
- MARIN, G. B.; YABLONSKY, G. S.; CONSTALES, D. **Kinetics of chemical reactions: decoding complexity**. 2nd. ed. Weinheim, Germany: Wiley-VCH, 2011. 428 p.
- MARQUARDT, D. W. An algorithm for Least-Squares Estimation of Nonlinear Parameters. **Journal of the Society for Industrial and Applied Mathematics**, v. 11, n. 2, p. 431–441, 1963.
- MATERIALS DATA. **JADE**. Disponível em: <<https://materialsdata.com/index.html>>. Acesso em: 1 ago. 2020.
- MEARS, D. E. Diagnostic criteria for heat transport limitations in fixed bed reactors. **Journal of Catalysis**, v. 20, n. 2, p. 127–131, 1971.
- MELCHIONNA, M.; MARCHESAN, S.; PRATO, M.; FORNASIERO, P. Carbon nanotubes and catalysis: the many facets of a successful marriage. **Catalysis Science & Technology**, v. 5, n. 8, p. 3859–3875, 2015.
- MENDES, D.; MENDES, A.; MADEIRA, L. M.; IULIANELLI, A.; SOUSA, J. M.; BASILE, A. The water-gas shift reaction: from conventional catalytic systems to Pd-based membrane reactors-a review. **Asia-Pacific Journal of Chemical Engineering**, v. 5, n. 1, p. 111–137, jan. 2010.
- MENG, Y.; CHEN, Y.; ZHOU, X.; PAN, G.; XIA, S. Experimental and theoretical investigations into the activity and mechanism of the water–gas shift reaction catalyzed by Au nanoparticles supported on Zn–Al/Cr/Fe layered double hydroxides. **International Journal of Hydrogen Energy**, v. 45, n. 1, p. 464–476, 1 jan. 2020. . Acesso em: 14 fev. 2024.
- MHADESHWAR, A. B.; VLACHOS, D. G. Is the water-gas shift reaction on Pt simple? Computer-aided microkinetic model reduction, lumped rate expression, and rate-determining step. **Catalysis Today**, v. 105, n. 1 SPEC. ISS., p. 162–172, 2005.

MITCHELL, G. M.; SABNIS, K. D.; SOLLBERGER, F. G.; CUI, Y.; HAN, C. W.; MAJUMDAR, P.; ZENG, Z.; MILLER, J. T.; GREELEY, J.; ORTALAN, V.; WANG, C.; DELGASS, W. N.; RIBEIRO, F. H. Effect of cobalt addition on platinum supported on multi-walled carbon nanotubes for water-gas shift. **Journal of Catalysis**, v. 391, p. 25–34, 2020. Disponível em: <<https://doi.org/10.1016/j.jcat.2020.07.028>>.

NAGAI, M.; ZAHIDUL, A. M.; KUNISAKI, Y.; AOKI, Y. Water-gas shift reactions on potassium- and zirconium-promoted cobalt molybdenum carbide catalysts. **Applied Catalysis A: General**, v. 383, n. 1–2, p. 58–65, 2010.

NASCIMENTO, C. A. O.; GIUDICI, R. Neural network based approach for optimisation applied to an industrial nylon-6,6 polymerisation process. **Computers & Chemical Engineering**, v. 22, p. 595–600, 1998.

NEWSOME, D. S. The Water-Gas Shift Reaction. **Catalysis Reviews**, v. 21, n. 2, p. 275–318, 5 jan. 1980.

ODABAŞI, Ç.; GÜNAY, M. E.; YILDIRIM, R. Knowledge extraction for water gas shift reaction over noble metal catalysts from publications in the literature between 2002 and 2012. **International Journal of Hydrogen Energy**, v. 39, n. 11, p. 5733–5746, 2014.

OLIVEIRA, H. A.; FRANCESCHINI, D. F.; PASSOS, F. B. Cobalt catalyst characterization for methane decomposition and carbon nanotube growth. **Journal of the Brazilian Chemical Society**, v. 25, n. 12, p. 2339–2349, 1 dez. 2014.

OSSWALD, S.; HAVEL, M.; GOGOTSI, Y. Monitoring oxidation of multiwalled carbon nanotubes by Raman spectroscopy. **Journal of Raman Spectroscopy**, v. 38, n. May, p. 728–736, 2007.

PAL, D. B.; CHAND, R.; UPADHYAY, S. N.; MISHRA, P. K. Performance of water gas shift reaction catalysts: A review. **Renewable and Sustainable Energy Reviews**, v. 93, n. December 2017, p. 549–565, 2018. Disponível em: <<https://doi.org/10.1016/j.rser.2018.05.003>>.

PANTOLEONTOS, G.; KIKKINIDES, E. S.; GEORGIADIS, M. C. A heterogeneous dynamic model for the simulation and optimisation of the steam methane reforming reactor. **International Journal of Hydrogen Energy**, v. 37, n. 21, p. 16346–16358, 2012.

PARK, T. Y.; FROMENT, G. F. A hybrid genetic algorithm for the estimation of parameters in detailed kinetic models. **Computers and Chemical Engineering**, v. 22, n. SUPPL.1, 1998.

- PASTOR-PÉREZ, L.; BUITRAGO-SIERRA, R.; SEPÚLVEDA-ESCRIBANO, A. CeO₂-promoted Ni/activated carbon catalysts for the water-gas shift (WGS) reaction. **International Journal of Hydrogen Energy**, v. 39, n. 31, p. 17589–17599, 2014.
- PATTERSON, A. L. The scherrer formula for X-ray particle size determination. **Physical Review**, v. 56, n. 10, p. 978–982, 1939.
- PENG, Y.; LIU, H. Effects of oxidation by hydrogen peroxide on the structures of multiwalled carbon nanotubes. **Industrial and Engineering Chemistry Research**, v. 45, n. 19, p. 6483–6488, 2006.
- PERLINGEIRO, C. A. G. **Engenharia de Processos: Análise, Simulação, Otimização e Síntese de Processos Químicos**. 1st. ed. São Paulo: Editora Blucher, 2005.
- POISSONNIER, J.; PELCKMANS, M.; VAN WAES, F.; MOONEN, K.; SELS, B. F.; THYBAUT, J. W.; MARIN, G. B. Kinetics of homogeneous and heterogeneous reactions in the reductive aminolysis of glucose with dimethylamine. **Applied Catalysis B: Environmental**, v. 227, n. April 2019, p. 161–169, 2018.
- POTDAR, H. S.; JEONG, D. W.; KIM, K. S.; ROH, H. S. Synthesis of highly active nano-sized Pt/CeO₂ catalyst via a cerium hydroxy carbonate precursor for water gas shift reaction. **Catalysis Letters**, v. 141, n. 9, p. 1268–1274, 2011.
- RABEE, A. I. M.; GAID, C. B. A.; MEKHEMER, G. A. H.; ZAKI, M. I. Combined TPR, XRD, and FTIR studies on the reduction behavior of Co₃O₄. **Materials Chemistry and Physics**, v. 289, p. 126367, 15 set. 2022. . Acesso em: 13 fev. 2024.
- RATNASAMY, C.; WAGNER, J. P. Water Gas Shift Catalysis. **Cat. Rev.**, v. 51, n. 3, p. 325–440, 2009.
- REDDY, G. K.; SMIRNIOTIS, P. G. **Water Gas Shift Reaction Research Developments and Applications**. 1st. ed. Waltham/USA: Elsevier, 2015.
- RHODES, C. N.; WILLIAMS, B. P.; KING, F.; HUTCHINGS, G. J. Promotion of Fe₃O₄/Cr₂O₃ High Temperature Water Gas Shift Catalyst. **Catalysis Communications**, v. 3, n. 8, p. 381–384, 2002.
- RIBEIRO, B.; BOTELHO, E. C.; COSTA, M. L.; BANDEIRA, C. F. Carbon nanotube buckypaper reinforced polymer composites: a review. **Polímeros**, v. 27, n. 3, p. 247–255, 2017.
- RODRIGUEZ, J. A. Gold-based catalysts for the water-gas shift reaction: Active sites and reaction mechanism. **Catalysis Today**, v. 160, n. 1, p. 3–10, 2011.

ROTHENBERG, G. Data mining in catalysis: Separating knowledge from garbage. **Catalysis Today**, v. 137, n. 1, p. 2–10, 2008.

SAEIDI, S.; FAZLOLLAHI, F.; NAJARI, S.; IRANSHAHI, D.; KLEMEŠ, J. J.; BAXTER, L. L. Hydrogen production: Perspectives, separation with special emphasis on kinetics of WGS reaction: A state-of-the-art review. **Journal of Industrial and Engineering Chemistry**, v. 49, p. 1–25, 2017.

SAW, S. Z.; NANDONG, J.; GHOSH, U. K. Comparative Study of Homogeneous and Heterogeneous Modelling of Water-Gas Shift Reaction with Macro-or Micro-kinetics. **Procedia Engineering**, v. 148, p. 949–956, 2016.

SCHMAL, M. **Heterogeneous Catalysis and its Industrial Applications**. 1st. ed. Switzerland: Springer, 2016.

SCHMAL, M.; TONIOLO, F. S.; KOZONOE, C. E. Perspective of catalysts for (Tri) reforming of natural gas and flue gas rich in CO₂. **Applied Catalysis A: General**, v. 568, p. 23–42, 25 nov. 2018.

SCHWAAB, M.; BISCAIA, E. C.; MONTEIRO, J. L.; PINTO, J. C. Nonlinear parameter estimation through particle swarm optimization. **Chemical Engineering Science**, v. 63, n. 6, p. 1542–1552, 2008.

SCHWAAB, M.; PINTO, J. C. Optimum reference temperature for reparameterization of the Arrhenius equation. Part 1: Problems involving one kinetic constant. **Chemical Engineering Science**, v. 62, n. 10, p. 2750–2764, 2007a.

SCHWAAB, M.; PINTO, J. C. **Análise de Dados Experimentais I**. 1st. ed. Rio de Janeiro: e-papers, 2007b.

SCHWAAB, M.; PINTO, J. C. **Análise de Dados Experimentais II - Planejamento de Experimentos**. 1st. ed. Rio de Janeiro: e-papers, 2011.

ŞENER, A. N.; GÜNAY, M. E.; LEBA, A.; YILDIRIM, R. Statistical review of dry reforming of methane literature using decision tree and artificial neural network analysis. **Catalysis Today**, v. 299, n. May 2017, p. 289–302, 2018.

SERP, P.; CORRIAS, M.; KALCK, P. Carbon nanotubes and nanofibers in catalysis. **Applied Catalysis A: General**, v. 253, n. 2, p. 337–358, 2003.

SERRA, J. M.; CORMA, A.; CHICA, A.; ARGENTE, E.; BOTTI, V. Can artificial neural networks help the experimentation in catalysis? **Catalysis Today**, v. 81, n. 3, p. 393–403, 2003.

SHANAHAN, A. E.; SULLIVAN, J. A.; MCNAMARA, M.; BYRNE, H. J. Preparation and characterization of a composite of gold nanoparticles and single-walled carbon

nanotubes and its potential for heterogeneous catalysis. **Xinxing Tan Cailiao/New Carbon Materials**, v. 26, n. 5, p. 347–355, 2011.

SMITH, A.; KEANE, A.; DUMESIC, J. A.; HUBER, G. W.; ZAVALA, V. M. A machine learning framework for the analysis and prediction of catalytic activity from experimental data. **Applied Catalysis B: Environmental**, v. 263, 1 abr. 2020.

SMITH R J, B.; LOGANATHAN, M.; SHANTHA, M. S. A Review of the Water Gas Shift Reaction Kinetics. **International Journal of Chemical Reactor Engineering**, v. 8, n. 1, p. 1–32, 2010.

SPRUNG, C.; KECHAGIOPOULOS, P. N.; THYBAUT, J. W.; ARSTAD, B.; OLSBYE, U.; MARIN, G. B. Microkinetic evaluation of normal and inverse kinetic isotope effects during methane steam reforming to synthesis gas over a Ni/NiAl₂O₄ model catalyst. **Applied Catalysis A: General**, v. 492, p. 231–242, 2015. Disponível em: <<http://dx.doi.org/10.1016/j.apcata.2014.10.062>>.

SUN, J.; THYBAUT, J. W.; MARIN, G. B. Microkinetics of methane oxidative coupling. v. 137, p. 90–102, 2008.

TESSONNIER, J.-P.; ERSEN, O.; WEINBERG, G.; PHAM-HUU, C.; SU, D. S.; SCHLÖGL, R. Selective deposition of metal nanoparticles inside or outside multiwalled carbon nanotubes. **ACS nano**, v. 3, n. 8, p. 2081–2089, 2009.

THOMMES, M.; KANEKO, K.; NEIMARK, A. V.; OLIVIER, J. P.; RODRIGUEZ-REINOSO, F.; ROUQUEROL, J.; SING, K. S. W. Physisorption of gases, with special reference to the evaluation of surface area and pore size distribution (IUPAC Technical Report). **Pure and Applied Chemistry**, v. 87, n. 9–10, p. 1051–1069, 2015.

THYBAUT, J. W.; SAEYS, M.; MARIN, G. B. Hydrogenation kinetics of toluene on Pt/ZSM-22. **Chemical Engineering Journal**, v. 90, n. 1–2, p. 117–129, 2002.

THYBAUT, J. W.; SUN, J.; OLIVIER, L.; VAN VEEN, A. C.; MIRODATOS, C.; MARIN, G. B. Catalyst design based on microkinetic models: Oxidative coupling of methane. **Catalysis Today**, v. 159, n. 1, p. 29–36, 2011.

TOCH, K. **An Intrinsic Kinetics Based Methodology for Multi-Scale Modeling of Chemical Reactions (PhD Thesis)**. 2015. Universiteit Gent, 2015.

TOCH, K.; THYBAUT, J. W.; MARIN, G. B. A Systematic Methodology for Kinetic Modeling of Chemical Reactions Applied to n-Hexane Hydroisomerization. **AIChE Journal**, v. 61, n. 3, p. 1–13, 2014.

VIRTANEN, P.; GOMMERS, R.; OLIPHANT, T. E.; HABERLAND, M.; REDDY, T.; COURNAPEAU, D.; BUROVSKI, E.; PETERSON, P.; WECKESSER, W.; BRIGHT, J.;

VAN DER WALT, S. J.; BRETT, M.; WILSON, J.; MILLMAN, K. J.; MAYOROV, N.; NELSON, A. R. J.; JONES, E.; KERN, R.; LARSON, E.; CAREY, C. J.; POLAT, İ.; FENG, Y.; MOORE, E. W.; VANDERPLAS, J.; LAXALDE, D.; PERKTOLD, J.; CIMRMAN, R.; HENRIKSEN, I.; QUINTERO, E. A.; HARRIS, C. R.; ARCHIBALD, A. M.; RIBEIRO, A. H.; PEDREGOSA, F.; VAN MULBREGT, P.; VIJAYKUMAR, A.; BARDELLI, A. Pietro; ROTHBERG, A.; HILBOLL, A.; KLOECKNER, A.; SCOPATZ, A.; LEE, A.; ROKEM, A.; WOODS, C. N.; FULTON, C.; MASSON, C.; HÄGGSTRÖM, C.; FITZGERALD, C.; NICHOLSON, D. A.; HAGEN, D. R.; PASECHNIK, D. V.; OLIVETTI, E.; MARTIN, E.; WIESER, E.; SILVA, F.; LENDERS, F.; WILHELM, F.; YOUNG, G.; PRICE, G. A.; INGOLD, G. L.; ALLEN, G. E.; LEE, G. R.; AUDREN, H.; PROBST, I.; DIETRICH, J. P.; SILTERRA, J.; WEBBER, J. T.; SLAVIČ, J.; NOTHMAN, J.; BUCHNER, J.; KULICK, J.; SCHÖNBERGER, J. L.; DE MIRANDA CARDOSO, J. V.; REIMER, J.; HARRINGTON, J.; RODRÍGUEZ, J. L. C.; NUNEZ-IGLESIAS, J.; KUCZYNSKI, J.; TRITZ, K.; THOMA, M.; NEWVILLE, M.; KÜMMERER, M.; BOLINGBROKE, M.; TARTRE, M.; PAK, M.; SMITH, N. J.; NOWACZYK, N.; SHEBANOV, N.; PAVLYK, O.; BRODTKORB, P. A.; LEE, P.; MCGIBBON, R. T.; FELDBAUER, R.; LEWIS, S.; TYGIER, S.; SIEVERT, S.; VIGNA, S.; PETERSON, S.; MORE, S.; PUDLIK, T.; OSHIMA, T.; PINGEL, T. J.; ROBITAILLE, T. P.; SPURA, T.; JONES, T. R.; CERA, T.; LESLIE, T.; ZITO, T.; KRAUSS, T.; UPADHYAY, U.; HALCHENKO, Y. O.; VÁZQUEZ-BAEZA, Y. SciPy 1.0: fundamental algorithms for scientific computing in Python. **Nature Methods**, v. 17, n. 3, p. 261–272, 2020.

WANG, X.; GORTE, R. J.; WAGNER, J. P. Deactivation mechanisms for Pd/ceria during the water-gas-shift reaction. **Journal of Catalysis**, v. 212, n. 2, p. 225–230, 2002.

YAGHOBI, N. The role of gas hourly space velocity and feed composition for catalytic oxidative coupling of methane: Experimental study. **Journal of King Saud University - Engineering Sciences**, v. 25, n. 1, p. 1–10, 2013.

ZAMANIYAN, A.; JODA, F.; BEHROOZSARAND, A.; EBRAHIMI, H. Application of artificial neural networks (ANN) for modeling of industrial hydrogen plant. **International Journal of Hydrogen Energy**, v. 38, n. 15, p. 6289–6297, 2013.

ZAVYALOVA, U.; HOLENA, M.; SCHLÖGL, R.; BAERNS, M. Statistical analysis of past catalytic data on oxidative methane coupling for new insights into the composition of high-performance catalysts. **ChemCatChem**, v. 3, n. 12, p. 1935–1947, 2011.

- ZHANG, M.; WANG, M.; XU, B.; MA, D. How to Measure the Reaction Performance of Heterogeneous Catalytic Reactions Reliably. **Joule**, v. 3, n. 12, p. 2876–2883, 2019.
- ZHANG, Y.; CHEN, C.; LIN, X.; LI, D.; CHEN, X.; ZHAN, Y.; ZHENG, Q. CuO/ZrO₂ catalysts for water-gas shift reaction: Nature of catalytically active copper species. **International Journal of Hydrogen Energy**, v. 39, n. 8, p. 3746–3754, 2014.
- ZHAO, H.; HU, Y.; LI, J. Reduced rate method for discrimination of the kinetic models for the water – gas shift reaction. 1999.
- ZHAO, Z. J.; LI, Z.; CUI, Y.; ZHU, H.; SCHNEIDER, W. F.; DELGASS, W. N.; RIBEIRO, F.; GREELEY, J. Importance of metal-oxide interfaces in heterogeneous catalysis: A combined DFT, microkinetic, and experimental study of water-gas shift on Au/MgO. **Journal of Catalysis**, v. 345, p. 157–169, 2017.
- ZHOU, L.; LIU, Y.; LIU, S.; ZHANG, H.; WU, X.; SHEN, R.; LIU, T.; GAO, J.; SUN, K.; LI, B.; JIANG, J. For more and purer hydrogen-the progress and challenges in water gas shift reaction. **Journal of Energy Chemistry**, v. 83, p. 363–396, ago. 2023. Disponível em: <<https://linkinghub.elsevier.com/retrieve/pii/S2095495623002206>>.
- ZHU, M.; WACHS, I. E. Resolving the Reaction Mechanism for H₂ Formation from High-Temperature Water-Gas Shift by Chromium-Iron Oxide Catalysts. **ACS Catalysis**, v. 6, n. 5, p. 2827–2830, 2016.
- ZUGIC, B.; BELL, D. C.; FLYTZANI-STEPHANOPOULOS, M. Activation of carbon-supported platinum catalysts by sodium for the low-temperature water-gas shift reaction. **Applied Catalysis B: Environmental**, v. 144, n. 1, p. 243–251, 2014.

APPENDIX A – DATABASE FOR ANN MODEL

The database used to build the ANN model is available at: <https://ars.els-cdn.com/content/image/1-s2.0-S0301479719302439-mmc2.xlsx>

APPENDIX B – ANN WEIGHTS

Table B.1 exhibits the estimated weight values of the developed ANN represented in Figure 3.8.

Table B.1 – Estimated weights of the developed ANN

Weight	Value
Intercept.to.1layhid1	-0.142034951
Temperature.to.1layhid1	16.21249168
Pressure.to.1layhid1	-1.948047916
Catalyst.Mass.to.1layhid1	4.159665538
GSHV.to.1layhid1	5.19060862
Specifc.Area.BET.to.1layhid1	-0.730298703
Calcination.Temperature.to.1layhid1	1.192254139
Calcination.Time.to.1layhid1	1.164595308
CO.to.1layhid1	-8.398235332
H2O.to.1layhid1	-0.571468492
CO2.to.1layhid1	-0.68168954
H2.to.1layhid1	-7.737595795
N2.to.1layhid1	9.557840518
He.to.1layhid1	-0.573124927
CH4.to.1layhid1	-7.646201927
Fe2O3.to.1layhid1	0.161734648
AC.to.1layhid1	1.973008733
CNT.to.1layhid1	2.425532348
Mo2C.to.1layhid1	0.621106319
CeO2.to.1layhid1	-0.553566414
La2O3.to.1layhid1	-4.84990885
ZrO2.to.1layhid1	-3.268432014
MgO.to.1layhid1	-445.3008863
Al2O3.to.1layhid1	-1.55181453
TiO2.to.1layhid1	-0.966841336
Co.to.1layhid1	-7.194662998
Ni.to.1layhid1	-120.8313239
Cu.to.1layhid1	-4.970889244
Ru.to.1layhid1	0.279002643
Pd.to.1layhid1	-12.74077839
Ag.to.1layhid1	-1.758610372
Ir.to.1layhid1	0.196746413
Pt.to.1layhid1	-3.647036563
Au.to.1layhid1	16.96977588
Cr.to.1layhid1	-21.54656135
Zn.to.1layhid1	-0.133744012
Na.to.1layhid1	37.85724915
K.to.1layhid1	-4.452523307

Weight	Value
Mg.to.1layhid1	-0.259653327
Ba.to.1layhid1	-338.2133712
B.to.1layhid1	1.375249895
Al.to.1layhid1	-0.192281105
Si.to.1layhid1	0.043714625
Pb.to.1layhid1	-63.71912325
S.to.1layhid1	-2.770034174
Hg.to.1layhid1	0.029806387
Y.to.1layhid1	31.19950196
Ti.to.1layhid1	-0.352898239
Zr.to.1layhid1	13.33255742
La.to.1layhid1	9.283683637
Ce.to.1layhid1	0.652484364
Fe.to.1layhid1	16.0286989
Intercept.to.1layhid2	0.065326744
Temperature.to.1layhid2	2.406108978
Pressure.to.1layhid2	-0.915418902
Catalyst.Mass.to.1layhid2	-0.437394411
GSHV.to.1layhid2	-2.489268026
Specifc.Area.BET.to.1layhid2	5.526628271
Calcination.Temperature.to.1layhid2	0.210228139
Calcination.Time.to.1layhid2	-1.030150719
CO.to.1layhid2	-1.151078442
H2O.to.1layhid2	1.692690133
CO2.to.1layhid2	1.348283503
H2.to.1layhid2	-2.240772588
N2.to.1layhid2	1.755746144
He.to.1layhid2	-7.587289547
CH4.to.1layhid2	-2.290043606
Fe2O3.to.1layhid2	-4.548765622
AC.to.1layhid2	-88.38353055
CNT.to.1layhid2	16.21415019
Mo2C.to.1layhid2	-0.656494317
CeO2.to.1layhid2	-0.342021077
La2O3.to.1layhid2	25.49364411
ZrO2.to.1layhid2	0.233943736
MgO.to.1layhid2	-1.074470546
Al2O3.to.1layhid2	-0.551638822
TiO2.to.1layhid2	-0.605469359
Co.to.1layhid2	0.02220382
Ni.to.1layhid2	1.547341873
Cu.to.1layhid2	0.399061144
Ru.to.1layhid2	1.048817147
Pd.to.1layhid2	-0.13160744
Ag.to.1layhid2	-1.406229188
Ir.to.1layhid2	70.3132861
Pt.to.1layhid2	-212.6592643

Weight	Value
Au.to.1layhid2	-8.942845844
Cr.to.1layhid2	-1.127452423
Zn.to.1layhid2	-0.212057175
Na.to.1layhid2	28.60434631
K.to.1layhid2	-1.218861359
Mg.to.1layhid2	-0.010263896
Ba.to.1layhid2	3.240173661
B.to.1layhid2	0.420324916
Al.to.1layhid2	-0.395093207
Si.to.1layhid2	-0.174983964
Pb.to.1layhid2	3.020170297
S.to.1layhid2	0.585319607
Hg.to.1layhid2	-1.96087424
Y.to.1layhid2	-0.025512801
Ti.to.1layhid2	0.235146635
Zr.to.1layhid2	-0.26592617
La.to.1layhid2	-342.2183743
Ce.to.1layhid2	-464.6034643
Fe.to.1layhid2	-1.46482605
Intercept.to.1layhid3	-0.107137604
Temperature.to.1layhid3	-5.806389711
Pressure.to.1layhid3	-1.414143012
Catalyst.Mass.to.1layhid3	-11.32108246
GSHV.to.1layhid3	4.138205751
Specifc.Area.BET.to.1layhid3	0.262302112
Calcination.Temperature.to.1layhid3	-0.043809702
Calcination.Time.to.1layhid3	-4.419379052
CO.to.1layhid3	-0.213850558
H2O.to.1layhid3	-1.069424047
CO2.to.1layhid3	4.07431733
H2.to.1layhid3	1.785843572
N2.to.1layhid3	0.454399475
He.to.1layhid3	3.059787824
CH4.to.1layhid3	2.401357628
Fe2O3.to.1layhid3	0.204247094
AC.to.1layhid3	-88.63258859
CNT.to.1layhid3	-0.096084577
Mo2C.to.1layhid3	-0.485456503
CeO2.to.1layhid3	-0.836330614
La2O3.to.1layhid3	0.596534493
ZrO2.to.1layhid3	2.503096316
MgO.to.1layhid3	-1.015283072
Al2O3.to.1layhid3	1.112677008
TiO2.to.1layhid3	1.218237356
Co.to.1layhid3	-1.085136638
Ni.to.1layhid3	-110.5687204
Cu.to.1layhid3	-0.178571645

Weight	Value
Ru.to.1layhid3	-0.538053281
Pd.to.1layhid3	1.989313632
Ag.to.1layhid3	-0.796319713
Ir.to.1layhid3	6.370746269
Pt.to.1layhid3	5.618108629
Au.to.1layhid3	4.852729335
Cr.to.1layhid3	1.09598084
Zn.to.1layhid3	-5.008570621
Na.to.1layhid3	1.204042042
K.to.1layhid3	-6.2497086
Mg.to.1layhid3	-0.346707391
Ba.to.1layhid3	0.658972847
B.to.1layhid3	-0.224854889
Al.to.1layhid3	11.67902267
Si.to.1layhid3	2.016787507
Pb.to.1layhid3	0.471955133
S.to.1layhid3	20.14616925
Hg.to.1layhid3	-1.363594352
Y.to.1layhid3	1.582665442
Ti.to.1layhid3	0.326868452
Zr.to.1layhid3	7.895387845
La.to.1layhid3	-0.457303367
Ce.to.1layhid3	-506.8073476
Fe.to.1layhid3	1.003964375
Intercept.to.1layhid4	0.237907994
Temperature.to.1layhid4	3.181034573
Pressure.to.1layhid4	-0.122953541
Catalyst.Mass.to.1layhid4	0.016905114
GSHV.to.1layhid4	-0.919925673
Specifc.Area.BET.to.1layhid4	-0.512695946
Calcination.Temperature.to.1layhid4	0.7363303
Calcination.Time.to.1layhid4	1.244906559
CO.to.1layhid4	1.522965155
H2O.to.1layhid4	-0.771598283
CO2.to.1layhid4	-1.976956409
H2.to.1layhid4	-0.86336982
N2.to.1layhid4	-0.196637364
He.to.1layhid4	-0.26678303
CH4.to.1layhid4	-0.554171962
Fe2O3.to.1layhid4	0.879000478
AC.to.1layhid4	-1.688103687
CNT.to.1layhid4	-0.282624051
Mo2C.to.1layhid4	1.636021008
CeO2.to.1layhid4	-0.052041166
La2O3.to.1layhid4	-0.592395177
ZrO2.to.1layhid4	-0.348411112
MgO.to.1layhid4	-0.257441733

Weight	Value
Al2O3.to.1layhid4	-0.980224548
TiO2.to.1layhid4	-0.004526073
Co.to.1layhid4	-0.440596598
Ni.to.1layhid4	1.00088836
Cu.to.1layhid4	0.441686987
Ru.to.1layhid4	0.485204855
Pd.to.1layhid4	-0.762477359
Ag.to.1layhid4	-1.449884637
Ir.to.1layhid4	50.95322248
Pt.to.1layhid4	-1.907027767
Au.to.1layhid4	2.660054253
Cr.to.1layhid4	-0.550176845
Zn.to.1layhid4	0.522964217
Na.to.1layhid4	-0.779177702
K.to.1layhid4	1.156353504
Mg.to.1layhid4	-0.280584311
Ba.to.1layhid4	-1.472487689
B.to.1layhid4	-2.49725E-05
Al.to.1layhid4	0.602384974
Si.to.1layhid4	1.249175519
Pb.to.1layhid4	0.199888094
S.to.1layhid4	-0.810677114
Hg.to.1layhid4	-1.405620114
Y.to.1layhid4	-0.743832135
Ti.to.1layhid4	1.246871803
Zr.to.1layhid4	-2.050939588
La.to.1layhid4	-1.176346977
Ce.to.1layhid4	1.100571421
Fe.to.1layhid4	-0.761221495
Intercept.to.1layhid5	-0.867405878
Temperature.to.1layhid5	-6.16216893
Pressure.to.1layhid5	-1.609386768
Catalyst.Mass.to.1layhid5	-6.485218456
GSHV.to.1layhid5	-61.1447618
Specifc.Area.BET.to.1layhid5	41.21402286
Calcination.Temperature.to.1layhid5	-1.249879864
Calcination.Time.to.1layhid5	-1.809124897
CO.to.1layhid5	1.427553631
H2O.to.1layhid5	1.319263409
CO2.to.1layhid5	-0.318839761
H2.to.1layhid5	0.224307997
N2.to.1layhid5	3.115005739
He.to.1layhid5	5.139649192
CH4.to.1layhid5	-2.76857057
Fe2O3.to.1layhid5	-30.75233139
AC.to.1layhid5	-29.31629518
CNT.to.1layhid5	1.933314869

Weight	Value
Mo2C.to.1layhid5	-1.474093862
CeO2.to.1layhid5	0.001249612
La2O3.to.1layhid5	-50.91092363
ZrO2.to.1layhid5	2.667456849
MgO.to.1layhid5	1.334227073
Al2O3.to.1layhid5	3.89339902
TiO2.to.1layhid5	-0.626478182
Co.to.1layhid5	0.754340301
Ni.to.1layhid5	2.741012618
Cu.to.1layhid5	2.996950611
Ru.to.1layhid5	-0.402482618
Pd.to.1layhid5	-2.445713735
Ag.to.1layhid5	10.46431149
Ir.to.1layhid5	17.65351643
Pt.to.1layhid5	-26.3379203
Au.to.1layhid5	-25.78570036
Cr.to.1layhid5	-70.27419435
Zn.to.1layhid5	-6.790010008
Na.to.1layhid5	2.39986298
K.to.1layhid5	-0.188724887
Mg.to.1layhid5	-0.007214427
Ba.to.1layhid5	72.65122637
B.to.1layhid5	-1.018599813
Al.to.1layhid5	-1.742973527
Si.to.1layhid5	1.404072059
Pb.to.1layhid5	29.48741442
S.to.1layhid5	-4.97459435
Hg.to.1layhid5	30.13766195
Y.to.1layhid5	3.549760471
Ti.to.1layhid5	-0.090837375
Zr.to.1layhid5	-1.726411157
La.to.1layhid5	-9.607180636
Ce.to.1layhid5	21.80237175
Fe.to.1layhid5	-16.83634368
Intercept.to.1layhid6	1.465450349
Temperature.to.1layhid6	-0.632437276
Pressure.to.1layhid6	0.711809591
Catalyst.Mass.to.1layhid6	-1.515720109
GSHV.to.1layhid6	-0.653953965
Specifc.Area.BET.to.1layhid6	0.859793851
Calcination.Temperature.to.1layhid6	0.5013695
Calcination.Time.to.1layhid6	-1.750395432
CO.to.1layhid6	1.029253724
H2O.to.1layhid6	-0.341499691
CO2.to.1layhid6	3.203078579
H2.to.1layhid6	-0.084902663
N2.to.1layhid6	-1.159794467

Weight	Value
He.to.1layhid6	-3.631901858
CH4.to.1layhid6	0.730992994
Fe2O3.to.1layhid6	-0.543573434
AC.to.1layhid6	0.808969362
CNT.to.1layhid6	1.096335446
Mo2C.to.1layhid6	1.096993384
CeO2.to.1layhid6	-0.525188566
La2O3.to.1layhid6	-1.658710664
ZrO2.to.1layhid6	2.575178614
MgO.to.1layhid6	0.582897177
Al2O3.to.1layhid6	-2.499976917
TiO2.to.1layhid6	0.815777772
Co.to.1layhid6	-22.73431916
Ni.to.1layhid6	10.93278656
Cu.to.1layhid6	-54.39445866
Ru.to.1layhid6	-0.359237267
Pd.to.1layhid6	-0.105559073
Ag.to.1layhid6	0.561355612
Ir.to.1layhid6	0.123532048
Pt.to.1layhid6	-1.473470068
Au.to.1layhid6	2.389542975
Cr.to.1layhid6	0.70707602
Zn.to.1layhid6	-7.146817051
Na.to.1layhid6	5.300959908
K.to.1layhid6	0.331998798
Mg.to.1layhid6	0.81518737
Ba.to.1layhid6	0.236002994
B.to.1layhid6	-2.020485706
Al.to.1layhid6	-6.356574892
Si.to.1layhid6	1.308896504
Pb.to.1layhid6	1.136079079
S.to.1layhid6	14.96421522
Hg.to.1layhid6	0.48748515
Y.to.1layhid6	2.786629666
Ti.to.1layhid6	0.326359423
Zr.to.1layhid6	-462.6482245
La.to.1layhid6	-0.400466049
Ce.to.1layhid6	1.489327208
Fe.to.1layhid6	42.52148394
Intercept.to.1layhid7	1.112623264
Temperature.to.1layhid7	-0.819053773
Pressure.to.1layhid7	2.64753221
Catalyst.Mass.to.1layhid7	0.677831543
GSHV.to.1layhid7	0.088114702
Specifc.Area.BET.to.1layhid7	0.092907843
Calcination.Temperature.to.1layhid7	0.961108519
Calcination.Time.to.1layhid7	-1.436796116

Weight	Value
CO.to.1layhid7	-0.579385047
H2O.to.1layhid7	2.313222337
CO2.to.1layhid7	-1.064021605
H2.to.1layhid7	0.338580931
N2.to.1layhid7	1.801494331
He.to.1layhid7	0.557403264
CH4.to.1layhid7	-0.62548572
Fe2O3.to.1layhid7	-0.564966288
AC.to.1layhid7	-1.056400705
CNT.to.1layhid7	1.998002487
Mo2C.to.1layhid7	-1.859795015
CeO2.to.1layhid7	0.357140109
La2O3.to.1layhid7	-2.925769147
ZrO2.to.1layhid7	2.297537946
MgO.to.1layhid7	0.195839561
Al2O3.to.1layhid7	0.103364389
TiO2.to.1layhid7	0.127726805
Co.to.1layhid7	-0.237669354
Ni.to.1layhid7	-3.231531532
Cu.to.1layhid7	-2.029980976
Ru.to.1layhid7	-0.640150981
Pd.to.1layhid7	-3.864016235
Ag.to.1layhid7	-1.653424157
Ir.to.1layhid7	-0.085045527
Pt.to.1layhid7	7.686523492
Au.to.1layhid7	-1.136184019
Cr.to.1layhid7	-2.114631056
Zn.to.1layhid7	3.105922247
Na.to.1layhid7	-4.794350633
K.to.1layhid7	0.216440157
Mg.to.1layhid7	0.169495716
Ba.to.1layhid7	-2.13870318
B.to.1layhid7	0.37088699
Al.to.1layhid7	4.024690828
Si.to.1layhid7	0.436420581
Pb.to.1layhid7	-0.986037477
S.to.1layhid7	-0.681072359
Hg.to.1layhid7	-2.566101329
Y.to.1layhid7	-1.679833079
Ti.to.1layhid7	0.59307239
Zr.to.1layhid7	38.28368674
La.to.1layhid7	225.6745926
Ce.to.1layhid7	-0.260674223
Fe.to.1layhid7	-9.598490941
Intercept.to.1layhid8	0.698498319
Temperature.to.1layhid8	-2.445559882
Pressure.to.1layhid8	0.712267264

Weight	Value
Catalyst.Mass.to.1layhid8	1.497588803
GSHV.to.1layhid8	0.922650548
Specifc.Area.BET.to.1layhid8	2.189073937
Calcination.Temperature.to.1layhid8	1.113925226
Calcination.Time.to.1layhid8	0.514851167
CO.to.1layhid8	0.225580088
H2O.to.1layhid8	-2.100260007
CO2.to.1layhid8	1.147961168
H2.to.1layhid8	-1.918178242
N2.to.1layhid8	1.441351146
He.to.1layhid8	1.49234053
CH4.to.1layhid8	-0.141937174
Fe2O3.to.1layhid8	-0.242243332
AC.to.1layhid8	-3.760018812
CNT.to.1layhid8	-4.041958297
Mo2C.to.1layhid8	-0.004521227
CeO2.to.1layhid8	1.318823857
La2O3.to.1layhid8	33.04251209
ZrO2.to.1layhid8	-0.885551611
MgO.to.1layhid8	0.890274292
Al2O3.to.1layhid8	0.108783866
TiO2.to.1layhid8	0.056047254
Co.to.1layhid8	0.31861726
Ni.to.1layhid8	-0.297477283
Cu.to.1layhid8	6.316358857
Ru.to.1layhid8	-0.874695139
Pd.to.1layhid8	-1.399504384
Ag.to.1layhid8	-0.714052519
Ir.to.1layhid8	-1.609071425
Pt.to.1layhid8	19.48279812
Au.to.1layhid8	13.20606442
Cr.to.1layhid8	4.85107784
Zn.to.1layhid8	-4.28451441
Na.to.1layhid8	34.4800515
K.to.1layhid8	-0.511451656
Mg.to.1layhid8	-0.981113795
Ba.to.1layhid8	22.83891568
B.to.1layhid8	0.171240247
Al.to.1layhid8	-0.832659372
Si.to.1layhid8	-1.740684369
Pb.to.1layhid8	-1.225690531
S.to.1layhid8	0.841132456
Hg.to.1layhid8	16.66392147
Y.to.1layhid8	-0.239244837
Ti.to.1layhid8	-0.655878226
Zr.to.1layhid8	-0.48512396
La.to.1layhid8	7.43418596

Weight	Value
Ce.to.1layhid8	4.272427729
Fe.to.1layhid8	-2.772697841
Intercept.to.1layhid9	0.574203584
Temperature.to.1layhid9	-2.719292061
Pressure.to.1layhid9	0.500711042
Catalyst.Mass.to.1layhid9	-2.236710296
GSHV.to.1layhid9	-0.422039554
Specifc.Area.BET.to.1layhid9	-1.233628969
Calcination.Temperature.to.1layhid9	-1.033560339
Calcination.Time.to.1layhid9	-0.239918423
CO.to.1layhid9	-0.67279865
H2O.to.1layhid9	-1.772544393
CO2.to.1layhid9	-0.190363295
H2.to.1layhid9	1.5006585
N2.to.1layhid9	2.313402617
He.to.1layhid9	-0.503013026
CH4.to.1layhid9	-1.457185591
Fe2O3.to.1layhid9	0.417544711
AC.to.1layhid9	0.195021899
CNT.to.1layhid9	0.017343497
Mo2C.to.1layhid9	-1.000112076
CeO2.to.1layhid9	0.393330997
La2O3.to.1layhid9	1.773146613
ZrO2.to.1layhid9	1.313774868
MgO.to.1layhid9	-32.91604102
Al2O3.to.1layhid9	3.296767616
TiO2.to.1layhid9	-0.046963444
Co.to.1layhid9	7.291724239
Ni.to.1layhid9	-27.83518863
Cu.to.1layhid9	-16.01833116
Ru.to.1layhid9	1.306304905
Pd.to.1layhid9	-1.531063293
Ag.to.1layhid9	-0.352226269
Ir.to.1layhid9	-2.852300873
Pt.to.1layhid9	-1.813295513
Au.to.1layhid9	-4.995696096
Cr.to.1layhid9	1.894201129
Zn.to.1layhid9	2.695234314
Na.to.1layhid9	2.283027473
K.to.1layhid9	-0.869931121
Mg.to.1layhid9	1.552396571
Ba.to.1layhid9	-0.013536838
B.to.1layhid9	-0.634543673
Al.to.1layhid9	14.28350367
Si.to.1layhid9	-0.586356027
Pb.to.1layhid9	0.086089831
S.to.1layhid9	0.826636886

Weight	Value
Hg.to.1layhid9	-0.555762157
Y.to.1layhid9	-41.5694644
Ti.to.1layhid9	-0.104531639
Zr.to.1layhid9	1.445918427
La.to.1layhid9	-5.605571867
Ce.to.1layhid9	2.611037548
Fe.to.1layhid9	-276.7235797
Intercept.to.1layhid10	1.15081244
Temperature.to.1layhid10	-0.867851245
Pressure.to.1layhid10	-0.025363812
Catalyst.Mass.to.1layhid10	-6.187013347
GSHV.to.1layhid10	1.242948436
Specifc.Area.BET.to.1layhid10	-0.138015856
Calcination.Temperature.to.1layhid10	-0.450360314
Calcination.Time.to.1layhid10	0.05550795
CO.to.1layhid10	0.564131093
H2O.to.1layhid10	-1.689859696
CO2.to.1layhid10	0.144226507
H2.to.1layhid10	0.456933043
N2.to.1layhid10	2.111886335
He.to.1layhid10	0.964267118
CH4.to.1layhid10	3.681220957
Fe2O3.to.1layhid10	0.24956724
AC.to.1layhid10	0.881393443
CNT.to.1layhid10	1.494519279
Mo2C.to.1layhid10	-0.246338448
CeO2.to.1layhid10	1.034851585
La2O3.to.1layhid10	0.536908541
ZrO2.to.1layhid10	-1.807793518
MgO.to.1layhid10	-0.209634052
Al2O3.to.1layhid10	-0.221844371
TiO2.to.1layhid10	-0.63426149
Co.to.1layhid10	0.040693445
Ni.to.1layhid10	-0.318669026
Cu.to.1layhid10	1.645984487
Ru.to.1layhid10	-5.5028328
Pd.to.1layhid10	0.245822998
Ag.to.1layhid10	-1.583271909
Ir.to.1layhid10	-0.867768375
Pt.to.1layhid10	-1.49614031
Au.to.1layhid10	6.435004694
Cr.to.1layhid10	0.868013372
Zn.to.1layhid10	2.326467196
Na.to.1layhid10	-1.084772882
K.to.1layhid10	0.757907899
Mg.to.1layhid10	-1.318019344
Ba.to.1layhid10	-1.53195407

Weight	Value
B.to.1layhid10	-1.138237098
Al.to.1layhid10	0.635003038
Si.to.1layhid10	-1.11598395
Pb.to.1layhid10	-0.380358254
S.to.1layhid10	0.965323485
Hg.to.1layhid10	-0.799484283
Y.to.1layhid10	1.405823613
Ti.to.1layhid10	0.013730167
Zr.to.1layhid10	-3.68437779
La.to.1layhid10	-2.338445035
Ce.to.1layhid10	-0.239183012
Fe.to.1layhid10	9.486880698
Intercept.to.1layhid11	1.103074853
Temperature.to.1layhid11	-7.556210775
Pressure.to.1layhid11	2.902788811
Catalyst.Mass.to.1layhid11	6.767055977
GSHV.to.1layhid11	0.355509248
Specifc.Area.BET.to.1layhid11	0.17751877
Calcination.Temperature.to.1layhid11	1.373211657
Calcination.Time.to.1layhid11	-0.287662201
CO.to.1layhid11	1.235041037
H2O.to.1layhid11	1.49004375
CO2.to.1layhid11	3.090760028
H2.to.1layhid11	-0.767265854
N2.to.1layhid11	-0.209988307
He.to.1layhid11	-1.155916175
CH4.to.1layhid11	-1.494118328
Fe2O3.to.1layhid11	0.372130806
AC.to.1layhid11	-0.400847133
CNT.to.1layhid11	1.627543663
Mo2C.to.1layhid11	0.09105528
CeO2.to.1layhid11	-0.377731272
La2O3.to.1layhid11	0.553432755
ZrO2.to.1layhid11	-2.002351535
MgO.to.1layhid11	-0.449300466
Al2O3.to.1layhid11	2.425541608
TiO2.to.1layhid11	-1.448115324
Co.to.1layhid11	1.841633956
Ni.to.1layhid11	0.651747434
Cu.to.1layhid11	-1.065034285
Ru.to.1layhid11	-1.754939036
Pd.to.1layhid11	-0.154509872
Ag.to.1layhid11	-4.945743234
Ir.to.1layhid11	0.406792632
Pt.to.1layhid11	-0.763236035
Au.to.1layhid11	6.428378238
Cr.to.1layhid11	-1.239724872

Weight	Value
Zn.to.1layhid11	0.263194546
Na.to.1layhid11	-2.343828424
K.to.1layhid11	-1.035660212
Mg.to.1layhid11	0.336186293
Ba.to.1layhid11	-73.05776863
B.to.1layhid11	0.065721917
Al.to.1layhid11	-0.047284986
Si.to.1layhid11	-0.265283968
Pb.to.1layhid11	-0.393667262
S.to.1layhid11	-3.394229761
Hg.to.1layhid11	-4.375253235
Y.to.1layhid11	-0.084908529
Ti.to.1layhid11	0.638063595
Zr.to.1layhid11	0.514158067
La.to.1layhid11	-1.239854943
Ce.to.1layhid11	6.433014257
Fe.to.1layhid11	1.293933194
Intercept.to.1layhid12	-0.075896746
Temperature.to.1layhid12	-0.140227106
Pressure.to.1layhid12	-0.658351356
Catalyst.Mass.to.1layhid12	0.539023516
GSHV.to.1layhid12	-0.99490309
Specifc.Area.BET.to.1layhid12	-0.352351472
Calcination.Temperature.to.1layhid12	1.414664049
Calcination.Time.to.1layhid12	1.148013349
CO.to.1layhid12	-0.428100793
H2O.to.1layhid12	1.91340747
CO2.to.1layhid12	-0.767167022
H2.to.1layhid12	-1.429802488
N2.to.1layhid12	0.493382476
He.to.1layhid12	-0.614553451
CH4.to.1layhid12	10.22475166
Fe2O3.to.1layhid12	-0.208221947
AC.to.1layhid12	2.403332424
CNT.to.1layhid12	-2.463990346
Mo2C.to.1layhid12	0.635552283
CeO2.to.1layhid12	7.550417549
La2O3.to.1layhid12	-0.061662534
ZrO2.to.1layhid12	-1.355685822
MgO.to.1layhid12	-0.380501721
Al2O3.to.1layhid12	-0.257231873
TiO2.to.1layhid12	1.036593812
Co.to.1layhid12	6.398547347
Ni.to.1layhid12	-2.719941661
Cu.to.1layhid12	48.98322418
Ru.to.1layhid12	0.953889168
Pd.to.1layhid12	-3.219533462

Weight	Value
Ag.to.1layhid12	-0.095432774
Ir.to.1layhid12	0.957691468
Pt.to.1layhid12	1.007033206
Au.to.1layhid12	-11.41871576
Cr.to.1layhid12	-1.544594477
Zn.to.1layhid12	0.063568328
Na.to.1layhid12	-271.3182626
K.to.1layhid12	0.558022494
Mg.to.1layhid12	-1.058609542
Ba.to.1layhid12	-1.510505097
B.to.1layhid12	-0.141710503
Al.to.1layhid12	-0.609778569
Si.to.1layhid12	1.613599519
Pb.to.1layhid12	-1.746493033
S.to.1layhid12	-1.446950914
Hg.to.1layhid12	-0.642469732
Y.to.1layhid12	0.018842698
Ti.to.1layhid12	-0.259640598
Zr.to.1layhid12	-26.91141911
La.to.1layhid12	62.02912896
Ce.to.1layhid12	-0.769141145
Fe.to.1layhid12	23.23357536
Intercept.to.Conversion	-1.94877885
1layhid.1.to.Conversion	-0.373794276
1layhid.2.to.Conversion	0.414363729
1layhid.3.to.Conversion	0.6800703
1layhid.4.to.Conversion	1.980621469
1layhid.5.to.Conversion	0.682968782
1layhid.6.to.Conversion	0.59532575
1layhid.7.to.Conversion	-0.322688963
1layhid.8.to.Conversion	1.61706785
1layhid.9.to.Conversion	-0.829333158
1layhid.10.to.Conversion	-0.939182325
1layhid.11.to.Conversion	-0.537103471
1layhid.12.to.Conversion	0.789510664

Source: (CAVALCANTI *et al.*, 2019)

APPENDIX C – PYTHON CODE TO ESTIMATE KINETIC PARAMETERS

```
#####
#
#   Program: KINETIC PARAMETER ESTIMATION FOR WGSR   #
#           USING scipy.optimize.curve_fit           #
#   Author: FÁBIO MACHADO CAVALCANTI               #
#   Location: GHENT UNIVERSITY, BELGIUM             #
#   CreationDate: 2020-04-06                        #
#   Updated on 2021-01-12                          #
#   Special code improvement from Leonardo Cavalcanti #
#           (Oregon State University)               #
#
#####

import numpy as np
import matplotlib.pyplot as plt
from scipy.integrate import odeint
from scipy.optimize import curve_fit
import pandas as pd
from scipy import stats
from pyswarm import pso
import pdb # pdb.set_trace()
from time import process_time
import time
from numpy.random import seed
import os
import errno

# creating new directory for the output files
actual_path = os.getcwd()
# print(actual_path)
script_name = os.path.basename(__file__) #get only the name of the
script file
modelnumber = os.path.splitext(script_name)[0] #without extension
timestr = time.strftime("%Y-%m-%d-%Hh%M_")

# filename_std = actual_path + '/results_' + timestr + modelnumber +
# '/' + modelnumber
filename_std = actual_path + '/results_' + modelnumber + '/' +
modelnumber
filename = filename_std + '_output_regression.txt'

if not os.path.exists(os.path.dirname(filename)):
    try:
        os.makedirs(os.path.dirname(filename))
    except OSError as exc: # Guard against race condition
        if exc.errno != errno.EEXIST:
```

```

        raise

with open(filename, 'w') as f:

    start = process_time()

    #####
    #                                     #
    #             USER INPUT             #
    #                                     #
    #####

    # parameter initial guess
    k0 = 1.e4
    E = 1.e5
    par0 = np.array([k0,E])
    NP = par0.shape[0]

    NY = 1

    # Select initial guess
    # initial_guess = "user_defined"
    initial_guess = "PSO"

    # Select mode
    mode = "regression"
    # mode = "simulation"

    #####
    #                                     #
    #             READ INPUT DATA        #
    #                                     #
    #####

    # Import data file using the Brazilian decimal system
    #Read the pandas dataframe
    mydata =
pd.read_csv('kinetic_data.csv',delimiter=";",decimal=",")
    mydata['T'] = mydata['T'] + 273.15

    #data_exp={}

    #Select columns and convert the pandas dataframe into a NumPy
array
    label_exp = mydata['Exp'].to_numpy()
    T_exp = mydata['T'].to_numpy()
    FA0_exp = mydata['FA0'].to_numpy()

```



```

#data_exp['FA0_exp'] = mydata['FA0'].to_numpy()
FB0_exp = mydata['FB0'].to_numpy()
FC0_exp = mydata['FC0'].to_numpy()
FD0_exp = mydata['FD0'].to_numpy()
FI0_exp = mydata['FI0'].to_numpy()
FA_exp = mydata['FA'].to_numpy()
w_exp = mydata['w'].to_numpy()
replicate_exp = mydata['Replicate'].to_numpy()

NE = len(mydata['T']) # number of experimental points

#####
#                                                                 #
#                               DEFINE MODEL                       #
#                                                                 #
#####

# define kinetic model
def kinetics(F,W,par,parC):

    T,FA0,FB0,FC0,FD0,FI0 = parC    # constant parameters
    k0,E = par                       # optimized parameters

    Tref = 350.+273.15
    R = 8.314 #J/mol.K
    k = k0*np.exp(-E/R*(1/T-1/Tref))
    Keq = np.exp(4577.8/T-4.33)

    PT = 1.
    FA = F[0]
    # FC = F[1]
    # FB = (FB0+FC0)-FC
    FD = (FD0+FA0)-FA
    FB = (FA0+FB0+2*FD0)-FA-2*FD
    FC = (FB0+FC0)-FB

    if FA == 0.:
        FA = 1.e-20
    if FB == 0.:
        FB = 1.e-20
    if FC == 0.:
        FC = 1.e-20
    if FD == 0.:
        FD = 1.e-20

    FT = FA+FB+FC+FD+FI0

```

```

PA = FA/FT*PT
PB = FB/FT*PT
PC = FC/FT*PT
PD = FD/FT*PT

if FA == 0. or FB == 0.:
    beta = 1.e20
else:
    beta = (PC*PD)/(PA*PB)*1/Keq

NUM = k*PA*PB*(1.-beta)
DEN = 1.
rate = NUM/DEN

dFAdW = -rate

return np.array([dFAdW])

# simulate for curve_fit
def simulate(label_exp,k0,E):
    par = np.array([k0,E])
    W = np.linspace(0,0.1,50)
    FA_calc = np.zeros((NE))
    for i in range(NE):
        F0 = np.array([FA0_exp[i]]) # umol/min
        parC =
np.array([T_exp[i],FA0_exp[i],FB0_exp[i],FC0_exp[i],FD0_exp[i],FI0_e
xp[i]])
        args = (par,parC)
        F = odeint(kinetics,F0,W,args)
        FA_calc[i] = F[-1,0]
    F_calc = np.r_[FA_calc]
    return F_calc

# simulate for general purposes
def simulate2(par,F0,parC):
    W = np.linspace(0,0.1,50)
    args = (par,parC)
    F = odeint(kinetics,F0,W,args)
    return F[-1,:]

# define objective
def objective(par):
    obj = 0.
    for i in range(NE):
        F0 = np.array([FA0_exp[i]]) # umol/min

```

```

        parC =
np.array([T_exp[i],FA0_exp[i],FB0_exp[i],FC0_exp[i],FD0_exp[i],FI0_e
xp[i]])
        F = simulate2(par,F0,parC)
        obj = obj + ((F[0]-FA_exp[i])/w_exp[i])**2
    return obj

# PSO for getting a better initial estimative
if initial_guess == "PSO":
    seed(222)
    lb = np.array([0.,0.])
    ub = np.array([1.e7,1.e6])
    swarmsize= 100
    maxiter= 100
    par0, f0 =
pso(objective,lb,ub,swarmsize=swarmsize,maxiter=maxiter,debug=True)
    # par0, f0 =
pso(objective,lb,ub,swarmsize=100,maxiter=100,debug=True)
    for i in range(NP):
        # print('par'+str(i+1)+': ' + str(par_opt[i]), '+/- ' +
str(par_error[i]))
        print("par{:<2d}: {:.10.3E}".format(i+1,par0[i]))
        print("f0    : {:.2f}".format(f0))
        print("swarmsize: {:<6d}".format(swarmsize))
        print("maxiter: {:<6d}".format(maxiter))
        pdb.set_trace()

#####
#
#          ESTIMATE MODEL PARAMETERS          #
#          curve_fit                          #
#
#####

if mode == "regression":

    F_exp = np.r_[FA_exp]
    weights = np.r_[np.sqrt(w_exp)]
    bounds = ((0.,0.),(np.inf,np.inf))
    par_opt,pcov =
curve_fit(simulate,label_exp,F_exp,p0=par0,sigma=weights,bounds=boun
ds)

    # print("pcov")
    # print(pcov,"\n")

```

```

# calculate model with updated parameters
F_calc = np.zeros((NE,NY))
for i in range(NE):
    F0 = np.array([FA0_exp[i]]) # umol/min
    parC =
np.array([T_exp[i],FA0_exp[i],FB0_exp[i],FC0_exp[i],FD0_exp[i],FI0_e
xp[i]])
    F_calc[i,:] = simulate2(par_opt,F0,parC)
#print(F_calc)

#print initial information
print('\nmode: ' + mode, file=f)
print('initial_guess: ' + initial_guess, file=f)
if initial_guess == "PSO":
    print("swarmsize: {:<6d}".format(swarmsize),file=f)
    print("maxiter: {:<6d}\n".format(maxiter),file=f)
for i in range(NP):
    print("par0{:<2d}: {:<10.3E}".format(i+1,par0[i]), file=f)

# parameter confidence interval
par_std = np.sqrt(np.diag(pcov)) # array with parameter stdev
values
matrix
aux = np.linalg.inv(np.diag(par_std,0)) # inverse of diagonal
matrix
pcor = aux.dot(pcov).dot(aux)
print("\npcor", file=f)
print(pcor,"\n", file=f)

par_error = np.zeros((NP))
df = NY*NE-NP
alpha = 0.05 # significance level
t = stats.t.ppf(1.-alpha/2.,df)
for i in range(NP):
    par_error[i] = t*par_std[i]

# optimized parameter values
for i in range(NP):
    # print('par'+str(i+1)+': ' + str(par_opt[i]), '+/- ' +
str(par_error[i]))
    print("par{:<2d}: {:<10.3E} +/-
{:<10.3E}".format(i+1,par_opt[i],par_error[i]), file=f)

# R2 - Coefficient of Determination
#print(np.c_[FA_exp,FC_exp])
#print(np.array([np.mean(FA_exp),np.mean(FC_exp)]))
SSres = np.sum((F_calc - np.c_[FA_exp])**2)
SStotal = np.sum((np.c_[FA_exp]-
np.array([np.mean(FA_exp)]))**2)
R2 = 1 - SSres/SStotal

```

```

Fobj = np.sum(((F_calc - np.c_[FA_exp])/np.c_[w_exp])**2)
print("\nR^2: {:.4f}".format(R2), file=f)
print("\nSSQ: {:.4f}".format(SSres), file=f)
print("Fobj: {:.4f}".format(Fobj), file=f)

# RMSD - Root Mean Square Deviation
RMSD = np.sqrt(SSres/(NE*NY))
print("RMSD: {:.4f}".format(RMSD), file=f)

# F-test (ANOVA)
SSreg = np.sum((F_calc - np.array([np.mean(FA_exp)]))**2)
df_reg = NP - 1
df_res = NE*NY - NP
MSSreg = SSreg/df_reg
MSSres = SSres/df_res
Fvalue = MSSreg/MSSres
Ftab = stats.f.ppf(1.-alpha,df_reg,df_res)
print('\ndf_reg : ' + str(df_reg), file=f)
print('df_res : ' + str(df_res), file=f)
print("F_value: {:.2f}".format(Fvalue), file=f)
print("F_tab : {:.2f}".format(Ftab), file=f)

# write outputs in a csv file
data2write = {'FAexp': FA_exp,
              'FAcalc': F_calc[:,0],}
dataframe =
pd.DataFrame(data2write,columns=['FAexp', 'FAcalc'])
# print(dataframe)
#mydata =
pd.read_csv('dados_francielle.csv',delimiter=";",decimal=",")
filename2 = filename_std + '_output_predictions.csv'
dataframe.to_csv(filename2,sep=";",decimal=",",index=False)

elif mode == "simulation":

    par_opt = par0

    # calculate model with updated parameters
    F_calc = np.zeros((NE,NY))
    for i in range(NE):
        F0 = np.array([FA0_exp[i]]) # umol/min
        parC =
np.array([T_exp[i],FA0_exp[i],FB0_exp[i],FC0_exp[i],FD0_exp[i],FI0_e
xp[i]])
        F_calc[i,:] = simulate2(par_opt,F0,parC)
    #print(F_calc)

    #print initial information

```

```

print('\nmode:' + mode, file=f)
print('initial_guess: ' + initial_guess, file=f)
if initial_guess == "PSO":
    print("swarmsize: {:<6d}".format(swarmsize),file=f)
    print("maxiter: {:<6d}\n".format(maxiter),file=f)
for i in range(NP):
    print("par0{:<2d}: {:<10.3E}".format(i+1,par0[i]), file=f)

# R2 - Coefficient of Determination
#print(np.c_[FA_exp,FC_exp])
#print(np.array([np.mean(FA_exp),np.mean(FC_exp)]))
SSres = np.sum((F_calc - np.c_[FA_exp])**2)
SStotal = np.sum((np.c_[FA_exp]-
np.array([np.mean(FA_exp)]])**2)
R2 = 1 - SSres/SStotal
print("\nR^2: {:.4f}".format(R2), file=f)
print("\nSSQ: {:.4f}".format(SSres), file=f)

# RMSD - Root Mean Square Deviation
RMSD = np.sqrt(SSres/(NE*NY))
print("RMSD: {:.4f}".format(RMSD), file=f)

# write outputs in a csv file
data2write = {'FAexp': FA_exp,
              'FAcalc': F_calc[:,0],}
dataframe =
pd.DataFrame(data2write,columns=['FAexp','FAcalc'])
# print(dataframe)
#mydata =
pd.read_csv('dados_francielle.csv',delimiter=";",decimal=",")
filename2 = filename_std + '_output_predictions.csv'
dataframe.to_csv(filename2,sep=";",decimal=",",index=False)

#####
#
#
#
#
#####

fig = plt.figure(1,figsize=(12,10))
plt.rcParams["axes.spines.right"] = False
plt.rcParams["axes.spines.top"] = False
plt.rcParams["axes.labelweight"] = "bold"
plt.rcParams.update({'font.size': 14})

plt.subplot(2,2,1)
plt.plot(FA_exp,F_calc[:,0],'bo')
plt.plot([0, 4.5e2], [0, 4.5e2],'k--')

```

```

plt.xlim([0, 4.5e2])
plt.ylim([0, 4.5e2])
plt.xticks([0,100,200,300,400])
plt.yticks([0,100,200,300,400])
plt.xlabel('experimental F$_{CO}$ ($\mu$mol/min)')
plt.ylabel('simulated F$_{CO}$ ($\mu$mol/min)')

#####
#                                                                 #
#              OTHER PLOTS                                       #
#          SENSITIVITY ANALYSIS                                   #
#              TEMPERATURE                                       #
#                                                                 #
#####

# varying Temperature
T_sa = np.arange(200.,500.+5.,5.)
T_sa += 273.15
NT_sa = T_sa.shape[0]
F_T_sa = np.zeros((NT_sa,NY))
XCO_T_sa = np.zeros((NT_sa,1))

VA0 = 4.93      # mL/min
VB0 = 12.325
VC0 = 0.
VD0 = 0.
VI0 = 25.99

# convert volumetric flow rate into molar flow rate
def par_T_sa(T,V):
    F = (1.*V)/(82.05*T)*1e6
    return F

# simulate varying the temperature
for i in range(NT_sa):
    F0 = np.array([par_T_sa(T_sa[i],VA0)])      # umol/min

    parC =
np.array([T_sa[i],par_T_sa(T_sa[i],VA0),par_T_sa(T_sa[i],VB0),
par_T_sa(T_sa[i],VC0),par_T_sa(T_sa[i],VD0),par_T_sa(T_sa[i],VI0)])
    F_T_sa[i,:] = simulate2(par_opt,F0,parC)
    XCO_T_sa[i,0] = (par_T_sa(T_sa[i],VA0)-
F_T_sa[i,0])/par_T_sa(T_sa[i],VA0)*100.

# print(T_sa)
# print(F_T_sa)
# print(XCO_T_sa)

```

```

# read experimental data varying the temperature
mydata =
pd.read_csv('results_T_sa_XCO.csv',delimiter=";",decimal=",")
T_sa_exp = mydata['T_sa_exp'].to_numpy()
XCO_T_sa_exp = mydata['XCO_T_sa_exp'].to_numpy()
error_T_sa_exp = mydata['error_T_sa_exp'].to_numpy()

plt.subplot(2,2,3)
plt.plot(T_sa-273.15, XCO_T_sa,'b-', linewidth=2)
plt.plot(T_sa_exp, XCO_T_sa_exp,'ko')
plt.errorbar(T_sa_exp, XCO_T_sa_exp, yerr=error_T_sa_exp, fmt='
', ecolor='k', elinewidth=1, capsize=4)
plt.xlabel('Temperature ($^oC$)')
plt.ylabel('CO Conversion (%)')
plt.xlim([175, 525])
plt.ylim([-5, 100])
# plt.legend(['mod', 'exp'])
#plt.show()

#####
#
#
#           OTHER PLOTS
#           SENSITIVITY ANALYSIS
#           SPACE TIME W/F
#
#####

# varying Space Time W/F
FT_sa = np.arange(600.,3600.+40.,40.) # umol/min
N_WF_sa = FT_sa.shape[0]
F_WF_sa = np.zeros((N_WF_sa,NY))
XCO_WF_sa = np.zeros((N_WF_sa,1))

FA0_sa = 0.1*FT_sa
FB0_sa = 0.25*FT_sa
FC0_sa = 0.*FT_sa
FD0_sa = 0.*FT_sa
FI0_sa = 0.65*FT_sa

T_list = [300.,350.,400.]
XCO_list = []
T_list_str = []

for T_WF in T_list:
    T_list_str.append('T = ' + str(int(T_WF)) + '^oC')

```



```

    T_WF += 273.15
    # F_WF_sa = np.zeros((N_WF_sa,NY))
    for i in range(N_WF_sa):
        F0 = np.array([FA0_sa[i]])
        parC =
np.array([T_WF,FA0_sa[i],FB0_sa[i],FC0_sa[i],FD0_sa[i],FI0_sa[i]])
        F_WF_sa[i,:] = simulate2(par_opt,F0,parC)
        XCO_WF_sa[i,0] = (FA0_sa[i]-F_WF_sa[i,0])/FA0_sa[i]*100.
    XCO_aux = XCO_WF_sa.copy() # to avoid updating variables by
the pointer
    XCO_list.append(XCO_aux)

W_FA0 = 0.1/FA0_sa*60000 # kg.s/mol

# read experimental data varying the space time
mydata =
pd.read_csv('results_WF_sa_XCO.csv',delimiter=";",decimal=",")
#Select columns and convert the pandas dataframe into a NumPy
array
WF_300_exp = mydata['WF_300_exp'].to_numpy()
XCO_300_exp = mydata['XCO_300_exp'].to_numpy()
error_300 = mydata['error_300'].to_numpy()
WF_350_exp = mydata['WF_350_exp'].to_numpy()
XCO_350_exp = mydata['XCO_350_exp'].to_numpy()
error_350 = mydata['error_350'].to_numpy()
WF_400_exp = mydata['WF_400_exp'].to_numpy()
XCO_400_exp = mydata['XCO_400_exp'].to_numpy()
error_400 = mydata['error_400'].to_numpy()

plt.subplot(2,2,4)
colors_list = ['b','r','g']
for i,XCO_WF_sa in enumerate(XCO_list):
    plt.plot(W_FA0,XCO_WF_sa,linewidth=2,color=colors_list[i])
plt.plot(WF_300_exp, XCO_300_exp, 'bo')
plt.plot(WF_350_exp, XCO_350_exp, 'ro')
plt.plot(WF_400_exp, XCO_400_exp, 'go')
plt.errorbar(WF_300_exp, XCO_300_exp, yerr=error_300, fmt=' ',
ecolor='b', elinewidth=1, capsize=4)
plt.errorbar(WF_350_exp, XCO_350_exp, yerr=error_350, fmt=' ',
ecolor='r', elinewidth=1, capsize=4)
plt.errorbar(WF_400_exp, XCO_400_exp, yerr=error_400, fmt=' ',
ecolor='g', elinewidth=1, capsize=4)
plt.xlabel('W/$F_{CO}$ (kg.s/mol)')
plt.ylabel('CO Conversion (%)')
plt.ylim([0, 100])
# plt.legend(T_list_str,loc='upper left')
# plt.show()

```

```
my_dpi = 144
filename = filename_std + '_CEJ.png'
plt.savefig(filename)
plt.show()

end = process_time()
print("\nelapsed time: {:.2f} seconds".format(end-start),
file=f)

print('\nEND')
```